EFFICIENT ANALYSIS OF LARGE ARRAY ANTENNAS

A THESIS SUBMITTED TO
THE GRADUATE SCHOOL OF NATURAL AND APPLIED SCIENCES
OF
MIDDLE EAST TECHNICAL UNIVERSITY

BY

FATİH OVALI

IN PARTIAL FULFILLMENT OF THE REQUIREMENTS FOR
THE DEGREE OF MASTER OF SCIENCE

IN

ELECTRICAL AND ELECTRONICS ENGINEERING

DECEMBER 2004

Approval of the Graduate School of Natural and Applied Sciences

Prof. Dr. Canan ÖZGEN
Director

I certify that this thesis satisfies all the requirements as a thesis for the degree of Master of Science.

Prof. Dr. İsmet ERKMEN
Head of Department

This is to certify that we have read this thesis and that in our opinion it is fully adequate, in scope and quality, as a thesis for the degree of Master of Science.

Assoc. Prof. Dr. Özlem Aydın ÇİVİ
Supervisor

Examining Committee Members

Prof. Dr. Mustafa KUZUOĞLU	(METU, EE)	———
Assoc. Prof. Dr. Özlem Aydın ÇİVİ	(METU, EE)	———
Assoc. Prof. Dr. Gülbin DURAL	(METU, EE)	———
Assist. Prof. Dr. Lale ALATAN	(METU, EE)	———
Assist. Prof. Dr. Vakur B. ERTÜRK	(BİLKENT, EE)	———

I hereby declare that all information in this document has been obtained and presented in accordance with academic rules and ethical conduct. I also declare that, as required by these rules and conduct, I have fully cited and referenced all material and results that are not original to this work.

Fatih OVALI

ABSTRACT

EFFICIENT ANALYSIS OF LARGE ARRAY ANTENNAS

Ovalı, Fatih
M.S, Electrical and Electronics Engineering Department
Supervisor: Assoc. Prof. Özlem Aydın Çivi

December 2004, 98 pages

Large phased array antennas are widely used in many military and commercial applications. The analysis of large arrays containing many antenna or frequency-selective (FSS) surface elements is inefficient or intractable when brute force numerical methods are used. For the efficient analysis of such structures hybrid methods (analytic and numerical, numerical and numerical) can be used. In this thesis, a hybrid method combining the uniform geometrical theory of diffraction (UTD) and the moment method (MoM) used for the analysis of large, finite arrays is modified for the efficient yet accurate analysis of large printed dipole arrays. In the present hybrid UTD-MoM approach, the number of unknowns to be solved is drastically reduced as compared to the conventional MoM approach, which provides a great efficiency on the computational cost. This extreme reduction in the number of MoM unknowns is carried out by introducing a few UTD-ray type global basis functions for the unknown array element currents. In this study, this hybrid UTD-MoM method is applied to the analysis of a finite, planar periodic array of printed dipoles on a grounded dielectric substrate. The efficiency and accuracy of this hybrid method are demonstrated with some numerical results.

Keywords: Large finite arrays, UTD-MoM

ÖZ

BÜYÜK ANTEN DİZİLERİNİN EFEKTİF ANALİZİ

Ovalı, Fatih
Y. Lisans, Elektrik-Elektronik Mühendisliği Bölümü
Tez Yöneticisi: Doç. Dr. Özlem Aydın Çivi

Aralık 2004, 98 sayfa

Faz dizili büyük antenler yaygın olarak birçok askeri ve ticari uygulamada kullanılmaktadır. Çok fazla sayıda anten ya da frekans seçici elemana sahip dizilerin analizi sadece nümerik yöntemler kullanılarak çözüldüğünde olanaksız hale gelmektedir. Bu tür yapıların efektif bir şekilde analizi için hibrit yöntemler (analitik ve nümerik, nümerik ve nümerik) kullanılabilir. Bu tezde, büyük sonlu anten dizilerinin analizi için geliştirilmiş olan UTD-MoM metodu, çok sayıda faz dizilimli baskı dipol içeren anten dizilerinin efektif ve doğru analizi için uyarlanmıştır. Bu hibrit UTD-MoM yönteminde çözülmesi gereken bilinmeyen sayısı konvansiyonel MoM yöntemindekine göre oldukça azdır ve bu da işlemsel açıdan büyük kolaylık sağlamaktadır. Bilinmeyen sayısındaki bu önemli azalma, elemanların bilinmeyen akım değerlerinin birkaç UTD-ışın tipi baz fonksiyonları cinsinden ifade edilmesiyle sağlanmaktadır. UTD-MoM hibrit metodu bu çalışmada topraklanmış dielektrik bir materyal üzerine periyodik olarak basılmış çok sayıda dipol içeren bir anten dizisinin analizi için kullanılmıştır. Bu yöntemin doğruluğu ve verimliliği elde edilen sonuçlarla gösterilmiştir.

Anahtar Kelimeler: Büyük Anten Dizileri, UTD-MoM

ACKNOWLEDGMENTS

I would like to express my deepest gratitude to my supervisor, Assoc. Prof. Özlem Aydın ÇİVİ, for her excellent guidance, advice, criticism and encouragement throughout my thesis studies. I would like to express my sincere thanks to her for her invaluable assistance during the preparation of the final manuscript. This work would not have been brought out without her effort and support.

I would like to express my appreciation to my director at work, Dr. Sartuk KARASOY, for his encouragement, support and tolerance. I also would like to thank my colleagues in System Engineering Group at work for their valuable comments and ideas.

I would like to express my sincere gratitude to my family for their constant support and encouragement throughout my life. Last but not least, I want to thank my first, new-born nephew, Onur Kemal AYTÜRK for bringing joy and happiness to our lives.

TABLE OF CONTENTS

LIST OF FIGURES

FIGURES

CHAPTER 1

INTRODUCTION

Printed periodic phased array antennas are currently being used in many commercial and military applications due to their advanced and advantageous characteristics. Contrary to dish or slotted array antennas, which use physical shape and direction to form and steer the beam, phased array antennas utilize the interference between multiple radiating elements to achieve beam forming and beam steering. By electronically adjusting the signal radiated by each element, the combined radiation pattern can be scanned and shaped at high speed and have advanced capabilities. Phased-array antennas have been developed mainly for radar applications but nowadays they are also used for space-based communications and aerospace applications because of their advantages in scanning, beam agility, reliability (performance degrades slowly if some elements malfunction), less structural intrusion (no moving parts, easier to fit into confined space), re-configurability, weight, and power. In future satellite communication systems, demands for faster access and more information are expected to increase because of the continuous growth of the Internet and direct-to-user satellite requirements. Meeting these requirements will require multi-beam satellite systems having an onboard active phased-array antenna system. Phased-array-antenna-based communications links are anticipated to deliver high data rates without the risk of the single-point failure of the gimbaled motors and transmitters used in reflector-based systems. Thus phased array antenna technology is very popular and analysis of large finite arrays gained more importance as a result of this trend in the antenna technology. It is therefore of interest to develop an efficient yet accurate analysis of large finite arrays.

Infinite periodic structure approach was used in the early analysis of large finite arrays. This method gives approximate solutions for large arrays; only the performance of the middle elements can be estimated accurately, current distribution of the elements on or near the edges can not be obtained correctly. As a result of this, main beam of the radiation pattern can be predicted accurately whereas far side lobe patterns can not. Full-wave analysis methods such as Method of Moments (MoM) or Finite Element Method (FEM) should be used in order to achieve rigorous solutions. In the conventional MoM approach [1] for the analysis of antennas, an integral equation is reduced to a matrix equation, and then this matrix equation is solved for the unknown element currents. Although MoM permits handling of problems which cannot be solved by analytic methods, it rapidly becomes impractical for solving electrically large problems due to the enormous number of unknowns. Asymptotic high-frequency methods such as Uniform Theory of Diffraction (UTD) [2], [3], [4] are preferable for the analysis of electrically large problems. Yet they can not be used alone when the geometry of interest contains electrically small antenna/FSS elements. However, lacking features of MoM and UTD can be compensated when they are combined to form a hybrid method that enables efficient analysis of large finite array radiation/scattering problems.

Many works have been published regarding UTD-MoM. In 1975, Burnside et al. [5] provided the solution of current distribution on a simple wedge using the results of scattering of a TE plane wave incident on the wedge. They achieved this by introducing a few local basis functions in the vicinity of diffraction point and two additional diffraction current functions, one on each wall of wedge, away from the diffraction point. Agreement of their results with the exact solutions showed that this kind of 2-D problems could be solved with few unknowns by the help of UTD-MoM. Again in 1975, Thiele and Newhouse [6] used this hybrid technique for the characterization of wire antennas on or near three-dimensional metallic surface. The basic idea in their work was to modify the impedance matrix using UTD to

include diffractions from metallic body or discontinuity where the antenna was placed on or nearby. They modeled the current on the wire by conventional piecewise-sinusoidal basis functions, whereas for the coupling of the wire with the conducting body they used a UTD based Green's function. Thus, only the wire antenna had unknown current to be solved for. Srikanth et al [7] extended the work of Burnside et al [5] by analyzing the scattering from a perfectly conducting semi-circular cylinder, where they took the coupling between the sharp edges and curved surfaces into account for their UTD-MoM hybrid solution. Again they employed only a few rectangular pulse type basis functions in the close vicinity of the edges. For the remaining part, which may be electrically large, they used UTD type basis functions. Eventually the number of unknowns was considerably less than those in conventional MoM solution.

The initial point in solving the problems of periodic structures such as radiation/scattering from planar periodic arrays of infinite extent is Floquet's Theorem. In the MoM analysis of infinite periodic arrays, only one cell called *unit cell* is treated with the use of Floquet Modes [8]. Floquet modes of infinite periodic structures are briefly explained in the Appendix A. The determination of the unknown current coefficients (more than one expansion modes per element) for one element in that unit cell accounts for all other elements as well due to the periodic and infinite structure. This approach cannot directly be applied to finite planar periodic arrays, however Shubert and Munk [9] adapted the infinite array theory to finite arrays such that they expanded the current amplitudes on the dipole elements into Fourier series which allowed them to express their finite array solution in terms of Floquet based infinite array solution. Ishimaru et al [10] reported a different procedure, which they called "finite periodic structure" method. Their solution based on a convolution integral of two functions: one is in the form of Floquet based infinite array solution, and the other involving the Fourier transform of the aperture current distribution. They carried out this method for a dipole array in free space. Skrivervik and Mosig [11] extended the work of [10] by

applying that method to finite periodic array of microstrip antennas. The methods in [9], [10], [11] allow the MoM operator matrix to be computed in terms of Floquet-modes, which is more efficient as compared to the conventional MoM solution. However, all those methods do not provide any advantage in reducing the number of unknowns which is still at least equal to or greater than the number of array elements.

Carin and Felsen [12] and Carin et al [13] carried out an asymptotic high-frequency analysis on scattering from a 2-D truncated array of infinitely long line sources of conducting strips. Their algorithm based on truncated Floquet modes and Floquet based edge diffractions due to truncations of the array.

Asymptotic high-frequency based analysis on completely finite arrays have been reported by Capolino [14] and Çivi et al [15,16] to include the 3-D wave diffractions from the array corners, in addition to the 3-D Floquet mode waves excited from the interior of the array and diffractions from the edges. Çivi et al [17] extended the study of [16] to include the presence of grounded dielectric substrates on which the array elements are placed. Asymptotic ray solutions are based on Kirchhoff approximation, which assumes that the aperture field distribution over the finite array is the same as that for the corresponding infinite array. High-frequency based analysis regarding the array of dipoles on a grounded dielectric slab was also carried out in [18] and [19].

In this study, an efficient analysis of an electrically large, finite, planar periodic array of printed dipoles on a grounded dielectric substrate is developed based on the study of [17]. In this hybrid UTD-MoM method, an integral equation formulation for the unknown currents on the dipoles is constituted as in the conventional MoM approach. Then unknown array element currents are expanded employing a few UTD-ray type global basis functions resulting in a drastic reduction in the number of unknowns as compared to the conventional MoM.

Those expansion functions are tested with the same functions to produce Galerkin solution, whereas in [17] point matching is used. Galerkin procedure provides more accurate results.

The composition of this thesis is as follows. In Chapter 2, formulation for the hybrid UTD-MoM approach is presented for the efficient analysis of electrically large, planar, periodic, finite array of printed dipoles. In Section 2.1, the conventional moment method formulation is provided for the array under consideration. An integral equation for the unknown element currents is obtained and reduced to a well-known matrix equation [Z][I]=[V]. In Section 2.2, the UTD ray concept that describes the asymptotic ray behavior of radiated/scattered fields from a planar array of printed dipoles is explained briefly which constitutes the basis for UTD-MoM formulation. In Section 2.3., UTD-MoM formulation is developed. UTD-type global basis functions for the unknown array element currents are defined and the unknown current [I] in conventional MoM are expanded using those UTD based basis functions. This operation enables a substantial reduction in the number of unknowns such that the matrix equation [Z][I] = [V] in the conventional MoM is transformed to a smaller size matrix equation $[Z'][I'] = [V']$. In Chapter 3, numerical results are presented to validate the efficiency and accuracy of the UTD-MoM approach. Results obtained by UTD-MoM method are compared with the conventional MoM results, results of [17] and the infinite array solution. Concluding remarks and future work are presented in Chapter 4.

CHAPTER 2

FORMULATION

In this chapter, the hybrid method combining the uniform geometrical theory of diffraction with the moment method approach is presented for the efficient analysis of electrically large, planar, periodic, finite array of printed dipoles. The problem geometry and configuration shown in Figure 2.1 are chosen because this structure provides simplicity in the development and understanding of the present hybrid method. However this approach can be utilized for the analysis of more complex arrays such as large finite array of microstrip patch antennas etc.

In Section 2.1, conventional moment method formulation is provided for the problem of geometry shown in Figure 2.1. An integral equation for the unknown element currents is obtained and reduced to the well-known matrix equation [Z][I]=[V].

In Section 2.2, UTD ray concept describing the asymptotic ray behavior of radiated/scattered fields from a planar array of printed dipoles is explained briefly. It is shown that the total field at an observation point sufficiently far from the source point can be represented as a sum of a few rays coming from special points in array.

In the light of Sections 2.1 and 2.2, UTD-MoM formulation is developed in Section 2.3. With the assumption that the current amplitudes on the array elements also obey the UTD rules, UTD-type global basis functions for the unknown array element currents are defined. The integral equation for the unknown current elements on the array obtained via conventional MoM method is solved by utilizing

those UTD-type global basis functions which yields a drastic reduction in the number of unknown current elements to be solved for. An example is given at the end of this section to show how the reduction in the number of unknowns, which is the essence of this hybrid method, is achieved.

2.1 The Moment Method Solution

In this section, a MoM formulation is provided in spectral domain for the rectangular periodic array of printed dipoles shown in Figure 2.1. An electric field integral equation (EFIE) is obtained using grounded dielectric slab Green's function. Piecewise-sinusoidal expansion and weighting functions are used yielding Galerkin solution.

The printed dipole elements are assumed to be perfectly conducting and oriented in the $\hat{a}_x$ direction on a grounded dielectric slab of infinite extent (Figure 2.1). Each dipole is assumed to have a length *L*, a width *W*, and spaced from neighboring dipoles by distances *dx* in the x-direction and *dy* in the y-direction. The dipoles are thin as compared to their length (*W* << *L*) so that only the $\hat{a}_x$ directed currents are taken into account.

The dielectric slab Green's function representing the electric field at an arbitrary point on the surface of a grounded dielectric slab, $G_{xx}(x,y,d)$, due to an infinitesimal electric dipole of unit strength located at (x', y', d) on that grounded dielectric slab of thickness *d* and relative permittivity ε_r is expressed as [20], [21];

$$G_{xx} = \frac{-jZ_0}{4\pi^2 k_0} \int_{-\infty}^{\infty} \int_{-\infty}^{\infty} Q(k_x, k_y) e^{jk_x(x-x')} e^{jk_y(y-y')} dk_x dk_y \qquad (2.1.1)$$

where

$$Q(k_x,k_y)=\frac{(\varepsilon_r k_0^2-k_x^2)k_2\cos(k_1 d)+jk_1(k_0^2-k_x^2)\sin(k_1 d)}{T_e T_m}\sin(k_1 d) \tag{2.1.2}$$

$$T_e=k_1\cos(k_1 d)+jk_2\sin(k_1 d) \tag{2.1.3}$$

$$T_m=\varepsilon_r k_2\cos(k_1 d)+jk_1\sin(k_1 d) \tag{2.1.4}$$

$$k_1^2=\varepsilon_r k_0^2-\beta^2 \quad , \quad (\mathrm{Im}\,k_1<0) \tag{2.1.5}$$

$$k_2^2=k_0^2-\beta^2 \quad , \quad (\mathrm{Im}\,k_2<0) \tag{2.1.6}$$

$$\beta^2=k_x^2+k_y^2 \tag{2.1.7}$$

$$Z_0=\sqrt{\mu_0/\varepsilon_0} \text{ , intrinsic impedance of free - space} \tag{2.1.8}$$

$$k_0=\omega\sqrt{\mu_0\varepsilon_0} \text{ , free - space wave number} \tag{2.1.9}$$

Zeros of T_e and T_m functions correspond to the transverse electric (TE) and transverse magnetic (TM) surface wave poles, respectively, of the grounded dielectric slab.

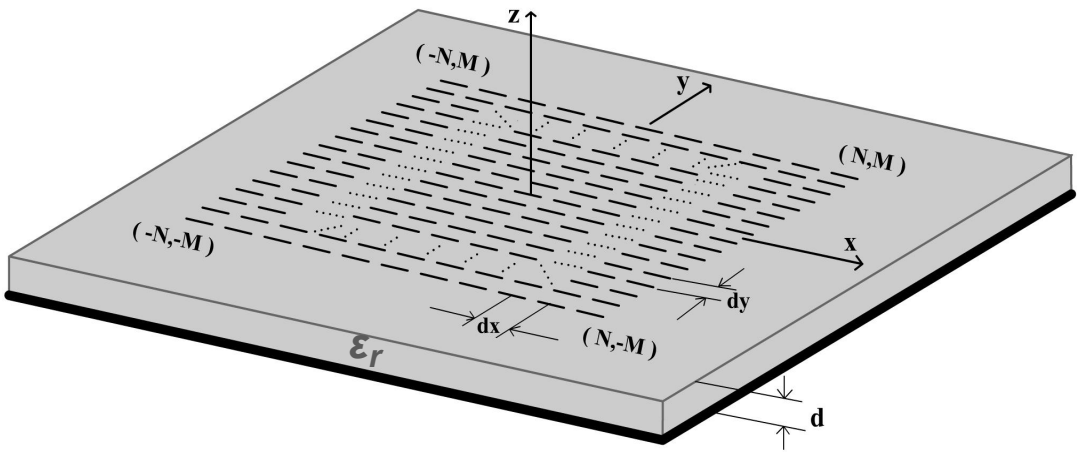

Figure 2.1 A planar, periodic rectangular array of (2N+1)(2M+1) identical x-directed printed dipoles on a grounded dielectric substrate

The *E-field* at *(x,y,d)* generated by the currents on the dipoles is ;

$$E_x^a(x,y,d) =$$

$$\frac{-jZ_0}{4\pi^2 k_0}\sum_{n=-N}^{N}\sum_{m=-M}^{M}\int_{-\infty}^{\infty}\int_{-\infty}^{\infty}\int_{x'}\int_{y'} Q(k_x,k_y)e^{jk_x(x-x')}e^{jk_y(y-y')}J_{nm}(x',y')dy'dx'dk_xdk_y \tag{2.1.10}$$

where *n* and *m* stand for the indices of the elements of array, taking on the integer values as $-N \le n \le N$ and $-M \le m \le M$. $J_{nm}(x',y')$ denote the current distribution on the $(n, m)^{\text{th}}$ dipole and are the equivalent sources that radiate E_x^a in the absence of dipoles.

E_x^a can be deduced if the observation points for the *E-field* are chosen as the points on the printed dipoles. Boundary condition for the *E-field* requires the tangential component of the total *E-field* to be zero on the dipoles:

$$E_x^{inc} + E_x^a = 0, \quad \text{on the dipoles} \tag{2.1.11}$$

where E_x^{inc} is the x-directed component of the excited *E-field* which is either due to delta gap voltages impressed at the central feed points on the dipole elements or due to an externally incident plane wave which is impinging on the whole array. The following expression is obtained after substituting (2.1.10) into (2.1.11):

$$E_x^{inc}(x,y,d) =$$

$$\frac{jZ_0}{4\pi^2 k_0}\sum_{n=-N}^{N}\sum_{m=-M}^{M}\int_{-\infty}^{\infty}\int_{-\infty}^{\infty}\int_{x'}\int_{y'} Q(k_x,k_y)e^{jk_x(x-x')}e^{jk_y(y-y')}J_{nm}(x',y')dy'dx'dk_xdk_y \tag{2.1.12}$$

where x and y correspond to the observation point that lie on the $(p\ ,\ q)^{\text{th}}$ element, p and q take the values $-N \le p \le N$ and $-M \le q \le M$.

Unknown dipole current on the $(n\ ,\ m)^{\text{th}}$ element, $J_{nm}(x', y')\hat{a}_x$, can be expanded as;

$$J_{nm}(x', y') \cong \sum_{i=1}^{I} A_{nm}^{i} f_i(x', y') \tag{2.1.13}$$

where I is the number of modes per dipole, A_{nm}^{i} are the unknown current coefficients, and $f_i(x', y')$ is the ith expansion (basis) function which is chosen as piecewise sinusoidal function;

$$f_i(x', y') = \frac{\sin(k_e(h - |x' - x_i^{nm}|))}{W \sin(k_e h)} \tag{2.1.14}$$

where h is the half-length of the expansion mode, x_i^{nm} and y_i^{nm} are the coordinates of the center of ith mode, k_e is the wave number of the expansion mode chosen as, [20]:

$$k_e = k_0 \sqrt{(\varepsilon_r + 1)/2} \tag{2.1.15}$$

Substituting (2.1.13) and (2.1.14) in (2.1.12) yields;

$$E_x^{inc}(x,y,d) =$$

$$\frac{jZ_0}{4\pi^2 k_0}\sum_{n=-N}^{N}\sum_{m=-M}^{M}\sum_{i=1}^{I}\int_{-\infty}^{\infty}\int_{-\infty}^{\infty}\int_{x'}\int_{y'} Q(k_x,k_y)e^{jk_x(x-x')}e^{jk_y(y-y')} \qquad (2.1.16)$$

$$A_{nm}^{i}\frac{\sin\left(k_e\left(h-\left|x'-x_i^{nm}\right|\right)\right)}{W\sin(k_e h)}dy'dx'dk_x dk_y$$

Since the RHS of Equation (2.1.12) is approximated as in (2.1.16) using (2.1.13), [RHS of (2.1.16) - $E_x^{inc}(x,y,d)$] produces error, *r*;

$$r = \left[RHS\ of\ (2.1.16)\right] - \left[E_x^{inc}(x,y,d)\right], \quad \text{residue} \qquad (2.1.17)$$

Applying the method of weighted residuals to minimize the error, inner product of *r* and weighting function should be zero:

$$\left\langle r, w_j(x,y)\right\rangle = 0 \qquad (2.1.18)$$

where $\langle .,. \rangle$ indicates inner product and $w_j(x,y)$ is the weighting function. Applying Galerkin method, weighting function is chosen the same as expansion function:

$$w_j(x,y) = \frac{\sin(k_e(h-|x-x_j^{pq}|))}{W\sin(k_e h)}, \qquad j = 1,2,.....J \qquad (2.1.19)$$

where *J=I* is the number of modes per dipole and (x_j^{pq}, y_j^{pq}) are the coordinates of the center of *j*th mode of (*p, q*)th element.

(2.1.19) is substituted in (2.1.18) and the inner product is performed, then the following equation is obtained:

$$\frac{jZ_0}{4\pi^2 k_0}\sum_{n=-N}^{N}\sum_{m=-M}^{M}\sum_{i=1}^{I}\int_{-\infty}^{\infty}\int_{-\infty}^{\infty}\iint_{x'\,y'\,x\,y} Q(k_x,k_y)e^{jk_x(x-x')}e^{jk_y(y-y')}$$

$$A_{nm}^{i}\frac{\sin(k_e(h-|x'-x_i^{nm}|))}{W\sin(k_e h)}\frac{\sin(k_e(h-|x-x_j^{pq}|))}{W\sin(k_e h)}dydxdy'dx'dk_x dk_y \qquad (2.1.20)$$

$$=\iint_{x\,y}E_x^{inc}(x,y)\frac{\sin(k_e(h-|x-x_j^{pq}|))}{W\sin(k_e h)}dydx$$

$E_x^{inc}(x,y)$ in (2.1.12) at the $(p, q)^{\text{th}}$ dipole can be expressed as:

$$E_x^{inc}(x,y)=\upsilon_{pq}e^{jk_0(ux+vy)}\delta\left(x-x_{[(J+1)/2]}^{pq}\right)\delta\left(y-y_{[(J+1)/2]}^{pq}\right) \qquad (2.1.21)$$

$$u=\sin\theta_s\cos\phi_s \qquad (2.1.22)$$

$$v=\sin\theta_s\sin\phi_s \qquad (2.1.23)$$

where ($x_{[(J+1)/2]}^{pq}$, $y_{[(J+1)/2]}^{pq}$) are the coordinates of the center of the $[(J+1)/2]^{\text{th}}$ mode of $(p,\text{q})^{\text{th}}$ element, i.e. actually the center of the $(p,\text{q})^{\text{th}}$ element when the number of modes, J, is chosen to be odd. $E_x^{inc}(x,y)$ in (2.1.21) corresponds to an impressed voltage $\upsilon_{pq}e^{jk_0\left(ux_{[(J+1)/2]}^{pq}+vy_{[(J+1)/2]}^{pq}\right)}$ at the center of each $(p,q)^{\text{th}}$ element to provide maximum radiation at the scan angle of (θ_s , ϕ_s) in the case of an antenna phased array radiation problem. The Equation (2.1.16) can also be solved for the passive array scattering problem by defining $E_x^{inc}(x,y)$ as an incident plane wave impinging on the array, but the analysis in this study is made for the radiation case

for the sake of simplicity. $d(x - x^{pq}_{[(J+1)/2]})$ and $d(y - y^{pq}_{[(J+1)/2]})$ are the Dirac delta functions to describe the corresponding delta-gap voltage generator at the center of each $(p,q)^{th}$ dipole element.

Equation (2.1.20) can be represented as a matrix equation:

$$[Z][I]=[V] \tag{2.1.24}$$

where [Z] is the matrix whose elements represent the mutual impedances between the modes of the elements in the array, $Z^{i,j}_{nm,pq}$:

$$Z^{i,j}_{nm,pq} = \frac{jZ_0}{4p^2 k_0} \int_{-\infty}^{\infty}\int_{-\infty}^{\infty} \int_{x'}\int_{y'}\int_{x}\int_{y} Q(k_x,k_y) e^{jk_x(x-x')} e^{jk_y(y-y')} A^i_{nm} \frac{\sin(k_e(h-|x'-x^{nm}_i|))}{W\sin(k_e h)} \frac{\sin(k_e(h-|x-x^{pq}_j|))}{W\sin(k_e h)} dydxdy'dx'dk_x dk_y \tag{2.1.25}$$

[I] is the vector having the elements that represent the unknown current amplitudes of the expansion modes:

$$[\mathrm{I}] = A^i_{nm} \tag{2.1.26}$$

[V] is the voltage excitation vector of elements that represent the impressed voltages at the center of each $(p,q)^{th}$ element, V^j_{pq}.

$$V^j_{pq} = \begin{cases} \frac{u_{pq}}{W} e^{jk_0(ux^{pq}_j + vy^{pq}_j)} & , \quad j=(J+1)/2 \\ 0 & , \quad j=1,2.....J, \quad j\neq(J+1)/2 \end{cases} \tag{2.1.27}$$

$Z^{i,j}_{nm,pq}$ in (2.1.25) can be written in a more suitable form as follows:

$$Z^{i,j}_{nm,pq} = \frac{jZ_0}{4\pi^2 k_0} \int_{-\infty}^{\infty} \int_{-\infty}^{\infty} Q(k_x,k_y) F^i_{nm}(k_x,k_y) F^{*j}_{pq}(k_x,k_y) dk_x dk_y \tag{2.1.28}$$

where

$$F^i_{nm}(k_x,k_y) = \int_{x'} \int_{y'} \frac{\sin(k_e(h-|x'-x_i^{nm}|))}{W \sin(k_e h)} e^{-jk_x x'} e^{-jk_y y'} dy' dx' \tag{2.1.29}$$

$$F^{*j}_{pq}(k_x,k_y) = \int_{x} \int_{y} \frac{\sin(k_e(h-|x-x_j^{pq}|))}{W \sin(k_e h)} e^{jk_x x} e^{jk_y y} dy dx \tag{2.1.30}$$

Integrals in (2.1.29) and (2.1.30) can be evaluated in closed form easily.

The integral in (2.1.28) needs treatment to be able to evaluate it numerically since it includes double infinite integral. This integral can be reduced to a finite integral and a semi-infinite integral by converting to polar coordinates (β,α) in the spectral domain:

$$Z^{i,j}_{nm,pq} = \frac{jZ_0}{4\pi^2 k_0} \int_{\beta=0}^{\infty} \int_{\alpha=0}^{2\pi} Q(k_x,k_y) F^i_{nm}(k_x,k_y) F^{*j}_{pq}(k_x,k_y) \beta d\beta d\alpha \tag{2.1.31}$$

where

$$k_x = \beta \cos\alpha \tag{2.1.32}$$

$$k_y = \beta \sin\alpha \tag{2.1.33}$$

The upper limit of semi-infinite integral in (2.1.31) cannot be taken as infinity in numerical integration. Discussion and more information on the choice of β value

as the upper limit where the integral converges can be found in [22]. In addition, convergence of the semi-infinite integral in (2.1.31) can be accelerated by subtracting the term representing the contribution of the current in a homogeneous medium from the Green's function of the dielectric slab and reinserting it as a separate integral as follows, [22]:

$$Z^{i,j}_{nm,pq} = Zh^{i,j}_{nm,pq} + \frac{jZ_0}{4\pi^2 k_0} \int_{\beta=0}^{\infty} \int_{\alpha=0}^{2\pi} [Q - Q^h] F^i_{nm} F^{*j}_{pq} \beta d\beta d\alpha \tag{2.1.34}$$

where $Zh^{i,j}_{nm,pq}$ is the mutual impedance between the modes of $(n,m)^{\text{th}}$ and $(p,q)^{\text{th}}$ elements in a grounded homogenous medium of effective relative permittivity $\varepsilon_e = (\varepsilon_r + 1)/2$. Details can be found in [22] about the Green's function of grounded homogeneous dielectric medium.

$$Zh^{i,j}_{nm,pq} = \frac{jZ_0}{4\pi^2 k_0} \int_{\beta=0}^{\infty} \int_{\alpha=0}^{2\pi} Q^h F^i_{nm} F^{*j}_{pq} \beta d\beta d\alpha \tag{2.1.35}$$

$$Q^h(k_x, k_y) = \frac{(\varepsilon_e k_0^2 - k_x^2)}{2j\varepsilon_e k_{1e}} (1 - e^{-2jk_{1e}d}) \tag{2.1.36}$$

$$k_{1e}^2 = \varepsilon_e k_0^2 - \beta^2 \tag{2.1.37}$$

Although the mutual impedance expression in (2.1.28) has been modified and improved as in (2.1.34) for the computational efficiency, this may not be enough for large array problems which may require excessive fill time for the [*Z*] matrix due to the convergence issue of (2.1.34). Since the number of modes used per dipole is directly related with the size of the [*Z*] matrix, it is reasonable to choose least possible number of modes to keep the size of the impedance matrix small. The choice of expansion mode as PWS function as in (2.1.14) and the wave number as

in (2.1.15) gives satisfactory results even when only one mode is used [20]. Thus one mode per dipole is taken in this study. Returning back to (2.1.24) with the choice of one mode per dipole:

$$[Z][I]=[V] \tag{2.1.24}$$

[Z], consisting of the elements $Z_{nm,pq}$ that corresponds to the mutual impedance between the $(n,m)^{th}$ and $(p,q)^{th}$ dipole elements, is a square matrix of size $[(2N+1)(2M+1)]^2$. [I] is a column vector of length $(2N+1)(2M+1)$ which contains the unknown current amplitudes, A_{nm}, of the dipole elements. [V] is also a column vector of length $(2N+1)(2M+1)$ whose elements are the impressed voltages, V_{pq}, at the center of the $(p,q)^{th}$ dipoles.

In the conventional MoM method, (2.1.24) is solved for the unknowns A_{nm} for the given values of excitation V_{pq}, by inverting the [Z] matrix which is of size $[(2N+1)(2M+1)]^2$. When N and M are large, the number of unknowns and the size of [Z] become very large resulting the solution of (2.1.24) to be highly inefficient. However the same problem can be solved faster and far more efficiently by using the present hybrid UTD-MoM approach which provides a drastic reduction in the number of unknowns, A_{nm}.

2.2 Summary of Asymptotic Analysis of Radiation/Scattering from Large Finite Arrays

It will be useful to make a brief explanation on the UTD [3] ray analysis of planar finite arrays, which constitutes the basis for UTD-MoM formulation.

Asymptotic high-frequency analysis for describing the fields of a large finite rectangular planar array of free-standing dipoles [16, 23, 24] and an array of

dipoles on an infinite grounded dielectric slab [18, 19] shows that the field at an observation point that is sufficiently far from the array truncation boundaries can be represented as a superposition of fields of a few rays arising from specific interior points and points at the truncation boundaries. These rays are illustrated in Figures 2.2a and 2.2b for a finite planar array of periodic elements on an infinite grounded dielectric slab for the scattering case and radiation case, respectively. The number of significant rays remains constant if the physical size of the array increases for a given frequency. The ray fields arising from the specific interior points of the array are related with the periodic structure Floquet modal waves that would exist on the corresponding infinite array. For the scattering case, the dominant Floquet modal ray is reflected specularly, obeying usual geometrical optics rules, on the other hand higher order propagating Floquet modal rays follow different type of reflected ray path, in an extended geometrical optics sense as shown in Figure 2.2a. For a given frequency, only a finite number of lower order modes are propagating away from the array surface, while the remaining infinite number of modes is evanescent normal to the array face. Additional surface rays launched from the corners and edge boundaries of the array exist as shown in Figure 2.2. The Floquet modal rays that make up the total field at an observation point P for the radiation case are illustrated in Figure 2.2b. Reflected Floquet mode rays are now replaced by incident Floquet modal rays in the radiation case.

It is noted that all of the propagating Floquet modal rays may not contribute to the total field at an observation point. Floquet modal wave contributions are discarded at those points if they arrive there originating from points outside the actual finite array. Thus the finiteness of the array introduces ray shadow boundaries for the Floquet modal field contributions. These Floquet ray shadow boundaries divide the observation space into the lit region, where Floquet ray contributions exist, and the shadow region where their contributions are discarded. Each propagating Floquet

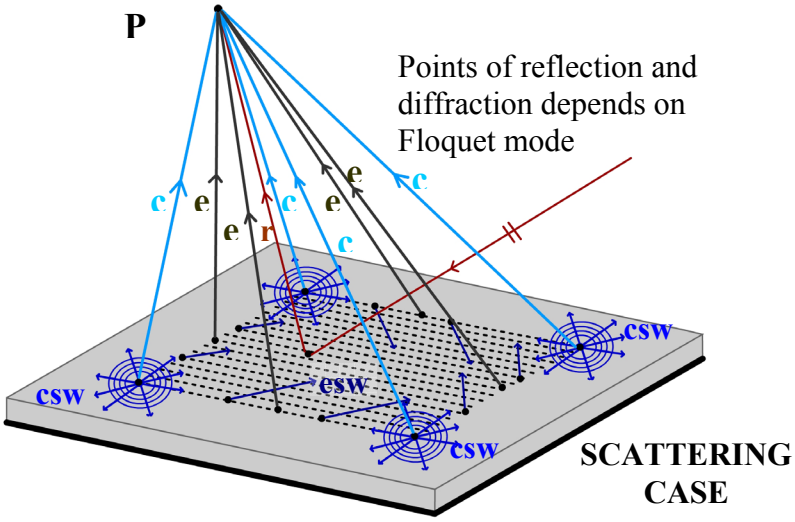

(a)

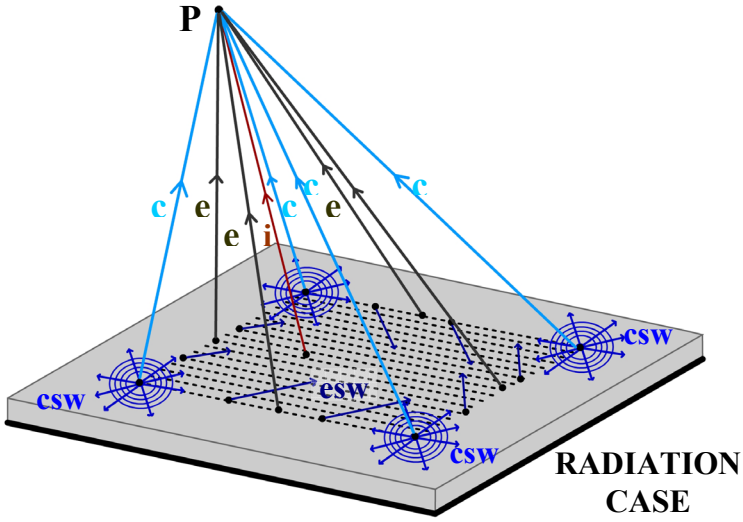

(b)

Figure 2.2 UTD Rays (a) for scattering by a planar, periodic rectangular array of printed elements. **r**: reflected Floquet Modal ray, **e**: edge diffracted Floquet Modal ray, **esw**: edge launched surface wave, **c**: corner diffracted Floquet Modal ray, **csw**: corner launched surface wave (b) for radiation by a planar, periodic rectangular array of printed elements. **i**: incident Floquet Modal ray. **c, e, csw, esw** are the same as defined for scattering case.

modal ray has its own ray shadow boundary since each Floquet mode has a different propagation direction.

Another aspect of the finiteness of the array is the diffraction of the Floquet modal rays at the array truncation boundaries. Those Floquet modal rays experience diffraction at the array edges and corners and produce edge/corner diffracted fields and edge/corner launched surface waves. Thus the total high-frequency field at an observation point can be given by the superposition of the fields of all the rays that arrive there such as the incident ray from direct path of source, the rays resultant from the diffraction of the incident rays at the array edges and corners and the surface rays launched from the array edges and corners again due to the diffraction of the incident rays. For example $E_x^a(x,y,d)$ in (2.1.10), the E-field at a point on the array surface can be expressed in terms of rays as follows:

$$E_x^a(x,y,d) \sim \sum_{j'=1}^{J_1} E_{j'}^{FM}(x,y) + \sum_{e=1}^{4}\sum_{j'=1}^{J_2} E_{j'}^{ed}(x,y) + \sum_{c=1}^{4}\sum_{j'=1}^{J_3} E_{j'}^{cd}(x,y) + \sum_{e=1}^{4}\sum_{j'=1}^{J_4} E_{j'}^{esw}(x,y) + \sum_{c=1}^{4}\sum_{j'=1}^{J_5} E_{j'}^{csw}(x,y) \tag{2.2.1}$$

where $E_{j'}^{FM}$ is the geometrical-optics-type incident Floquet ray field, $E_{j'}^{ed}$ and $E_{j'}^{cd}$ denote the edge and corner diffracted ray fields, and $E_{j'}^{esw}$ and $E_{j'}^{csw}$ denote the edge and corner launched surface waves produced by the *j*th Floquet mode respectively. *J* denotes the number of propagating Floquet modes and $J_{1,2,3,4,5} \le J$ since all of the incident Floquet modes may not reach the observation point due to the shadowing effects. Edge/corner diffracted or edge/corner launched surface rays of all incident Floquet modes also may not arrive the observation point. In most of the practical array designs, parameters are chosen such that only one Floquet mode

(the dominant mode) is excited. For this reason the UTD-MoM formulation to be developed in Section 2.3 is based only on the dominant Floquet mode and this practice gives quite sufficient results as shown in Chapter 3.

Edge diffracted Floquet modal ray is in the form of a modal summation of conical waves emanating from the array edges and compensates for the discontinuity of the associated Floquet mode across its shadow boundary arising from that edge. The location of the edge diffraction depends on the observation point. Edge diffraction produces both propagating and evanescent modes. The propagation constants of the propagating modes are less than the free space wave number and they diffract as diffraction cones, as shown in Figures 2.3a and 2.4a. Propagation constants of the evanescent modes are larger than the free space wave number so that they are guided along the edge but attenuate away from the edge, as shown in Figures 2.3b and 2.4b. Edge diffracted Floquet modes propagate as cylindrical waves [18].

Corner diffraction of the propagating Floquet modal ray occurs due to the element truncation of the array at the corner. Corner diffracted Floquet ray field is in the form of a spherical wave originating from the corner of the array. The Floquet corner diffracted field compensates for the discontinuity of the edge diffracted Floquet modal ray at the corresponding shadow boundary arising at the corner. Corner diffraction of a Floquet modal ray is illustrated in Figure 2.5.

Edge-excited surface waves are launched from the array edges due to the diffraction of Floquet modal waves. These waves have the same propagation constant as the surface waves of a grounded substrate that can exist also in the absence of the array.

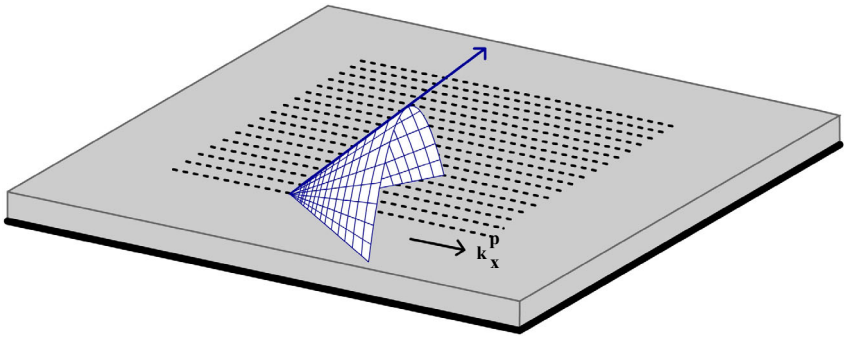

(a) Propagating mode, $(k_x^p)^2 < k_o^2$

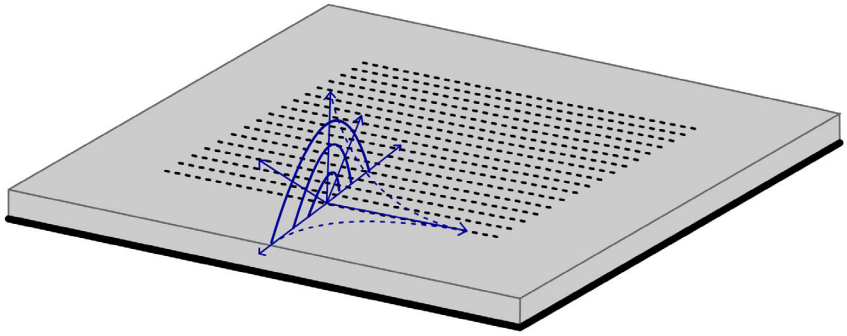

(b) Evanescent mode, $(k_x^p)^2 > k_o^2$

Figure 2.3 Edge diffracted Floquet wave rays from the x-directed edge (a) Propagating mode (b) Evanescent mode

Propagation constant of an edge-launched surface wave is matched to the Floquet modal wave number in the direction along the edge. These edge-excited complex waves exist in specific regions and disappear at the shadow boundary plane due to the truncation of the edge [18]. Figure 2.6 shows the ray picture illustrating the edge excited complex surface waves.

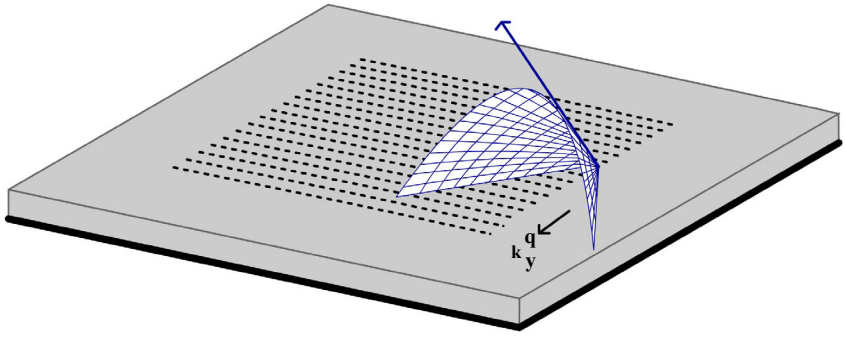

(a) Propagating mode, $(k_y^q)^2 < k_o^2$

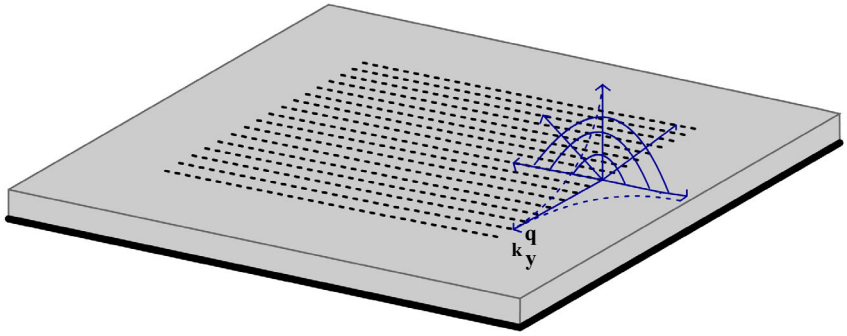

(b) Evanescent mode, $(k_y^q)^2 > k_o^2$

Figure 2.4 Edge diffracted Floquet wave rays from the y directed edge, (a) Propagating mode (b) Evanescent mode

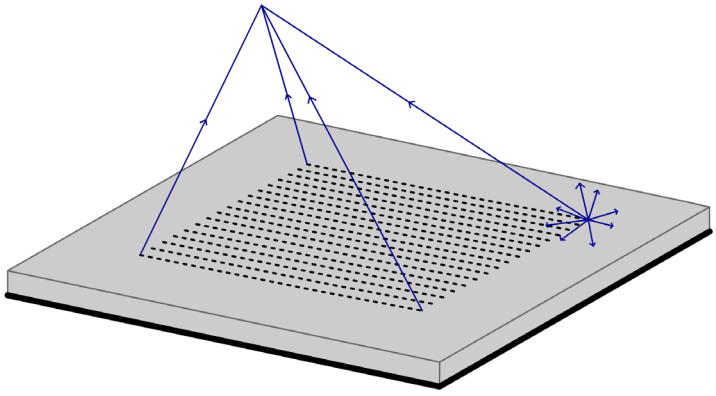

Figure 2.5 A ray picture illustrating the corner diffraction of Floquet modal ray.

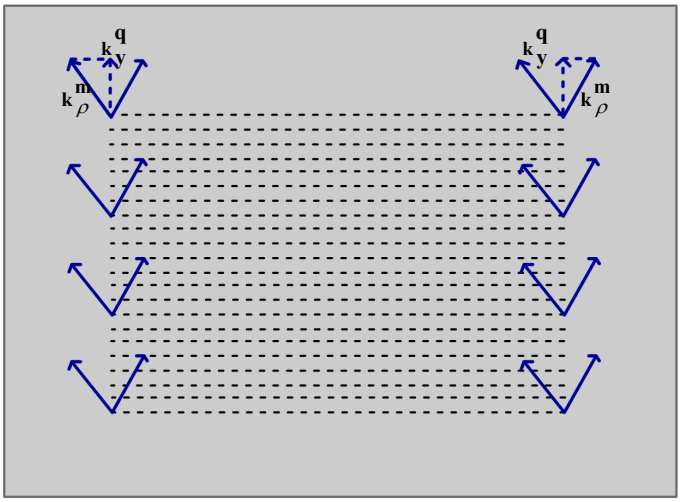

(a)

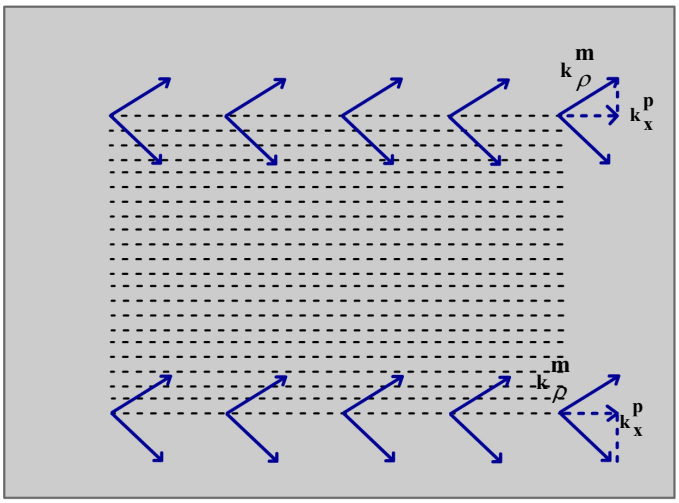

(b)

Figure 2.6 Edge-launched Floquet wave rays from the array edges (Top view), (a) the y directed edges (b) the x directed edges

Corner-excited surface waves are launched from the array corners due to the diffraction of Floquet modal waves as discussed before. As in the edge-excited case, these waves have the same propagation constant as the surface waves of a grounded substrate that can exist in the absence of the array. The corner-excited

complex waves have a cylindrical spreading factor. These surface waves compensate for the discontinuities of the corresponding edge-excited surface waves at the shadow boundary planes [18]. Figure 2.7 shows the ray picture illustrating the corner excited complex surface waves

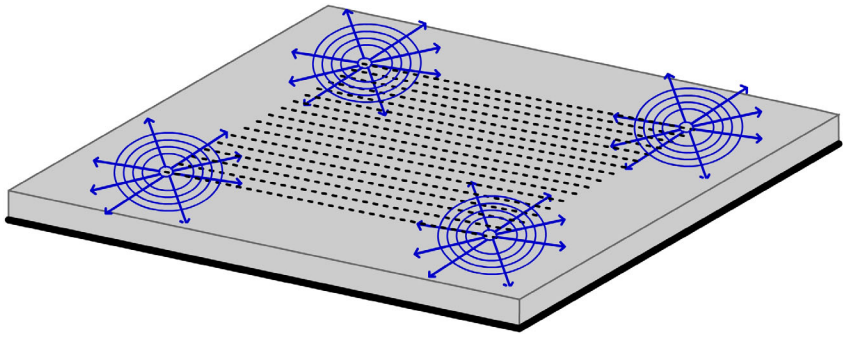

Figure 2.7 A ray picture illustrating the corner-excited complex surface waves

2.3 UTD-MoM Solution

In this section the hybrid UTD-MoM formulation is developed for the finite array of printed dipoles illustrated in Figure 2.1.

Conventional MoM formulation has been provided in Section 2.1 for the array under consideration. A matrix equation representation for an EFIE is obtained to be solved for the unknown current vector [I] of elements A_{nm} in (2.1.24). As emphasized at the end of Section 2.1, the solution to the unknown [I] eventually becomes inefficient as the number of elements in the array increases since inversion of the impedance matrix, [Z], of larger size is required. The present hybrid method handles the vector [I] to reduce the length, i.e. the number of unknowns, of it. With the guidance of Section 2.2, where asymptotic ray analysis of radiation/scattering from the array under consideration is summarized, it is assumed that the complex amplitudes A_{nm} of [I] also follow the UTD rules. This

enables [I] to be reformed by expanding it via a few UTD-type global basis functions. This technique is described below:

$$[\mathrm{I}]=[\mathrm{f}_{\text{UTD-MoM}}][\mathrm{I}'] \tag{2.3.1}$$

where $[\mathrm{f}_{\text{UTD-MoM}}]$ is the matrix having the elements as the values of UTD-MoM basis functions and $[\mathrm{I}']$ is the vector containing the new unknowns.

The procedure for evaluating $[\mathrm{f}_{\text{UTD-MoM}}]$ matrix is explained in the following paragraphs. The matrix Equation (2.1.24) then takes the form:

$$[\mathrm{Z}][\mathrm{f}_{\text{UTD-MoM}}][\mathrm{I}']=[\mathrm{V}] \tag{2.3.2}$$

To achieve Galerkin MoM solution, both sides of (2.3.2) is multiplied by the conjugate transpose of $[\mathrm{f}_{\text{UTD-MoM}}]$ to obtain the following equation;

$$[Z'][I'] = [V'] \tag{2.3.3}$$

where

$$[Z'] = \{\mathrm{conj}[\mathrm{f}_{\text{UTD-MoM}}]\}^{\mathrm{T}}[\mathrm{Z}][\mathrm{f}_{\text{UTD-MoM}}] \tag{2.3.4}$$

$[I']$: vector of new unknowns (2.3.5)

$$[V'] = \{\mathrm{conj}[\mathrm{f}_{\text{UTD-MoM}}]\}^{\mathrm{T}}[V] \tag{2.3.6}$$

It is worth noting that solution of (2.3.3) requires the inversion of $[\mathrm{Z}']$ matrix

whose size is now much more smaller than of [Z] matrix. After solving Equation (2.3.3) for [I′], current distribution of the array is obtained from Equation (2.3.1).

- **UTD-MoM Basis Functions and New Unknowns**

In the UTD-MoM concept, the array is divided into regions as *corner, edge*, and *inner* parts as depicted in Figure 2.8. Keeping the UTD ray behavior in mind, the complex amplitudes A_{nm} of the currents on the dipoles within array interior can be thought of as consisting of the infinite array value, i.e. propagating Floquet modal ray from direct path, together with the contributions from edge and corner diffracted rays and edge and corner launched surface waves. Thus it is reasonable to divide the array into a large inner part and a small remaining outer part as shown in Figure 2.8. Division of the array into regions cannot be done arbitrarily. According to the asymptotic high-frequency analysis of EM fields, a sufficient distance (at least one or two wavelengths) between the source and observation points is required to obtain accurate results. Assuming that the element spacing is $dx = dy = 0.5\lambda_0$, it is enough to choose edge parts as shown in Figure 2.8, which are only three cells away from the corresponding actual array edges. For a 19x19 element array each corner region has 15 elements. The remaining inner elements constitute the inner region. If the number of elements is increased greatly with inter-element spacing unchanged, i.e. $dx = dy = 0.5\lambda_0$, again it is enough to define edge regions as 3 cells away from the corresponding actual edges (edge regions now contains more elements) and corner regions as each having 15 elements. The remaining inner region now contains many more elements. Thus the determination of the regions is independent of the physical size of the array. Another crucial point is that, although the number of elements increased in the edge regions and inner part for the latter case, the number of unknowns remains the same, which is the advantageous and appealing characteristic of the present hybrid method. This is explained in the following paragraphs.

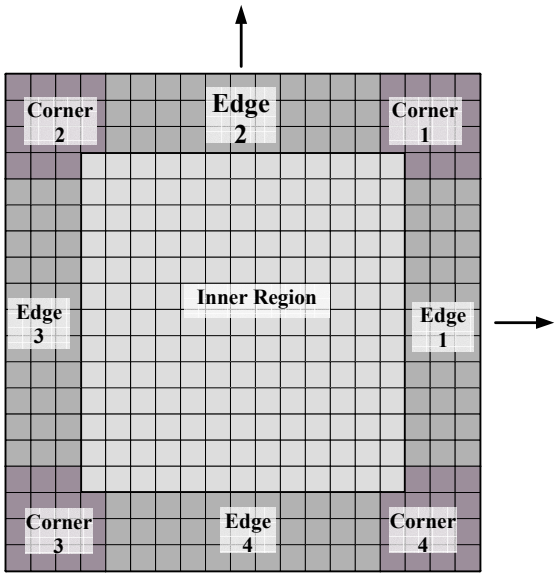

(a)

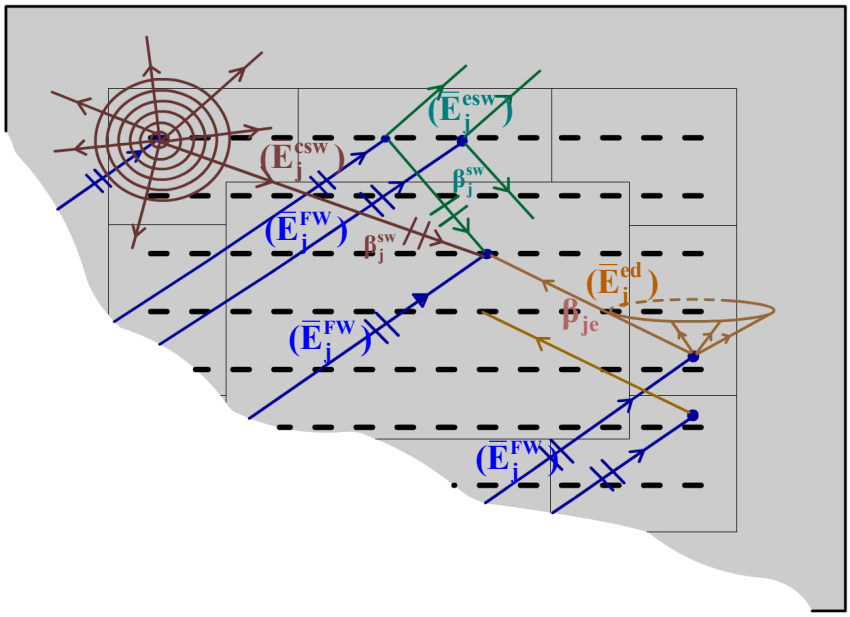

(b)

Figure 2.8 (a) Regions that the array is divided into in UTD-MoM approach (b) Ray fields that an element in the inner region experiences i.e. field from direct path, edge diffracted field, and edge and corner launched surface waves.

As mentioned at the beginning of this section, the unknown currents A_{nm} on the dipoles are expanded in terms of UTD-based global basis functions. According to the regional description of the elements the following expression can be used for A_{nm} as:

$$A_{nm} = \begin{cases} C_{-n+N+1,m+M+1}, & \text{for corner cells of the outer part} \\ E'_{nm} + A''_{nm}, & \text{for edge cells of the outer part} \\ A'_{nm} + A''_{nm}, & \text{for the inner part} \end{cases} \tag{2.3.7}$$

- **Inner part:** Elements in the "inner region" of the array experience the ray fields of Floquet modal waves from direct path, edge and corner diffracted waves of those Floquet modes, and edge and corner launched surface waves of those Floquet modes. The physical interpretation of each type of ray fields is given below.

$$A_{nm} = A'_{nm} + A''_{nm} \tag{2.3.8}$$

A_{nm} : Unknown current amplitudes of the elements in the "inner region".

A'_{nm} : Currents contributed by Floquet modal waves from direct path, edge and corner diffracted waves of those Floquet modes.

A''_{nm} : Currents contributed by edge and corner launched surface waves of the propagating Floquet modes

For the special case of J=1 (single propagating Floquet mode):

$$A'_{nm} = D_{nm} + \sum_{e=1}^{4} B_{nm}^{e} \; + \; \sum_{c=1}^{4} Q_{nm}^{c} \tag{2.3.9}$$

where

D_{nm}: Direct ray contribution of the dominant Floquet modal wave that corresponds to the infinite array value i.e. the field produced by an infinite periodic array.

$\sum_{e=1}^{4} B_{nm}^{e}$: Floquet edge-diffracted field contributions. Since the array is finite, the Floquet modal ray is truncated and diffracted at the array edges.

$\sum_{c=1}^{4} Q_{nm}^{c}$: Floquet corner-diffracted field contributions.

Functional forms of the terms that make up the equation (2.3.9) are as follows:

$$D_{nm} = \mathbf{D} V(ndx, mdy) e^{-j\beta_x ndx} e^{-j\beta_y mdy} \tag{2.3.10}$$

$$\beta_x = k \sin(\theta_s) \cos(\phi_s) \tag{2.3.11}$$

$$\beta_y = k \sin(\theta_s) \sin(\phi_s) \tag{2.3.12}$$

where (θ_s, ϕ_s) is the scan angle and k is the free-space wave-number. $V(ndx, mdy)$ is the feed voltage amplitude at the center of each $(n,m)^{\text{th}}$ dipole. In this study uniform excitation is assumed so that $V(ndx, mdy)=1$ for each of the

$(n,m)^{\text{th}}$ element. Choice of $V(ndx, mdy)$ for a tapered excitation also provides accurate results as in [25].

D: Unknown coefficient of the UTD-type global basis function representing the direct ray contribution of the dominant Floquet modal wave. It brings only one unknown for the inner region no matter how large the inner part is.

$$B_{nm}^{e} = \left(\frac{\mathbf{A_e}}{\sqrt{ks_e}} + \frac{\mathbf{B_e}}{\sqrt{(ks_e)^3}} + \frac{\mathbf{F_e}}{\sqrt{(ks_e)^5}} \right) e^{-jks_e} V(x_e, y_e) e^{-j\beta_x x_e} e^{-j\beta_y y_e} U_e \qquad (2.3.13)$$

where

(x_e, y_e): coordinates of the diffraction point on the edge.

$$x_e = x - \frac{\beta_x \left| y \mp Mdy \right|}{\sqrt{k^2 - \beta_x^2}} \quad , \quad -Ndx < x_e < Ndx \quad , \quad y_e = \pm Mdy \,(e = 2,4) \qquad (2.3.14)$$

$$y_e = y - \frac{\beta_y \left| x \mp Ndx \right|}{\sqrt{k^2 - \beta_y^2}} \quad , \quad -Mdy < y_e < Mdy \quad , \quad x_e = \pm Ndx \,(e = 1,3) \qquad (2.3.15)$$

s_e: distance between the diffraction point at the edge and the observation point (x,y) on the element.

$$s_e = \sqrt{(x - x_e)^2 + (y - y_e)^2} \qquad (2.3.16)$$

U_e: Heavy-side unit step function which cuts off the edge-diffraction defining the domain of existence. It takes the value of 1 if (x_e, y_e) lies on the true edge, 0 otherwise.

A_e, B_e, F_e: Unknown coefficients of the UTD-type global basis functions for the edge diffracted propagating Floquet modal ray. They bring 12 unknowns for all the elements at which the edge diffraction contributions are included.

Q_{nm}^{c}: corner diffraction from the cth corner (2.3.17)

The contributions resultant from corner diffraction can be excluded because the effects of edge diffraction is much more dominant in comparison when any $(n,m)^{th}$ cell is not within approximately 2 wavelengths from an array corner. In the vicinity of array corners, the effect of corner diffraction on A_{nm} is already included through $C_{-n+N+1,m+M+1}$ of (2.3.7).

Again for the special case of J=1 (only one propagating Floquet mode):

$$A''_{nm} = A''_1 + A''_2 \tag{2.3.18}$$

where

A''_1: Edge-excited surface wave contributions. Surface waves are launched from the array edges due to the diffraction of incident Floquet modal waves.

A''_2: Corner-excited surface wave contributions. These surface waves are launched from the array corners due to the diffraction of Floquet modal waves as discussed before.

Functional forms of the terms that make up the equation (2.3.18) are as follows:

$$A_1'' = \sum_{e=1}^{4} \mathbf{G_e} f(f_e') \frac{e^{-jb_{sw}s_e'}}{k_t} V(x_e', y_e') e^{-jb_x x_e'} e^{-jb_y y_e'} U_e' \tag{2.3.19}$$

(x_e', y_e') : The point at the edge at which the surface wave is launched.

$$x_e' = x - \frac{b_x \left| y \mp Mdy \right|}{\sqrt{b_{sw}^2 - b_x^2}} \quad , \quad -Ndx < x_e' < Ndx \quad , \quad y_e' = \pm Mdy (e = 2,4) \tag{2.3.20}$$

$$y_e' = y - \frac{b_y \left| x \mp Ndx \right|}{\sqrt{b_{sw}^2 - b_y^2}} \quad , \quad -Mdy < y_e' < Mdy \quad , \quad x_e' = \pm Ndx (e = 1,3) \tag{2.3.21}$$

s_e': distance between the point where the surface wave is launched at the edge and the observation point (x,y) on the element.

$$s_e' = \sqrt{(x - x_e')^2 + (y - y_e')^2} \tag{2.3.22}$$

$$k_t = \begin{cases} \sqrt{b_{sw}^2 - b_x^2} & ; \quad e = 2,4 \\ \sqrt{b_{sw}^2 - b_y^2} & ; \quad e = 1,3 \end{cases} \tag{2.3.23}$$

b_{sw}: surface wave propagation constant of the grounded dielectric slab.

U_e': Heavy side unit step function. It takes the value of 1 if (x_e', y_e') lies on the true edge, 0 otherwise.

$f(f') = \cos^2(f') \equiv \mathrm{H_y}$ TM surface wave pattern (2.3.24)

f'_e: Angles of shadow boundaries for the edges

$$f'_e = \begin{cases} -j'_{ex} & ; e = 2 \\ +j'_{ex} & ; e = 4 \\ -(\frac{p}{2} - j'_{ey}) + \text{sgn}(b_y) * p & ; e = 1 \\ +(\frac{p}{2} - j'_{ey}) & ; e = 3 \end{cases} \quad (2.3.25)$$

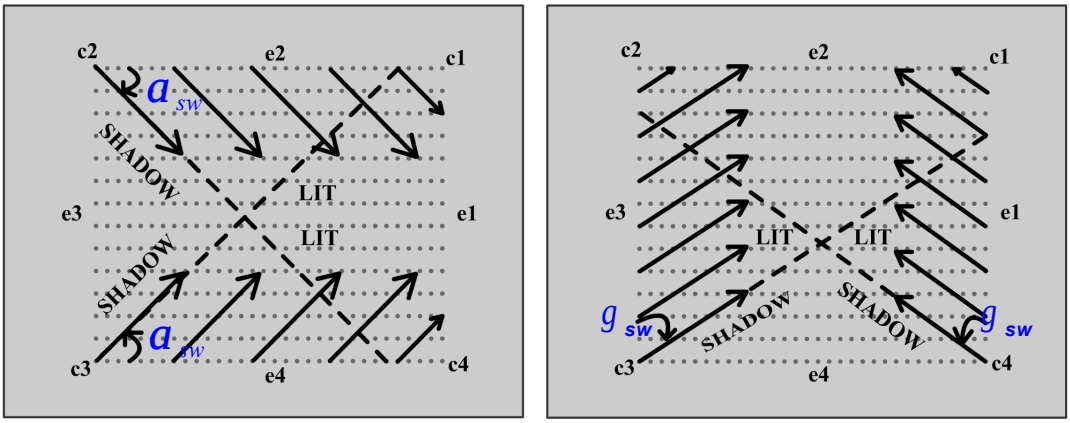

Figure 2.9 Shadow boundaries for x and y directed edges respectively

$$a_{sw} = \cos^{-1}(b_x / b_{sw})$$
$$f'_{e2} = -a_{sw} \quad (2.3.26)$$
$$f'_{e4} = +a_{sw}$$

$$g_{sw} = \cos^{-1}(b_y / b_{sw})$$
$$f'_{e1} = \frac{p}{2} + g_{sw} \quad (2.3.27)$$
$$f'_{e3} = \frac{p}{2} - g_{sw}$$

$\mathbf{G_e}$: Unknown coefficients of the UTD-type global basis function for the edge launched surface wave. It brings 4 unknowns for all the elements at which the edge excited surface wave contributions are included.

Again for the special case of J=1 (only one propagating Floquet mode):

$$A_2'' = \sum_{c=1}^{4} \left\{ \frac{\mathbf{G_{cx}} f(f_c) F(d'_{cx}) \operatorname{sgn}(x_c)}{(b_{sw}\cos(f_c) - b_x)} + \frac{\mathbf{G_{cy}} f(f_c) F(d'_{cy}) \operatorname{sgn}(y_c)}{(b_{sw}\sin(f_c) - b_y)} \right\} \frac{e^{-jb_{sw}s_c}}{\sqrt{2p\, jb_{sw}s_c}} V(x_c, y_c) e^{-jb_x x_c} e^{-jb_y y_c} \tag{2.3.28}$$

(x_c, y_c) : coordinates of the corresponding corners.

$$x_c = \begin{cases} +Ndx & ; c = 1,4 \\ -Ndx & ; c = 2,3 \end{cases}$$
$$y_c = \begin{cases} +Mdy & ; c = 1,2 \\ -Mdy & ; c = 3,4 \end{cases} \tag{2.3.29}$$

s_c : distance between the cth corner and the observation point.

$$s_c = \sqrt{(x - x_c)^2 + (y - y_c)^2} \tag{2.3.30}$$

$$f_{ci} = \tan^{-1}\left(\frac{y - y_{ci}}{x - x_{ci}}\right) + (\operatorname{sgn}[y - y_{ci}] - 1)p/2 \quad ; i = 1,\ldots,4 \tag{2.3.31}$$
$$\text{where} \quad 0 \le \tan^{-1}(q) \le p$$

$$d'_{cx} = 2b_{sw}s_c \sin^2\left(\frac{f_c - f'_{cx}}{2}\right)$$
$$d'_{cy} = 2b_{sw}s_c \sin^2\left(\frac{f_c - f'_{cy}}{2}\right) \qquad (2.3.32)$$

$$f'_{cx} = \begin{cases} f'_2(e=2) & ; c=1,2 \\ f'_4(e=4) & ; c=3,4 \end{cases}$$
$$f'_{cy} = \begin{cases} f'_1(e=1) & ; c=1,4 \\ f'_3(e=3) & ; c=2,3 \end{cases} \qquad (2.3.33)$$

$F(x) = 2j\sqrt{x}e^{jx}\int_{\sqrt{x}}^{\infty} e^{-jt^2}dt$, UTD Fresnel Transition Function
$f(f) = \cos^2(f)$, H_y TM surface wave pattern (2.3.34)

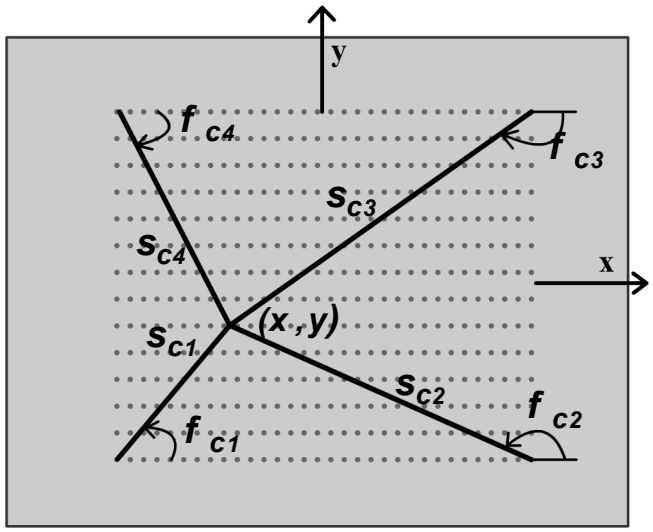

Figure 2.10 Surface waves launched from corners

$\mathbf{G_{cx}}, \mathbf{G_{cy}}$: Since A''_2 compensates for the discontinuities of the corresponding edge-excited surface waves at the shadow boundary planes, $\mathbf{G_{cx}}$ and $\mathbf{G_{cy}}$ contribute no new unknowns (see Equations 2.3.35 and 2.3.36 below).

$$G_{cx} = \begin{cases} G_2 & ; \ c = 1,2 \\ G_4 & ; \ c = 3,4 \end{cases} \tag{2.3.35}$$

$$G_{cy} = \begin{cases} G_1 & ; \ c = 1,4 \\ G_3 & ; \ c = 2,3 \end{cases} \tag{2.3.36}$$

- **Edge Part:** Similarly, elements in the "edge" parts of the array experience the ray fields of: Floquet modal waves from direct path, edge and corner diffracted waves of those Floquet mode rays, and edge and corner launched surface waves resultant from the diffraction of those Floquet mode rays.

$$A_{nm} = E'_{nm} + A''_{nm} \tag{2.3.37}$$

A_{nm} : Unknown current amplitudes of the elements in the "edge" parts.

E'_{nm} : Currents contributed by Floquet modal waves from direct path, edge and corner diffracted waves of those Floquet modes.

A''_{nm} : Currents contributed by edge and corner launched surface waves of the propagating Floquet modes

For the special case of J=1 (only one propagating Floquet mode):

$$E'_{nm}(l,j) = H_{nm}^{lj} + \sum_{e=1,e\neq l}^{4} B_{nm}^{e} + \sum_{c=1}^{4} Q_{nm}^{c} \tag{2.3.38}$$

where

H_{nm}^{lj}: Direct ray contribution of the dominant Floquet modal wave which represents the field produced by an infinite periodic array.

$\sum_{e=1,\, e\neq\ell}^{4} B_{nm}^{e}$: Floquet edge-diffracted fields, as explained in "Inner Part" section. The only difference is that, for an element belonging to *e*th edge, the field contribution resultant from the ray diffraction at the corresponding edge is excluded. This is due to the ray theory that requires a separation of at least one λ_0 between the source and observation points.

$\sum_{c=1}^{4} Q_{nm}^{c}$: Floquet corner-diffracted field contributions.

Functional forms of the terms that make up the equation (2.3.38) are as follows:

$$H_{nm}^{lj} \approx \mathbf{H_{lj}} V(ndx, mdy) e^{-j\beta_x ndx} e^{-j\beta_y mdy} \tag{2.3.39}$$

$\mathbf{H_{lj}}$: Unknown coefficient of the UTD-type global basis function representing the direct ray contribution of the dominant Floquet modal wave i.e. the infinite array value. It brings only one unknown for the elements on the *j*th row/column of *l*th edge.

B_{nm}^{e}: The same as explained in "Inner Part" section. (See Equation (2.3.13))

Q_{nm}^{c} : The same as explained in "Inner Part" section. (See Equation (2.3.17))

A_{nm}'' **:** The same as explained in "Inner Part" section. (See Equation (2.3.18))

The substantial reduction in the number of unknowns is made possible by using the UTD ray-type global basis functions that have been defined by the Equations (2.3.7) through (2.3.39). Assume that the array to be analyzed is divided into regions as shown in Figure 2.8a. Corner regions will bring 4x15 = 60 unknowns (each corner has 15 elements/unknowns). Edge regions will bring 4x3 = 12 unknowns (each edge has 3 rows/columns and each row/column has one unknown i.e. infinite array value). The inner region has only 1 unknown i.e. the infinite array value. The infinite array values defined for the elements in the inner and edge regions are contributed by the edge-diffracted rays that bring 12 unknowns (A_e, B_e, F_e, where e = 1,..,4) and the edge and corner launched surface waves that bring 4 unknowns (G_e, where e = 1,..,4). Total number of unknowns is then 89 for this hybrid approach. If that array contains 100x100 = 10000 elements, the number of unknowns equals to at least 10000 (in the case of one mode per element is taken) in the conventional MoM approach.

Example: In this example, expansion of the unknown current on an element in the inner region is illustrated. The array consists of 7x7 elements as shown in Figure 2.11. Actually this array is small to analyze with this hybrid approach. It is chosen just to show how the new $[Z']$ matrix elements are calculated. The element under consideration has the unknown coefficient $A_{1,2}$ as shown in Figure 2.11.

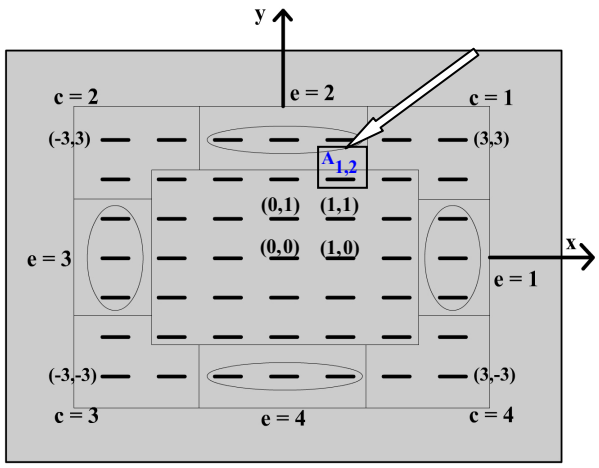

Figure 2.11 A 7x7 array of printed dipoles.

Figure 2.11 shows the regions that the array is divided into using UTD-MoM approach. If one mode per dipole is taken, there are 7x7 = 49 unknowns to be solved for in the conventional MoM approach. This number reduces to 33 if UTD-MoM method is used with the regions defined as in Figure 2.11.

Figure 2.12 shows the expansion of conventional unknown currents for this example according to the Equation 2.3.1:

$$[\mathrm{I}]=[\mathrm{f}_{\text{UTD-MoM}}][\mathrm{I}'] \tag{2.3.1}$$

It should be noted that the black squares in $[\mathrm{f}_{\text{UTD-MoM}}]$ (Fig. 2.12) matrix do not represent the same value. They are calculated according to the equations provided in Section 2.3.

For example let's consider the expansion of $\mathrm{A}_{1,2}$. This current amplitude belongs to an element in the *inner* region and the terms in the expression below are calculated according to the Equations 2.3.8 through 2.3.39.

$$A_{(1,2)} = \mathbf{D}V(dx,2dy)e^{-jb_x dx}e^{-2jb_y dy}$$

$$+\sum_{e=1}^{4}\left(\frac{\mathbf{A_e}}{\sqrt{ks_e}}+\frac{\mathbf{B_e}}{\sqrt{(ks_e)^3}}+\frac{\mathbf{F_e}}{\sqrt{(ks_e)^5}}\right)e^{-jks_e}V(x_e,y_e)e^{-jb_x x_e}e^{-jb_y y_e}U_e$$

$$+\sum_{e=1}^{4}\mathbf{G_e}f(f'_e)\frac{e^{-jb_{sw}s'_e}}{k_t}V(x'_e,y'_e)e^{-jb_x x'_e}e^{-jb_y y'_e}U'_e$$

$$+\sum_{c=1}^{4}\left\{\frac{\mathbf{G_{cx}}f(f_c)F(d'_{cx})\mathrm{sgn}(x_c)}{(b_{sw}\cos(f_c)-b_x)}+\frac{\mathbf{G_{cy}}f(f_c)F(d'_{cy})\mathrm{sgn}(y_c)}{(b_{sw}\sin(f_c)-b_y)}\right\}$$

$$\frac{e^{-jb_{sw}s_c}}{\sqrt{2p\,jb_{sw}s_c}}V(x_c,y_c)e^{-jb_x x_c}e^{-jb_y y_c}$$

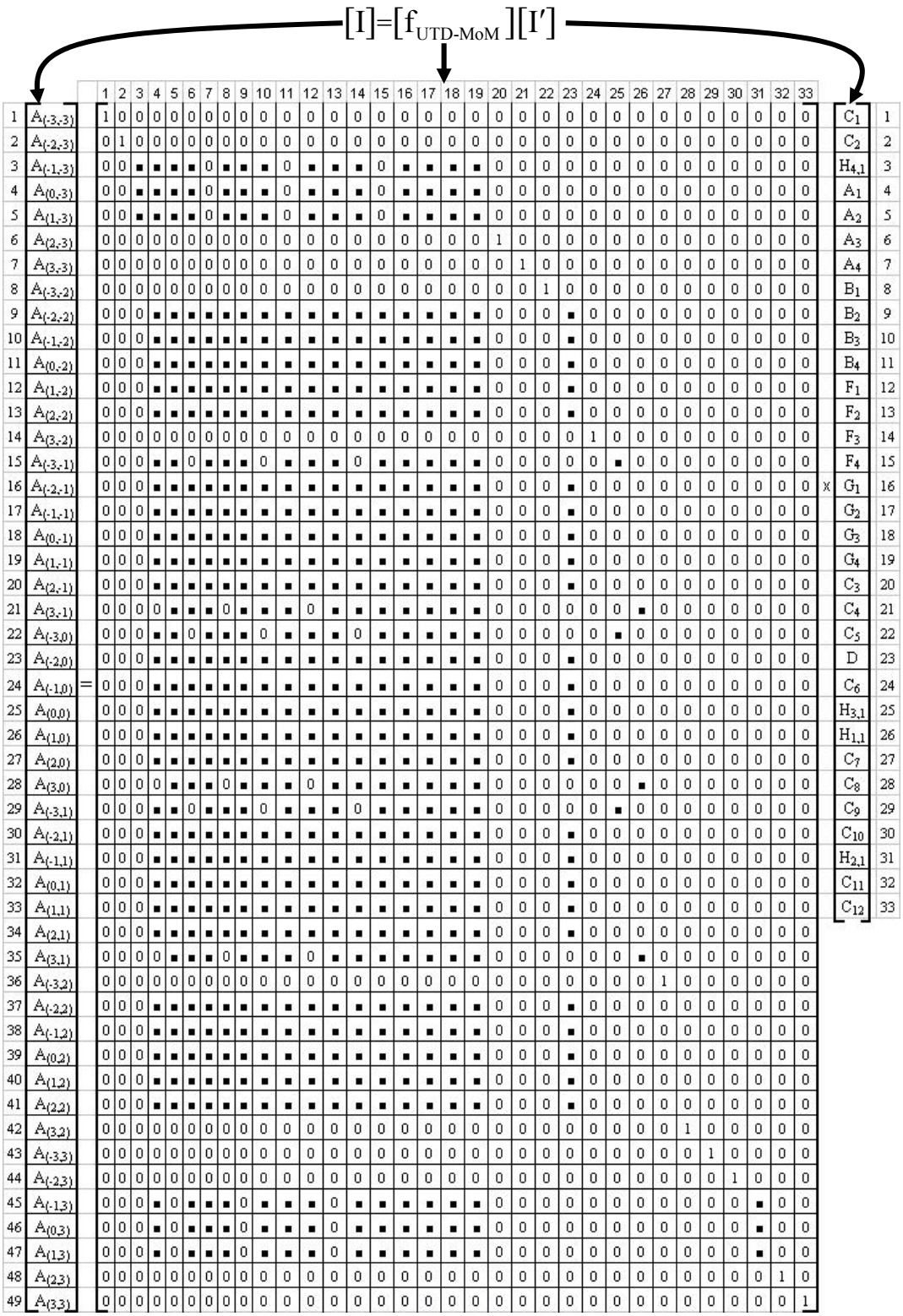

Figure 2.12 Expansion of conventional unknown currents in terms of UTD-MoM unknowns

CHAPTER 3

NUMERICAL RESULTS

In this chapter, numerical results obtained via the hybrid UTD-MoM approach developed in Section 2.3 are presented for the element currents on the array under consideration. These results are compared with the results of the conventional MoM solution, the method in [17] and the infinite array solution to demonstrate the accuracy, efficiency and robustness of the present hybrid method.

The UTD-MoM approach is applied to the analysis of radiation from the finite array of printed dipoles on an infinite grounded slab shown in Figure 2.1. In the numerical results shown in this chapter the array is assumed to be consisting of 19x19 printed dipole elements. Three different cases are investigated to test the accuracy and robustness of the current UTD-MoM method. In all three cases it is assumed that the array is excited uniformly in amplitude, so that $V_{nm} = 1$ for each of the $(n,m)^{th}$ dipoles. Another condition common to all three cases is the periodic spacing of the dipoles that are $dx = 0.5\lambda_0$ and $dy = 0.5\lambda_0$, in the $\hat{a}_x$ and $\hat{a}_y$ directions, respectively. Keeping these element spacings in mind, the array is divided into regions such that each corner region consists of 15 elements and each edge region consists of 3 rows or columns, as shown in Figure 3.1. The remaining elements constitute the large inner part. This configuration produces 89 unknown element currents to be solved for, whereas it is 361 in the conventional MoM approach. Solution of this problem via UTD-MoM approach for the unknown element currents requires the inversion of $[Z']$ matrix (see Equation 2.3.3) of size 89^2. If the same problem is handled via conventional MoM approach, the solution requires the inversion of the impedance matrix $[Z]$ (see Equation 2.1.24) of size 361^2. If the number of elements in the array is increased, for example to 101x101 =

10201, the number of unknowns thus the size of the [Z′] matrix to be inversed remains the same as 89 and 89^2 respectively (provided that the array is divided into the same electrical regions) in the present UTD-MoM approach, whereas the number of unknowns increases to 10201 and the size of the impedance matrix [Z] becomes 10201^2 in the conventional MoM approach. This example indicates the superior feature of the present hybrid method in terms of computational efficiency.

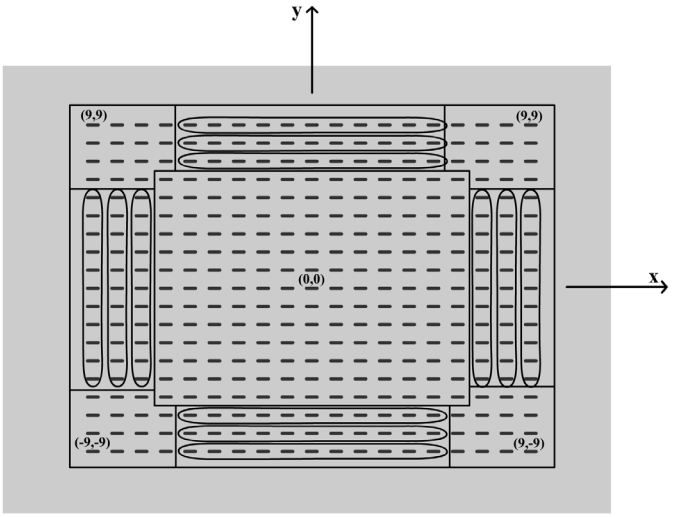

Figure 3.1 (Top view) Division of a 19x19 printed dipole array into regions.

Accuracy of the present UTD-MoM method is demonstrated for three cases. In the first case, an electrically thin ($d = 0.06\lambda_0$) dielectric substrate of relative permittivity $\varepsilon_r = 2.55$ is chosen. In the second case, all the parameters are the same as in the first case except for the thickness of the substrate which is increased to $d = 0.19\lambda_0$. In the third case, all the parameters are the same as in the first case except that relative permittivity of the slab is increased to $\varepsilon_r = 12.8$ and length of dipoles is decreased to $L = 0.156\lambda_0$. The aim of choosing three different cases in terms of substrate thickness or its relative permittivity is to find out how well the present hybrid method can handle the effects of surface waves. Surface waves are trapped in the substrate and travel parallel to the ground plane, thus don't

contribute to the array radiation at the scan angle and a part of the power is wasted. Both TE and TM surface waves can be excited on a grounded dielectric substrate and the number of surface wave modes and how strong they are excited depend on the material and thickness of the slab. For the accurate prediction of the array performance, the mutual coupling effects of surface waves must be included in the analysis. In the conventional MoM formulation, the surface wave contributions are included in the evaluation of impedance matrix elements. The present hybrid method also accounts for the mutual coupling of the surface waves. TM_0 mode surface wave has a zero cut-off frequency so that it can be excited for any substrate of thickness *d*. For thin substrates ($d < 0.01\lambda_0$) surface wave contribution is generally not significant [26]. However, as the thickness or/and relative permittivity of the dielectric substrate increase, surface wave(s) is/are better excited and coupling to the lower order mode(s) can become stronger. This condition is realized by increasing the thickness of the dielectric substrate in Case 2 and increasing the relative permittivity of the slab in Case 3. Results are in very good agreement with the conventional MoM results for both cases, thus the present hybrid method is capable of including the surface wave effects successfully. In all three cases, for the sake of simplicity, only one surface wave (TM_{10}) is excited although the present hybrid method can handle problems with more than one surface wave. Besides, in practical applications, designs are made such that the least possible number of surface waves is excited since they cause power loss reducing the efficiency of the antenna.

Case 1 The geometry of the problem is the same as in Figure 2.1 with 19x19 dipole elements printed on an infinite grounded dielectric slab. Dipoles are oriented in the $\hat{a}_x$ direction. The dielectric substrate is electrically thin ($d = 0.06\lambda_0$) with relative permittivity $\varepsilon_r = 2.55$ so that the dielectric slab surface wave is not well excited. Each dipole has a length $L = 0.39\lambda_0$, a width $W = 0.01\lambda_0$, and spaced from

neighboring dipoles by distances $dx=0.5\lambda_0$ in the x-direction and $dy=0.5\lambda_0$ in the y-direction.

Results are obtained for near-broadside ($\theta_s = 10^o$) and off-broadside ($\theta_s = 60^o$) radiations and compared with three different results; i.e. conventional MoM, the method used in [17] and the infinite array solution. As seen from the figures, the hybrid solution compares very well with the conventional MoM solution for both the near-broadside ($\theta_s = 10^o$) and off-broadside ($\theta_s = 60^o$) radiations. As seen on the figures, the infinite array value approximates the current distribution on the elements far from the edges whereas it becomes more inaccurate for the element near edges. The current magnitudes obtained from the method in [17] seem to follow the conventional MoM current pattern with less accuracy as compared to the present method. The method in [17] is the same as the method in this study except for the Galerkin solution used in this study. In [17], the unknown element currents are expanded the same way as explained in this study using UTD-type global functions, but those expansion functions are tested in point-matching fashion on some elements in the interior region whose locations are chosen by the user. Thus the accuracy of that method depends on the locations of the testing functions. However the method developed in this study doesn't need that kind of manipulation since Galerkin solution is applied, which makes the present hybrid method robust.

The present hybrid method may not provide accurate results at scan angles near grazing. This is due to the ill-conditioned character of $[Z']$; as the scan angle becomes large, the condition of the $[Z']$ matrix in (2.3.3) becomes large and eventually inversion of $[Z']$ matrix can not be carried out properly since it is nearly singular. (In this study it is observed that simulation terminates for $\theta_s > 75^o$ giving singularity error)

The current distributions on the first 3 rows (1st, 2nd and 3rd rows), on the middle 3 rows (9th, 10th, and 11th rows), on the last 3 rows (17th,18th, and 19th rows) and on the first 3 columns (1st, 2nd and 3rd columns), on the middle 3 columns (9th, 10th, and 11th columns), on the last 3 columns (17th,18th, and 19th columns) are plotted for $\theta_s = 10^o$ in Figures 3.2~3.7. Since $\phi_s = 0$, symmetric rows with respect to the middle row have the same current distributions. For this reason, for $\theta_s = 60^o$ in Case 1 and for the other 2 cases, first three rows, 9th and 10th rows (10th row is the middle row) are plotted, 11th row and last three rows are not plotted due to the symmetry. E-plane radiation patterns for the E_θ component in the case of scan angles $\theta_s = 10^o$ and $\theta_s = 60^o$ are shown in Figure 3.13.

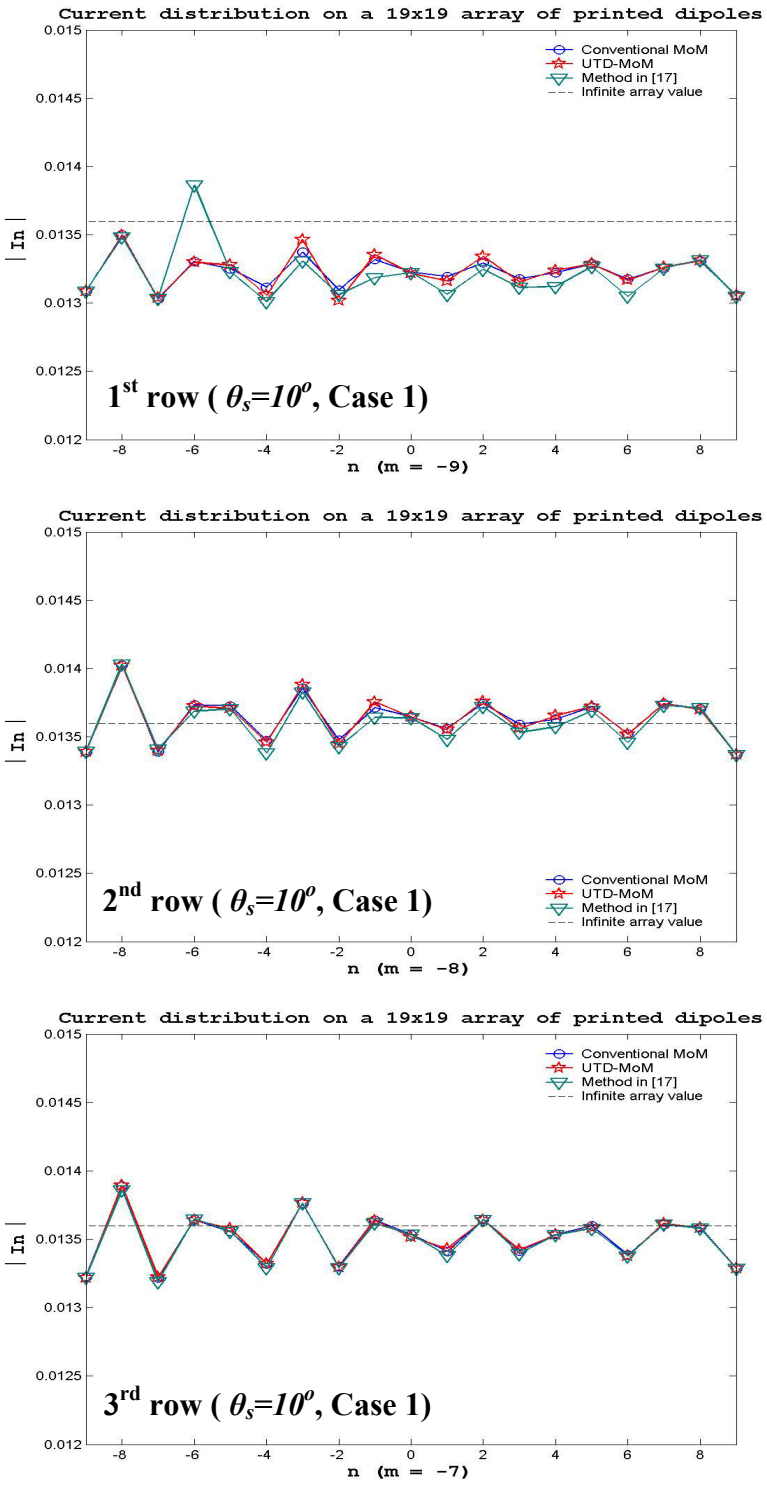

Figure 3.2 Element currents on the first three rows for Case 1 at $\theta_s = 10^o$; graph on the top is for the first row, graph in the middle is for the second row, graph at the bottom is for the third row

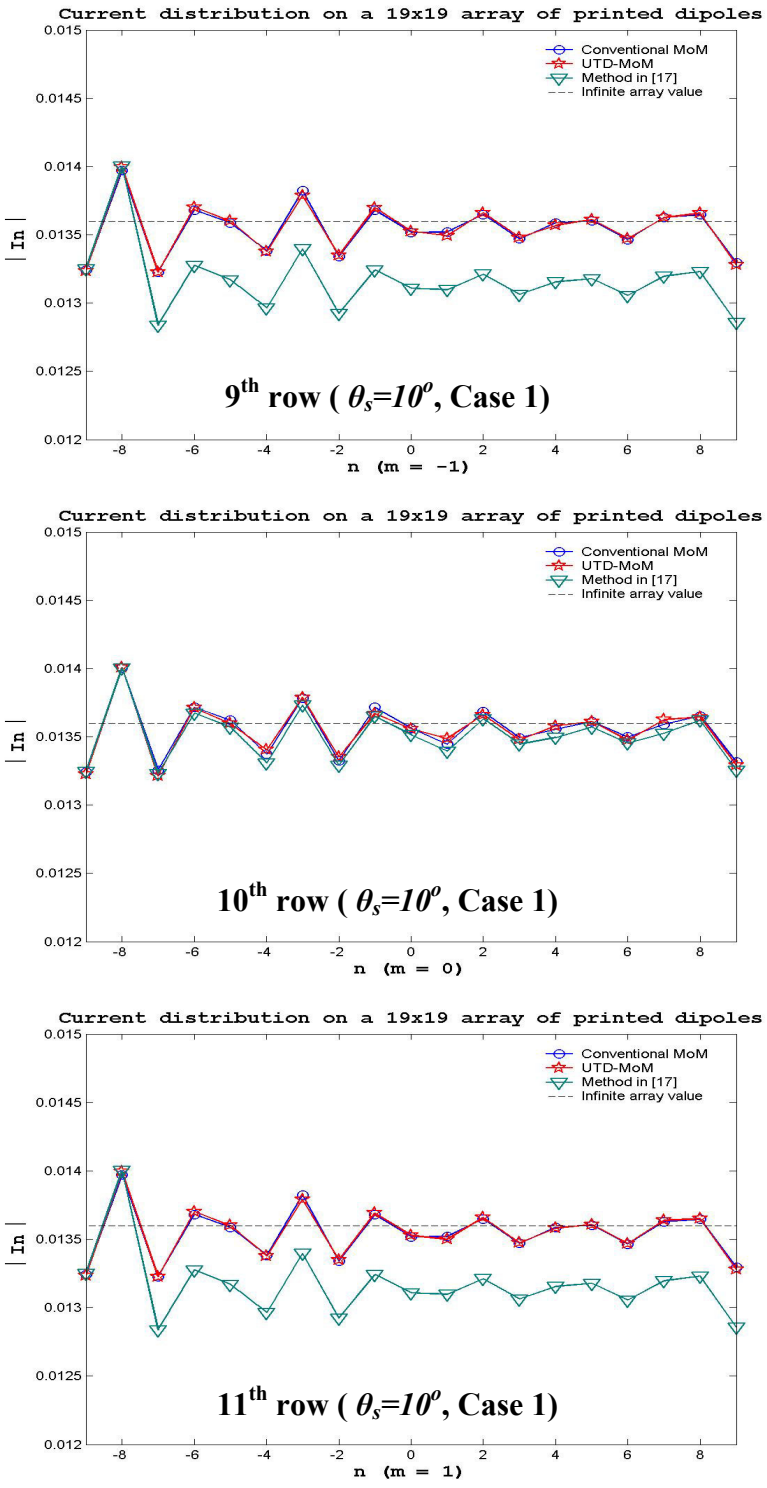

Figure 3.3 Element currents on the middle three rows for Case 1 at $\theta_s = 10^o$; graph on the top is for the 9th row, graph in the middle is for the 10th row, graph at the bottom is for the 11th row.

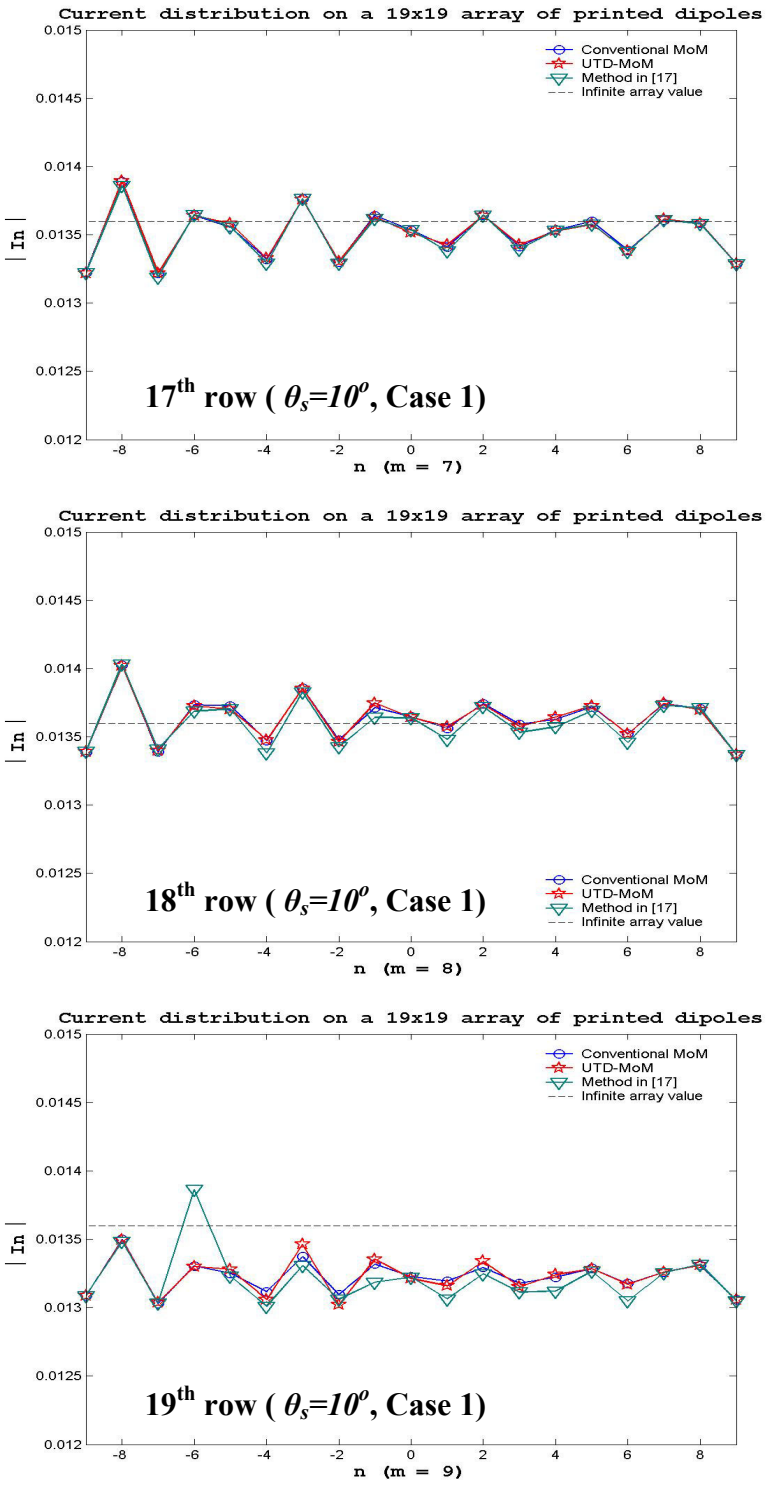

Figure 3.4 Element currents on the last three rows for Case 1 at $\theta_s = 10^o$; graph on the top: 17th row, graph in the middle: 18th row, graph at the bottom: 19th row

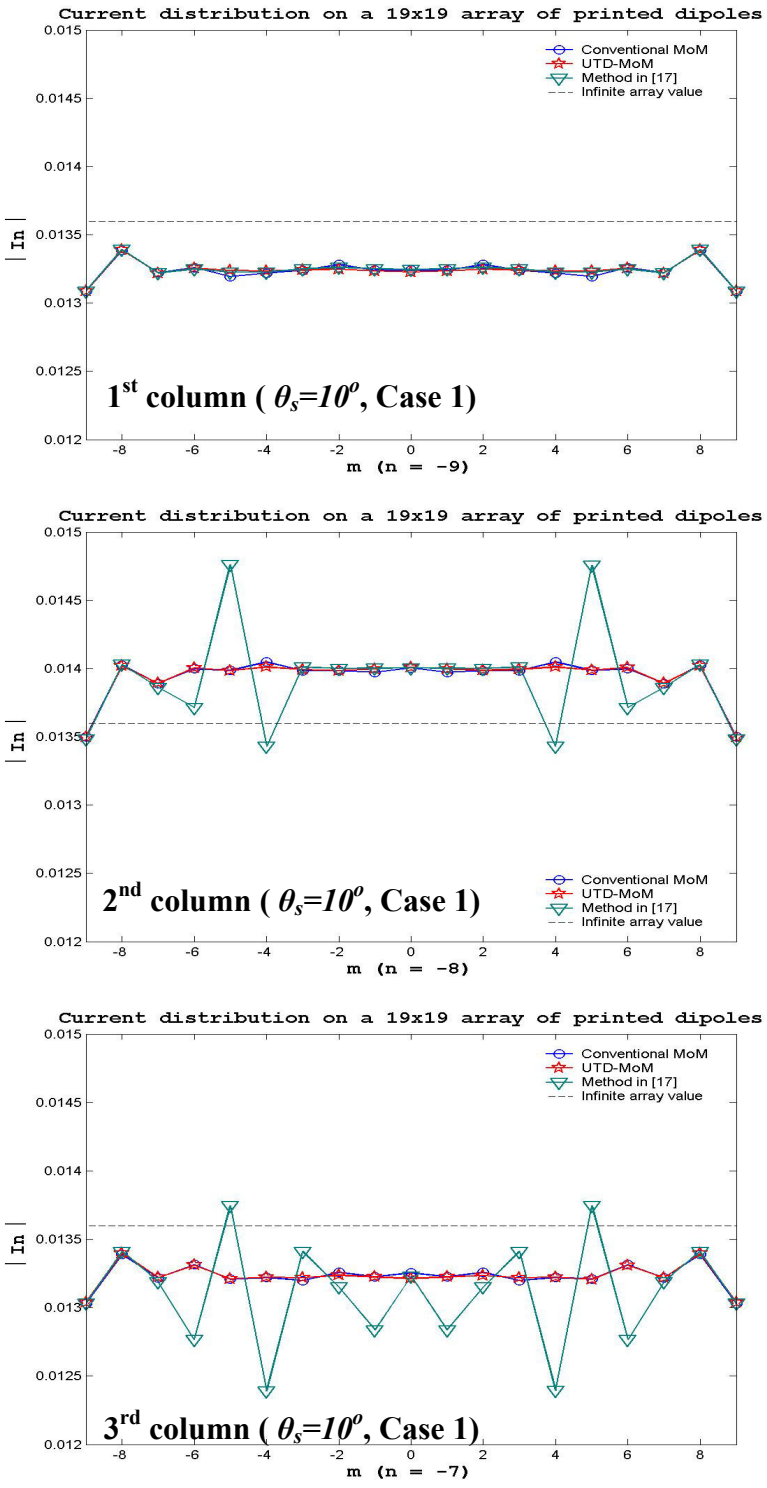

Figure 3.5 Element currents on the first three columns for Case 1 at $\theta_s = 10^o$; graph on the top is for the first column, graph in the middle is for the second column, graph at the bottom is for the third column

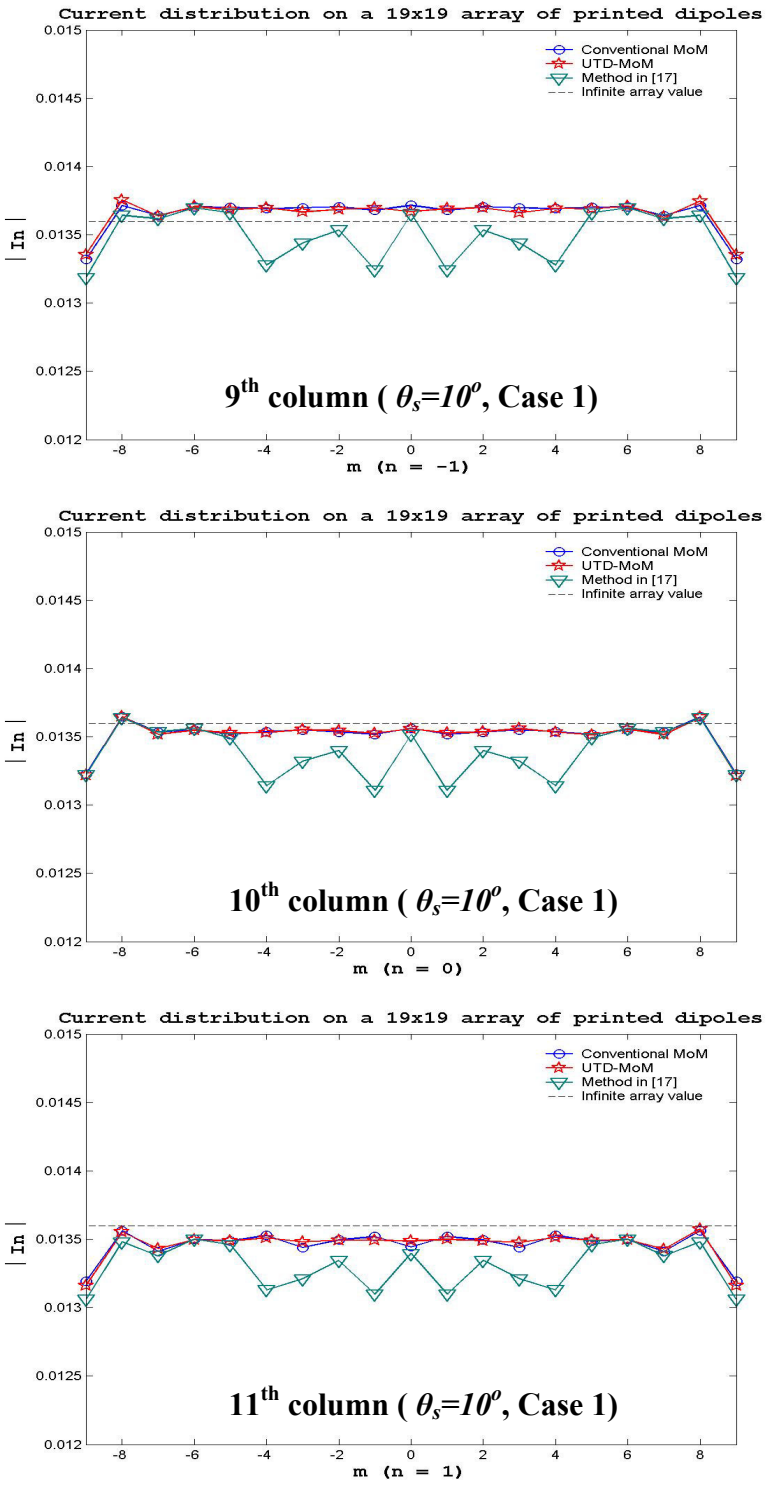

Figure 3.6 Element currents on the middle three columns for Case 1 at $\theta_s = 10^o$; graph on the top is for the 9th column, graph in the middle is for the 10th column, graph at the bottom is for the 11th column.

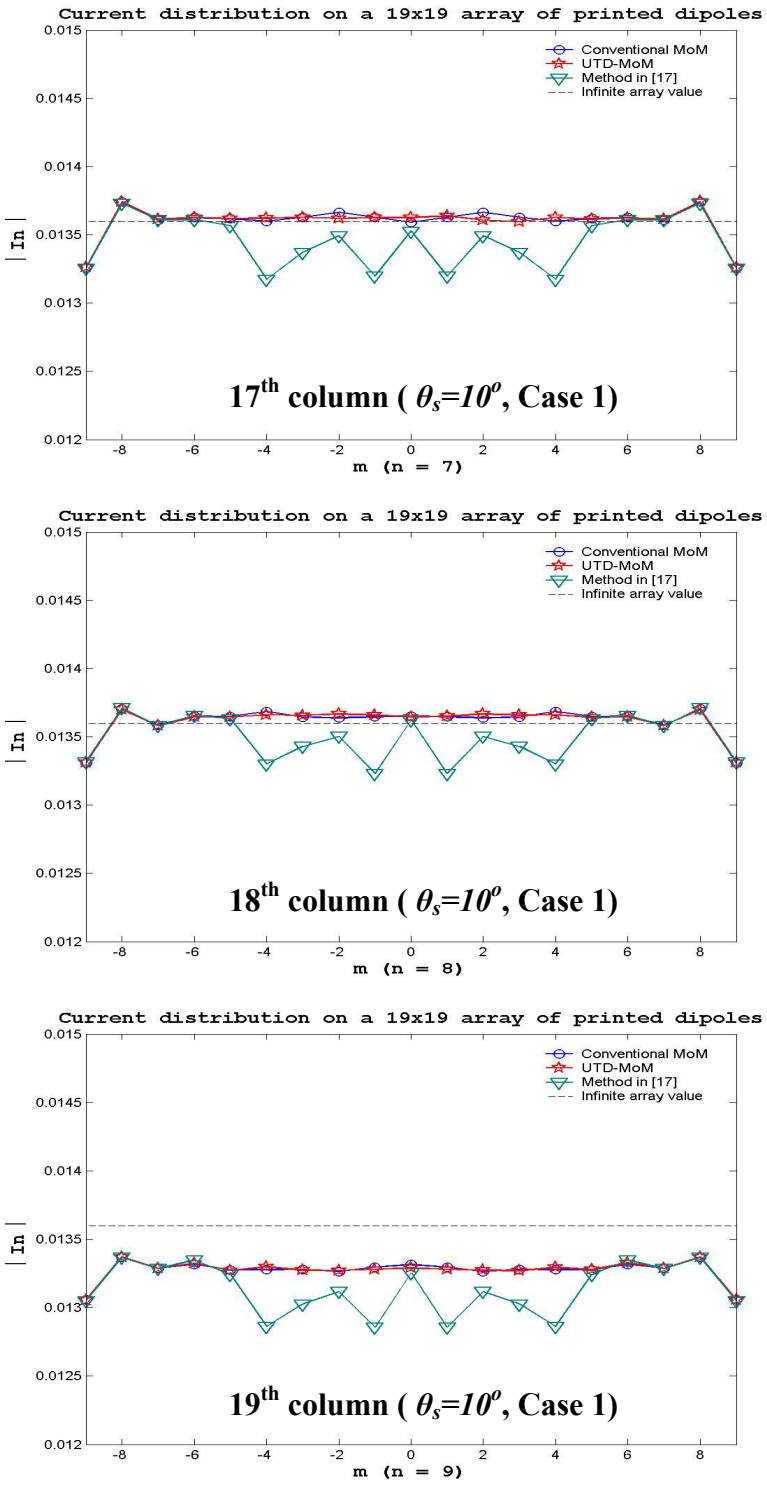

Figure 3.7 Element currents on the last three columns for Case 1 at $\theta_s = 10^o$; graph on the top is for the 17th column, graph in the middle is for the 18th column, graph at the bottom is for the 19th column.

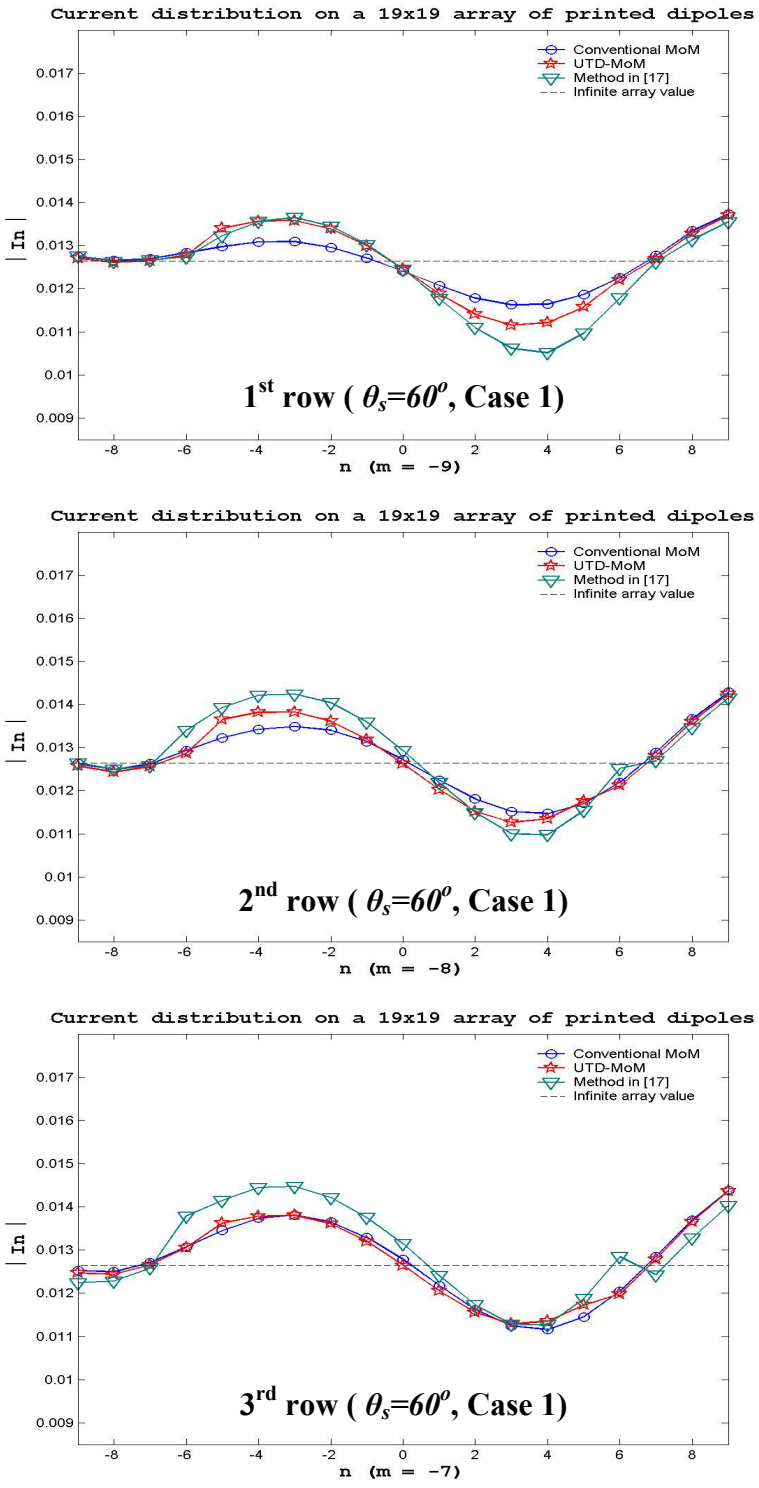

Figure 3.8 Element currents on the first three rows for Case 1 at $\theta_s = 60^o$; graph on the top is for the first row, graph in the middle is for the second row, graph at the bottom is for the third row.

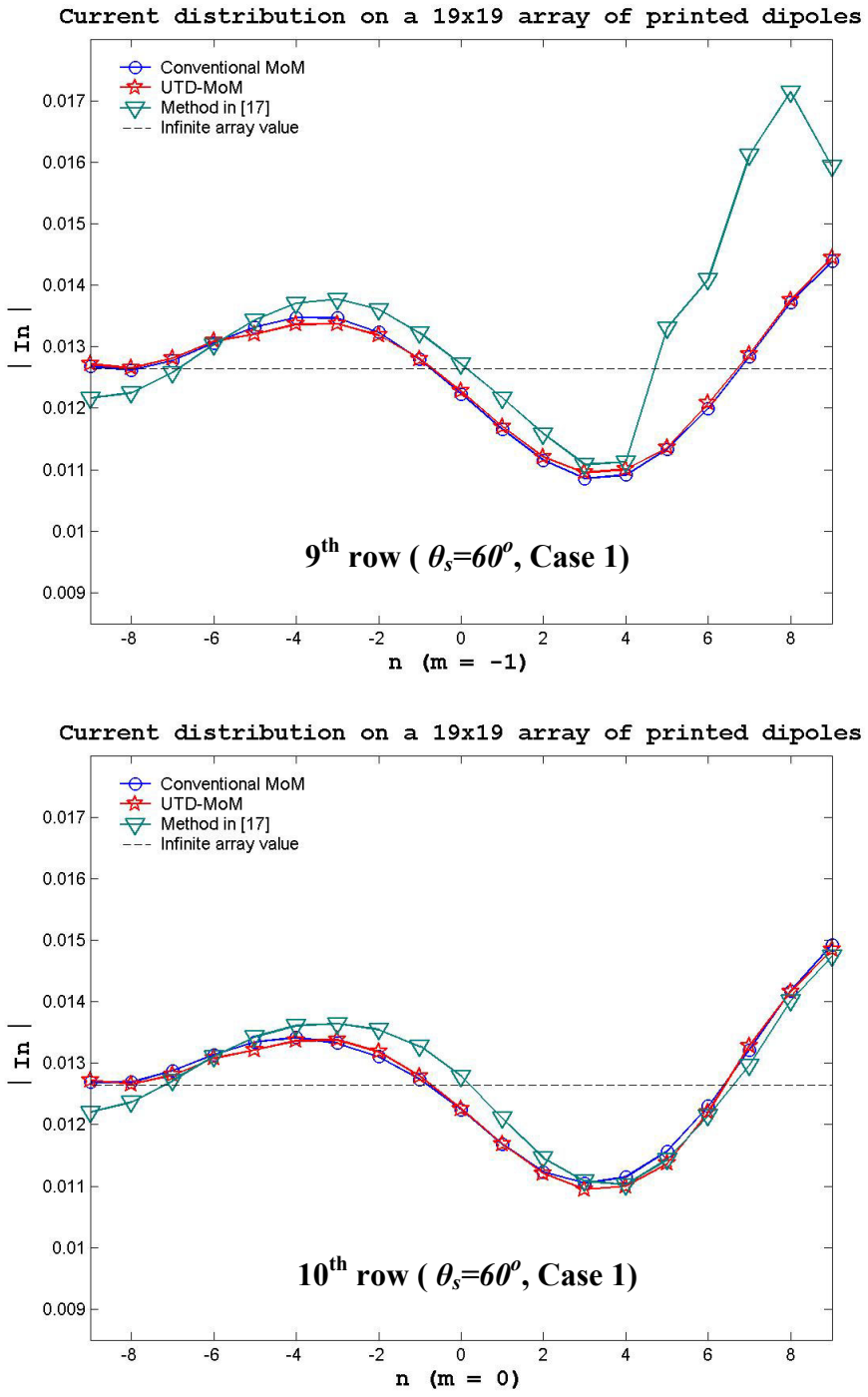

Figure 3.9 Element currents on the 9th and 10th rows in the middle for Case 1 at $\theta_s = 60^o$; graph on the top is for the 9th row, graph at the bottom is for the 10th row.

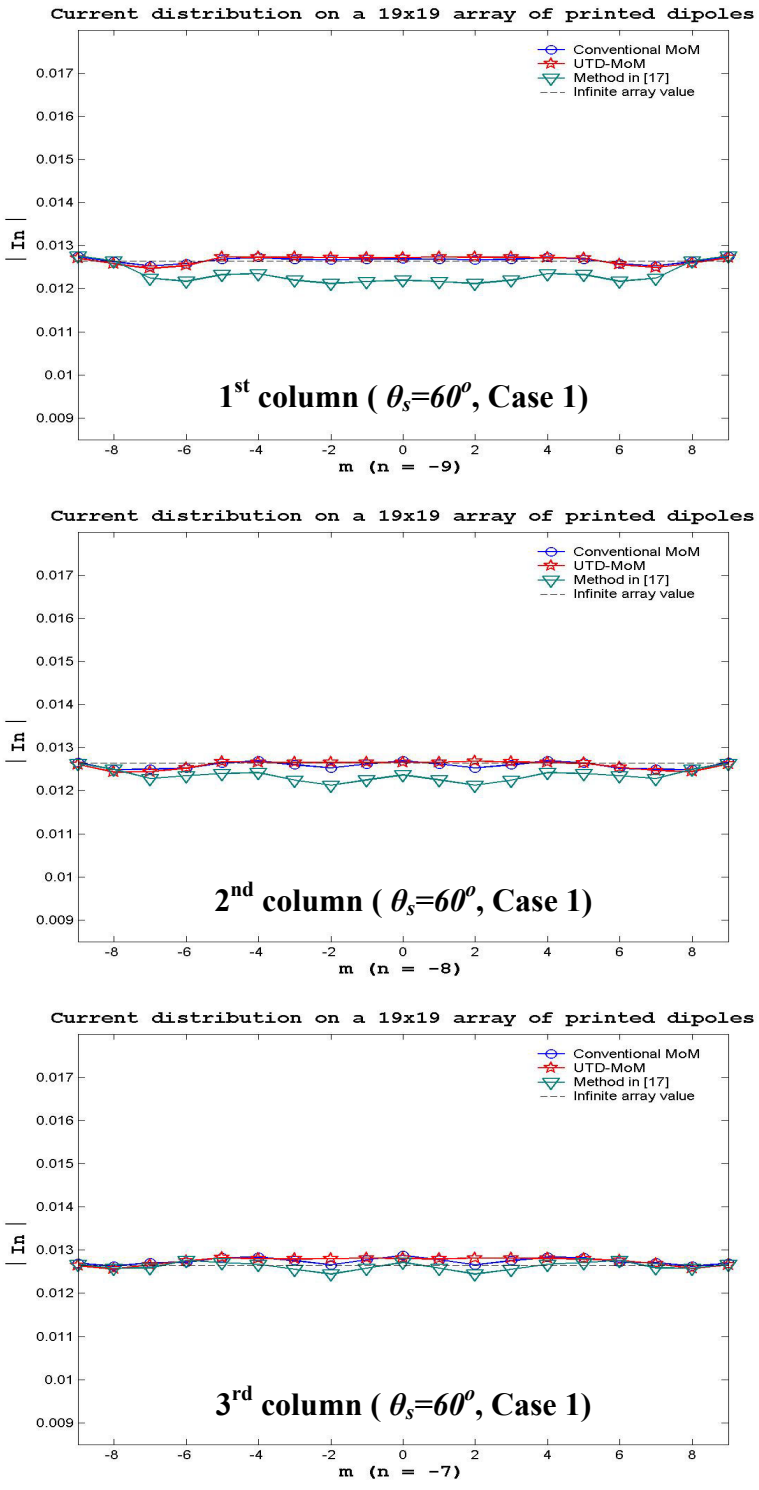

Figure 3.10 Element currents on the first three columns for Case 1 at $\theta_s = 60^o$; graph on the top is for the first column, graph in the middle is for the second column, graph at the bottom is for the third column

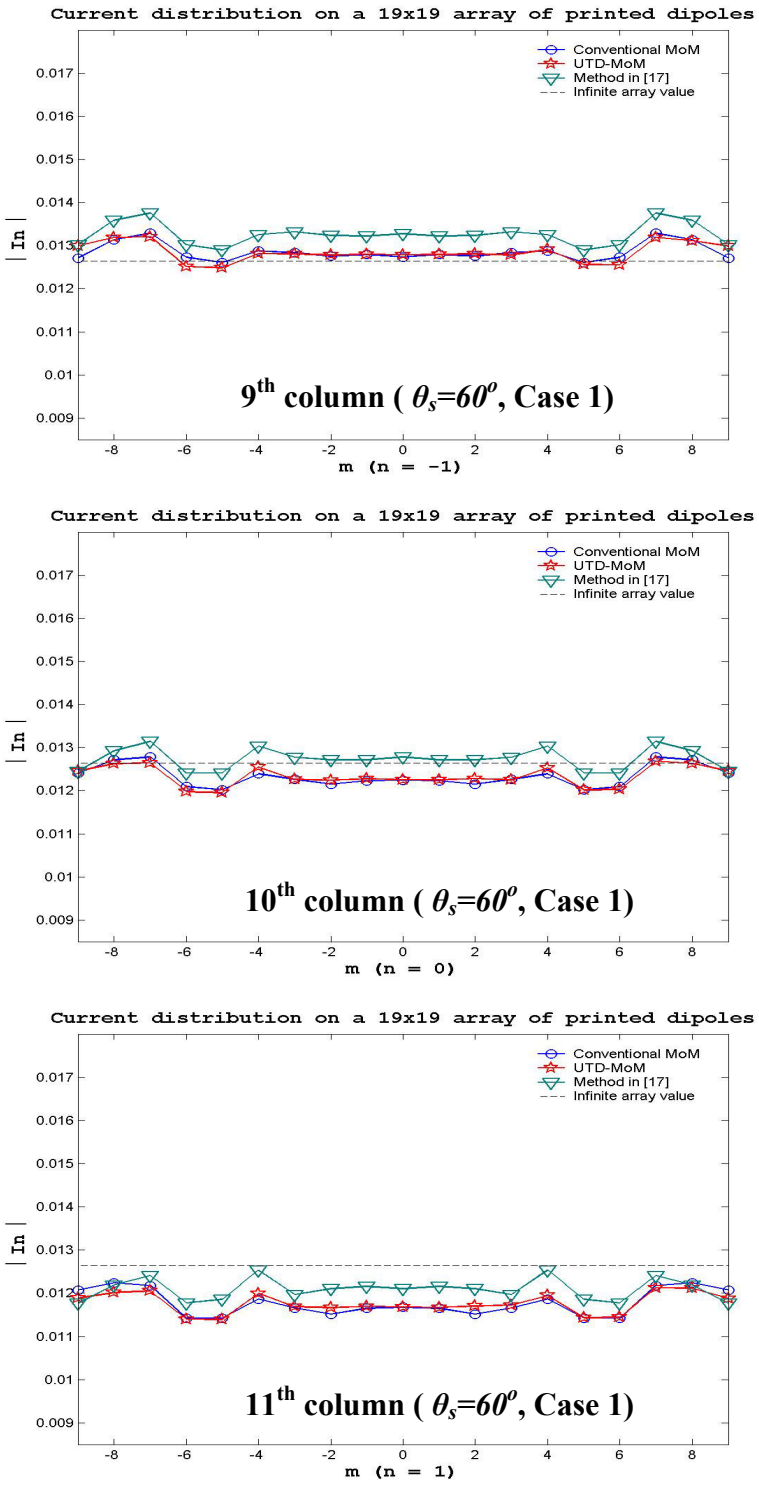

Figure 3.11 Element currents on the middle three columns for Case 1 at $\theta_s = 60^o$; graph on the top is for the 9th column, graph in the middle is for the 10th column, graph at the bottom is for the 11th column.

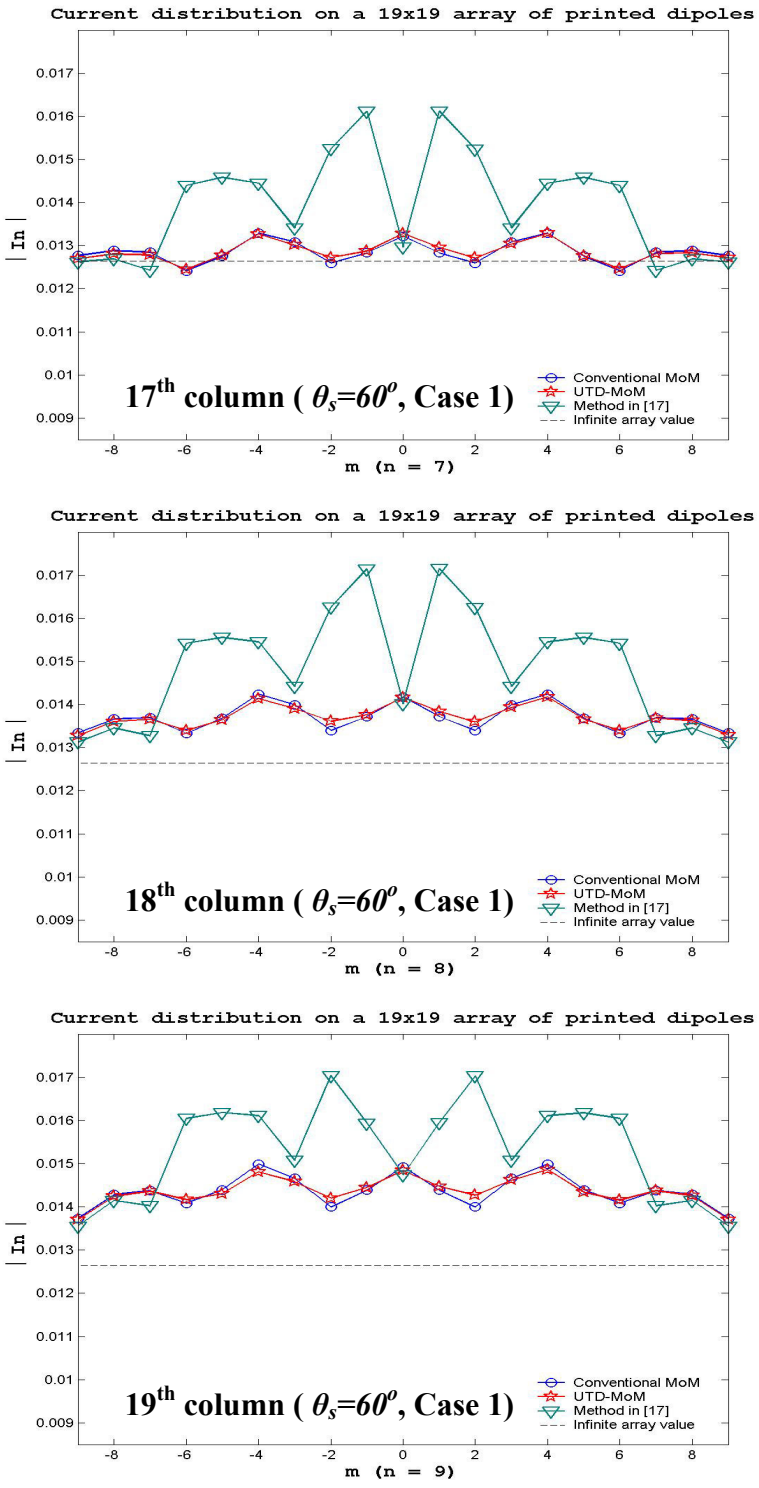

Figure 3.12 Element currents on the last three columns for Case 1 at $\theta_s = 60^o$; graph on the top is for the 17th column, graph in the middle is for the 18th column, graph at the bottom is for the 19th column.

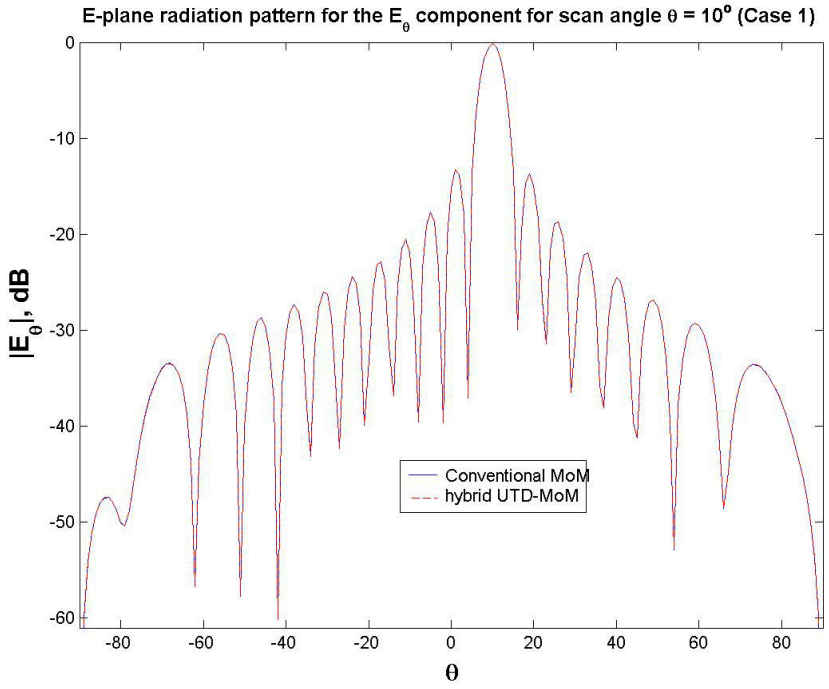

(a)

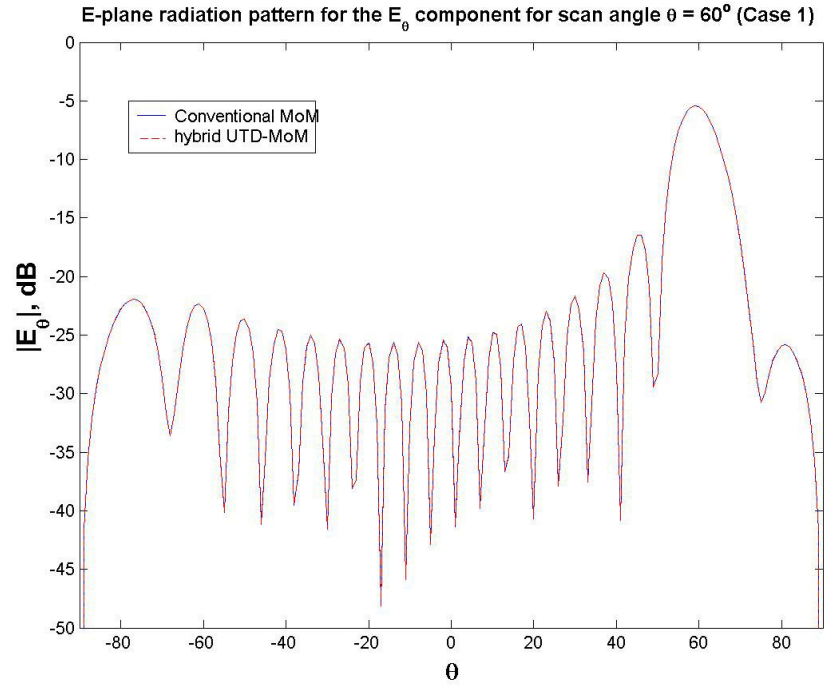

(b)

Figure 3.13 E-plane radiation patterns for the E_θ component in the case of scan angles a) $\theta_s = 10^o$ b) $\theta_s = 60^o$ (Case 1)

Case 2 The geometry and the parameters are the same as in Case 1 except for the thickness of the dielectric slab. The dielectric substrate is electrically thicker now ($d = 0.19\lambda_0$) so that the surface wave is better excited as compared to Case1.

Results are obtained for near-broadside ($\theta_s = 10^o$) and scan blindness ($\theta_s = 45.8^o$) angles and compared with three different results; i.e. conventional MoM, the method used in [17] and the infinite array solution. Although the mutual coupling effect of the surface wave is more significant now as compared to the Case 1 (due to the thicker dielectric slab), results of the present hybrid method compare very well with the results of conventional MoM method. For the arrays of printed dipoles, scan blindness is possible when the wave number β in (2.1.7) takes the value of the propagation constant, β_{sw} of the dielectric slab [27]. At blindness, nearly all the power incident on the array is trapped in the non-radiating surface wave(s), resulting in a severe degradation in the radiation in the direction of scan angle. Figures 3.19~3.24 show that the present hybrid UTD-MoM method also provides very accurate results at scan blindness angles.

The currents on the first 3 rows (1st, 2nd, and 3rd rows), on the 9th and 10th rows, and on the first 3 columns (1st, 2nd, and 3rd columns), on the 3 middle columns (9th, 10th, and 11th columns), on the last 3 columns (17th, 18th, and 19th columns) are plotted in the Figures 3.14~3.23. *E-plane* radiation patterns for the E_θ component in the case of scan angles $\theta_s = 10^o$ and $\theta_s = 45.8^o$ are shown in the Figure 3.24.

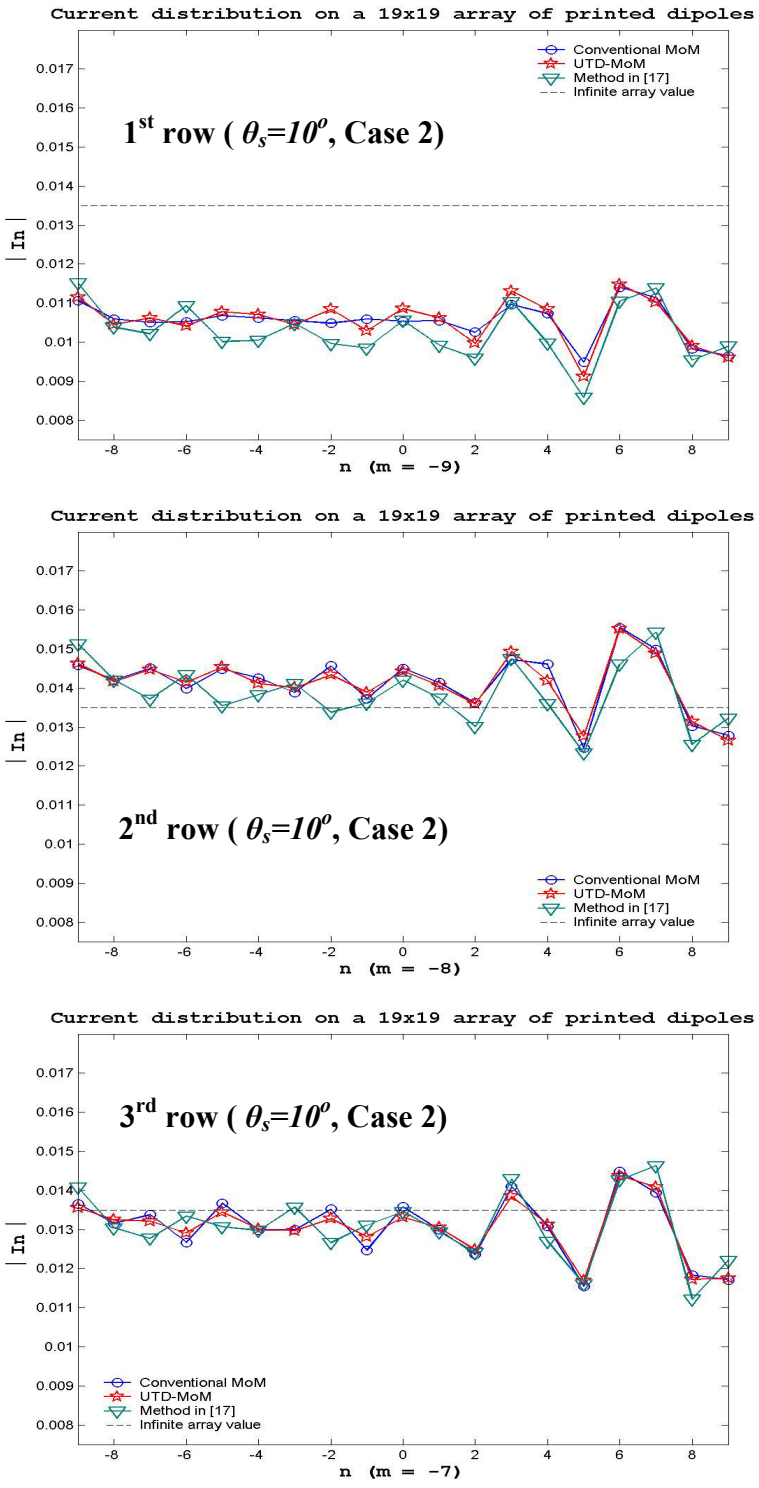

Figure 3.14 Element currents on the first three rows for Case 2 at $\theta_s = 10^o$; graph on the top is for the first row, graph in the middle is for the second row, graph at the bottom is for the third row.

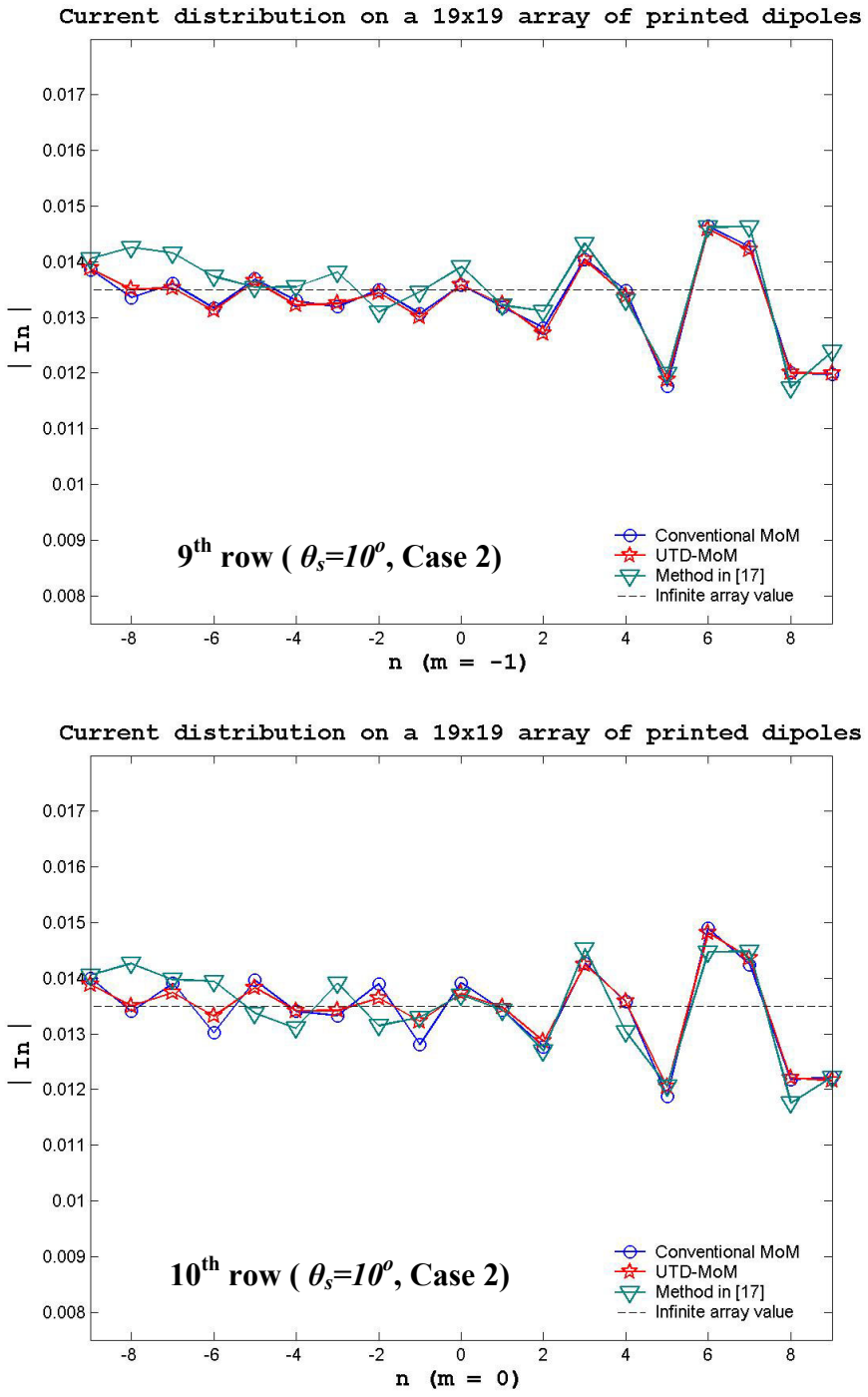

Figure 3.15 Element currents on the 9th and 10th rows in the middle for Case 2 at $\theta_s = 10^o$; graph on the top is for the 9th row, graph at the bottom is for the 10th row.

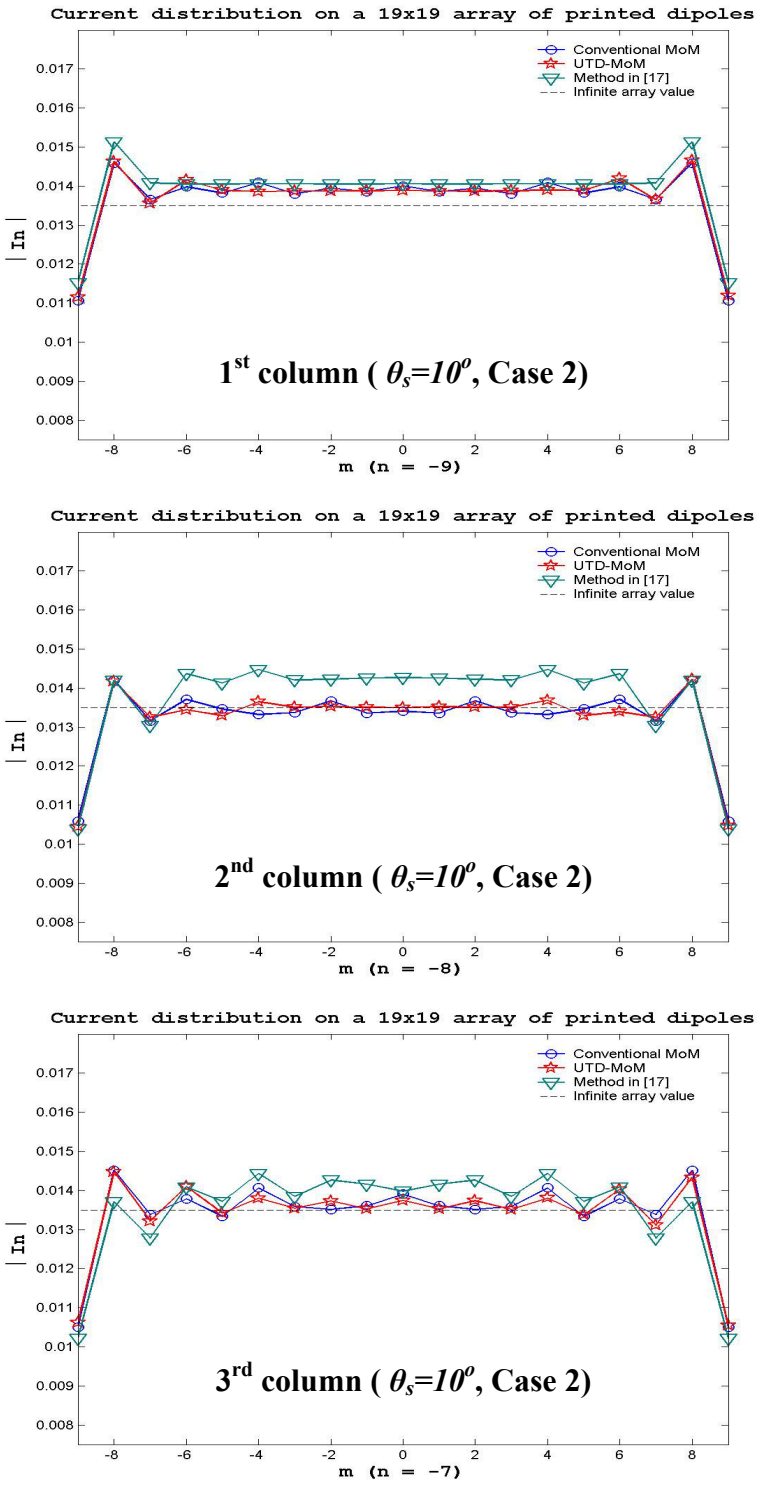

Figure 3.16 Element currents on the first three columns for Case 2 at $\theta_s = 10^o$; graph on the top is for the first column, graph in the middle is for the second column, graph at the bottom is for the third column

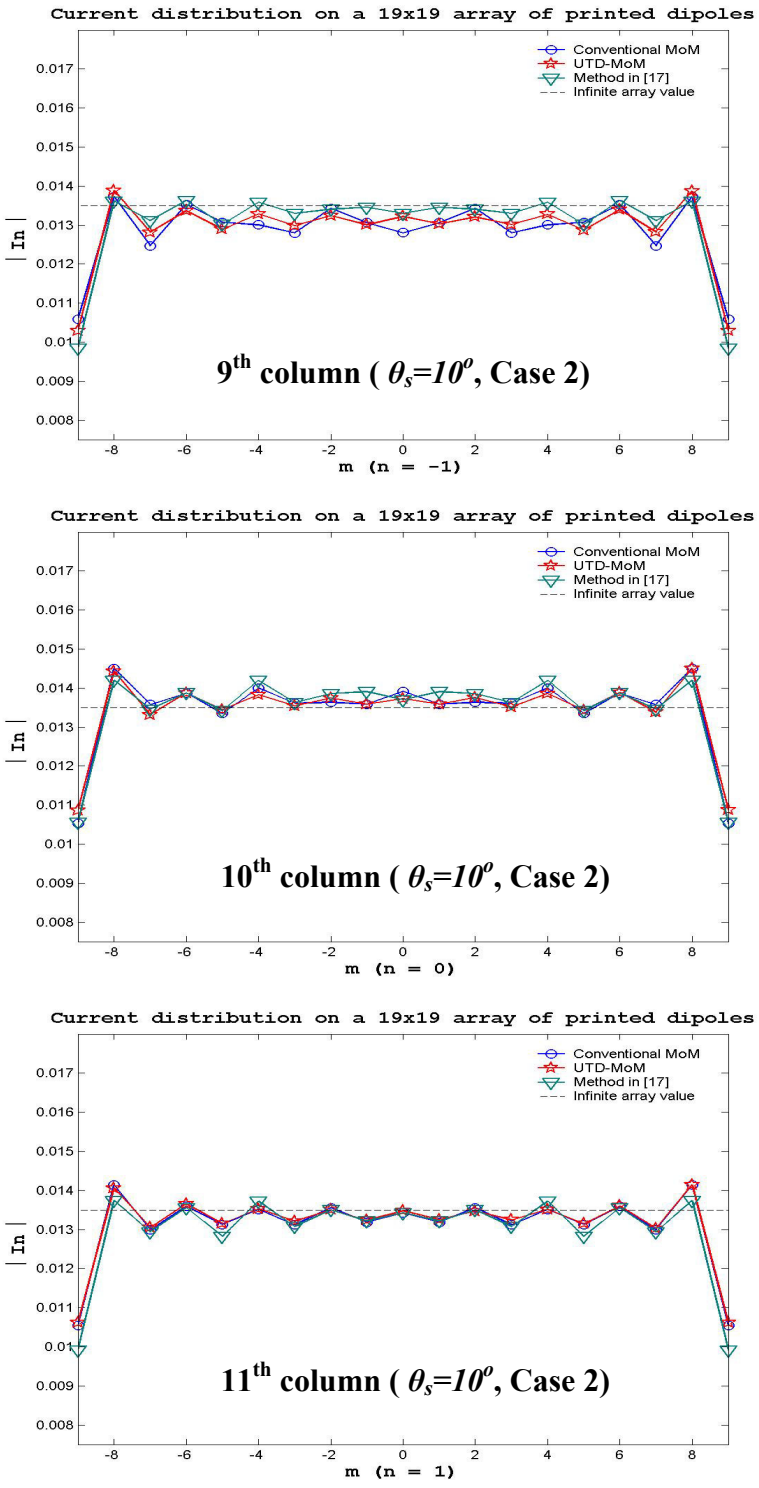

Figure 3.17 Element currents on the middle three columns for Case 2 at $\theta_s = 10^o$; graph on the top is for the 9th column, graph in the middle is for the 10th column, graph at the bottom is for the 11th column.

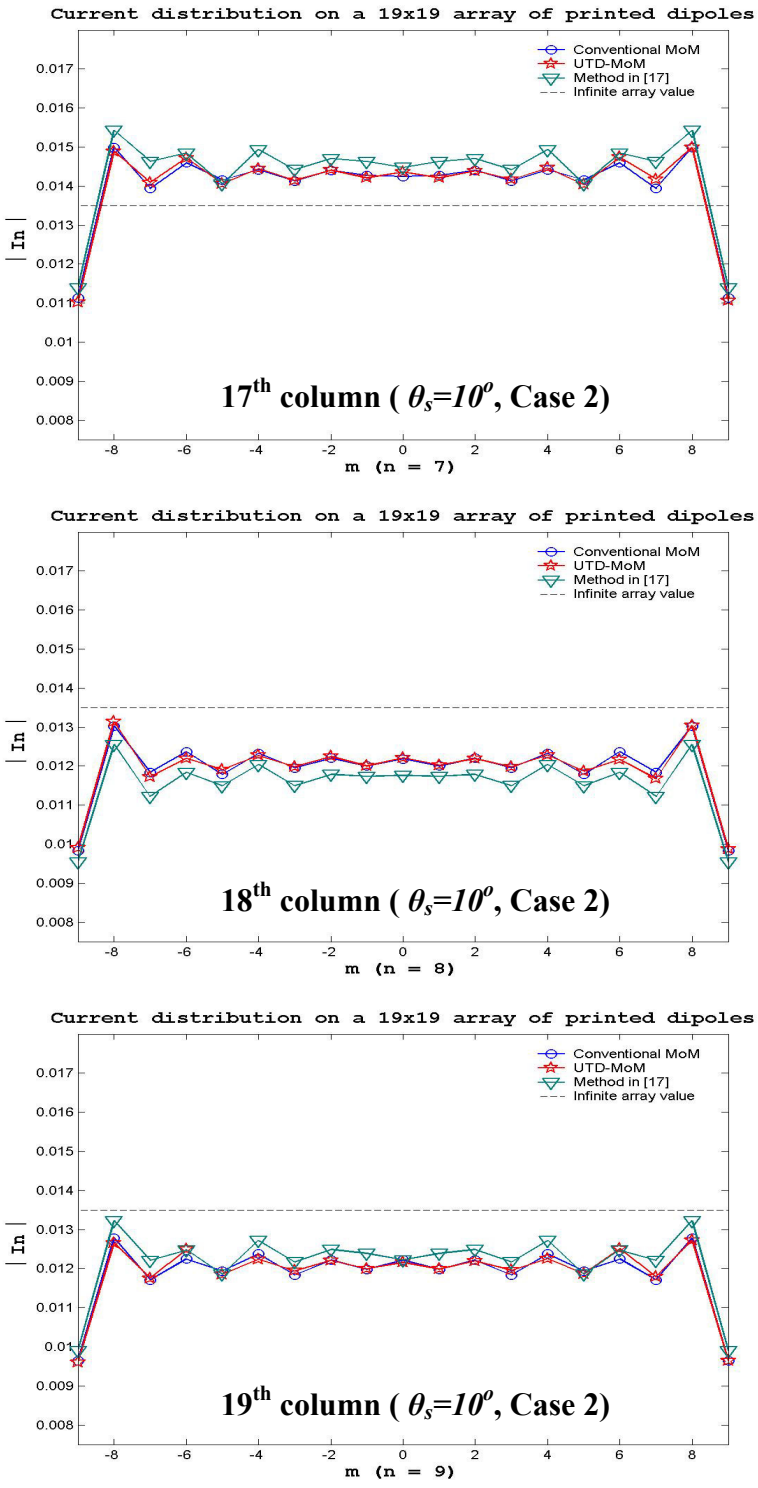

Figure 3.18 Element currents on the last three columns for Case 2 at $\theta_s = 10^o$; graph on the top is for the 17th column, graph in the middle is for the 18th column, graph at the bottom is for the 19th column.

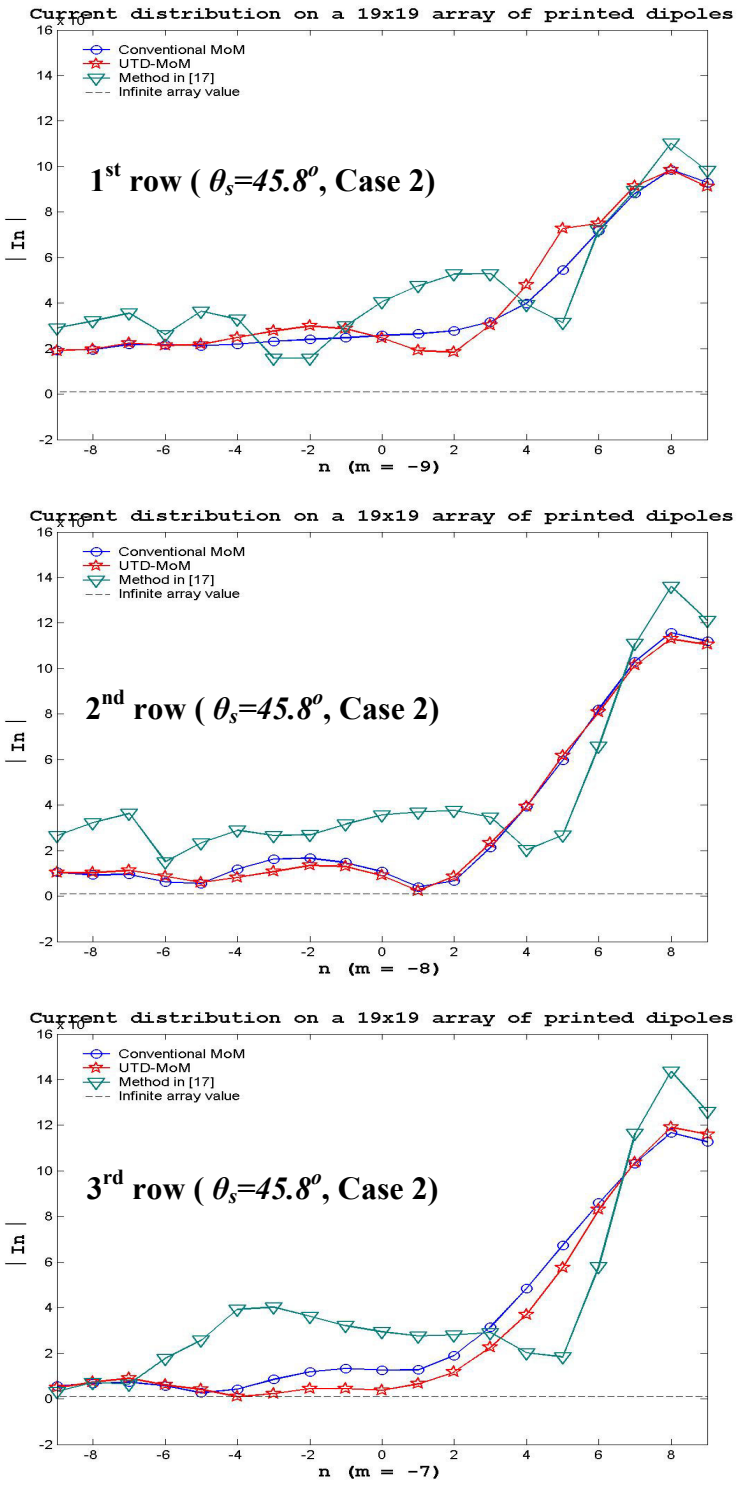

Figure 3.19 Element currents on the first three rows for Case 2 at $\theta_s = 45.8^o$; graph on the top is for the first row, graph in the middle is for the second row, graph at the bottom is for the third row

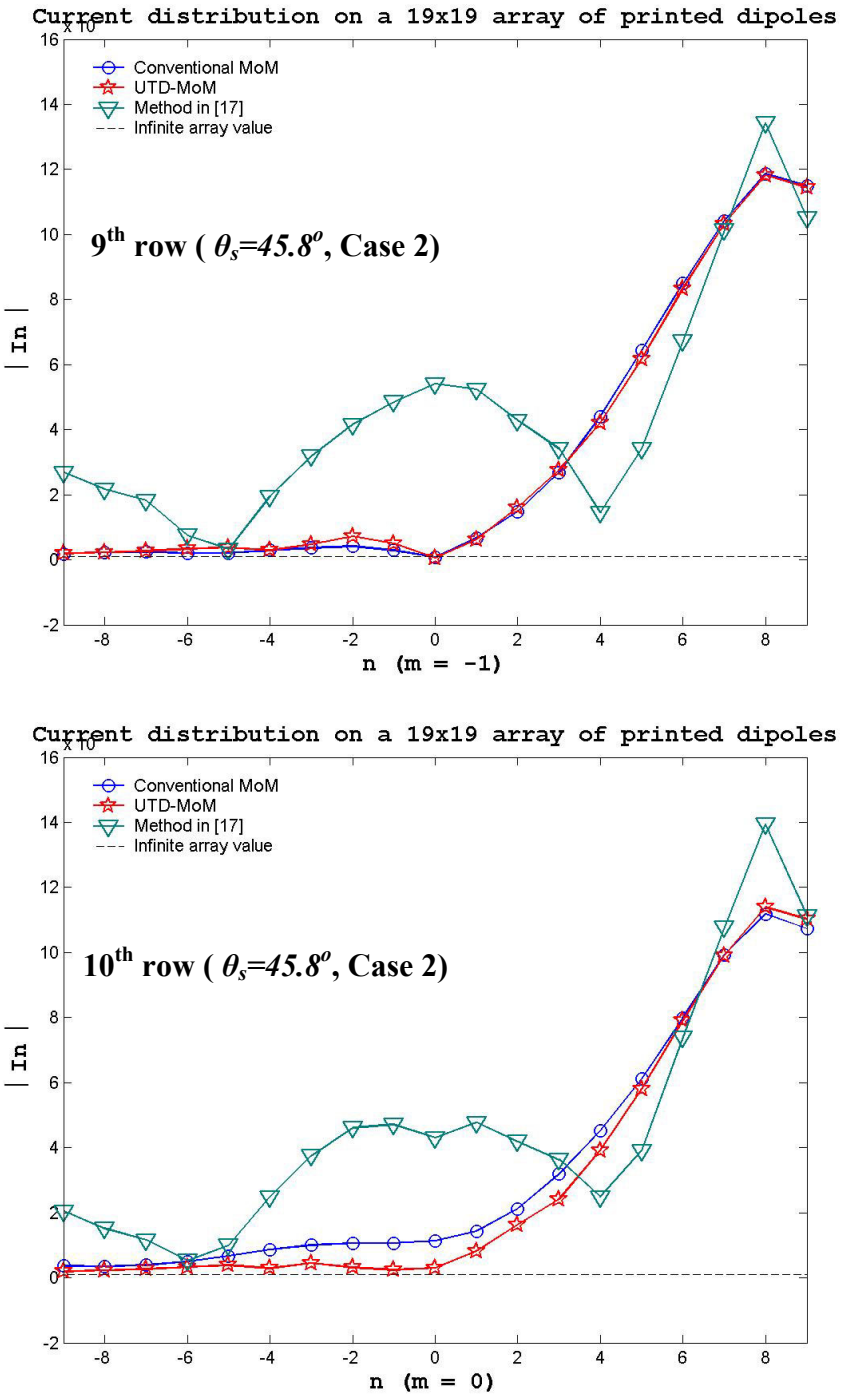

Figure 3.20 Element currents on the 9th and 10th rows in the middle for Case 2 at $\theta_s = 45.8^o$; graph on the top is for the 9th row, graph at the bottom is for the 10th row.

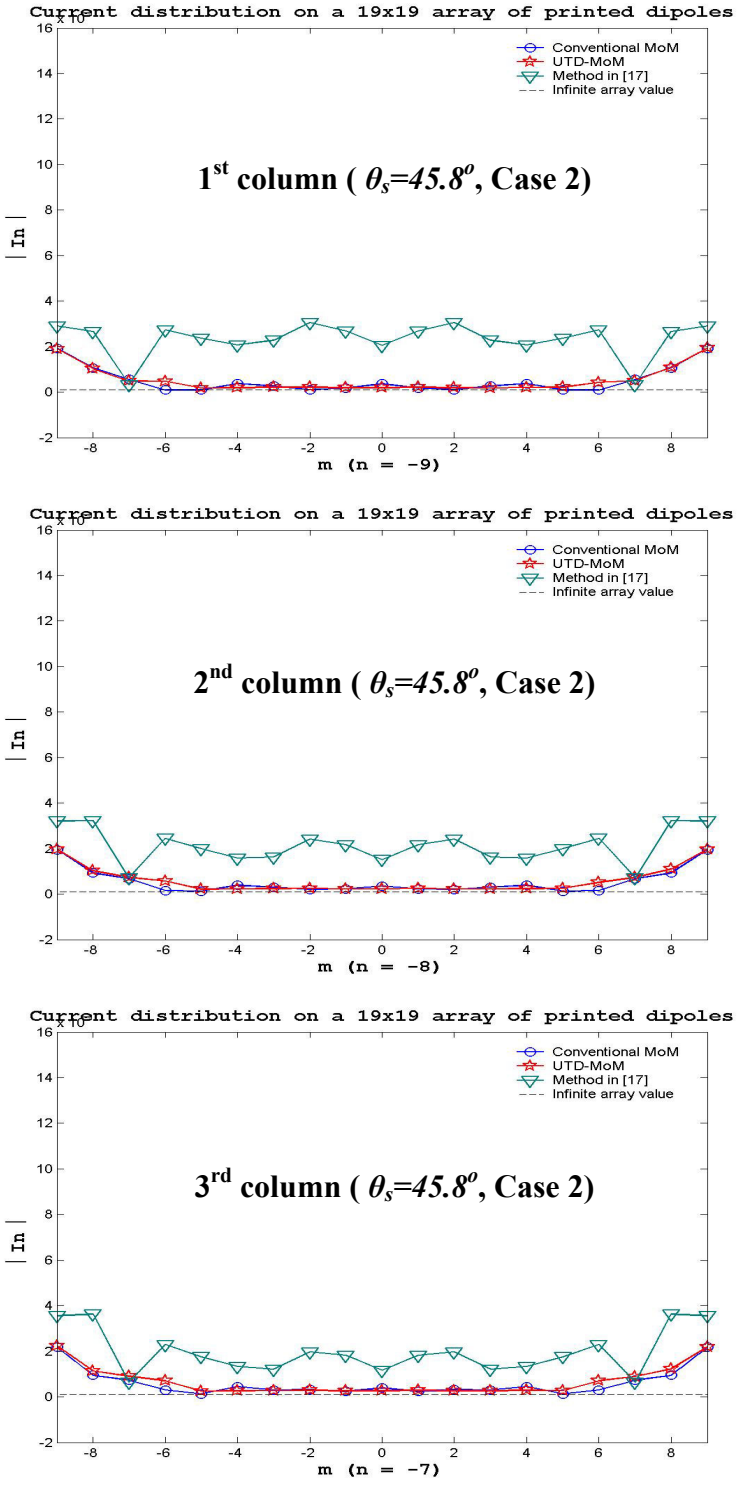

Figure 3.21 Element currents on the first three columns for Case 2 at $\theta_s = 45.8^o$; graph on the top is for the first column, graph in the middle is for the second column, graph at the bottom is for the third column

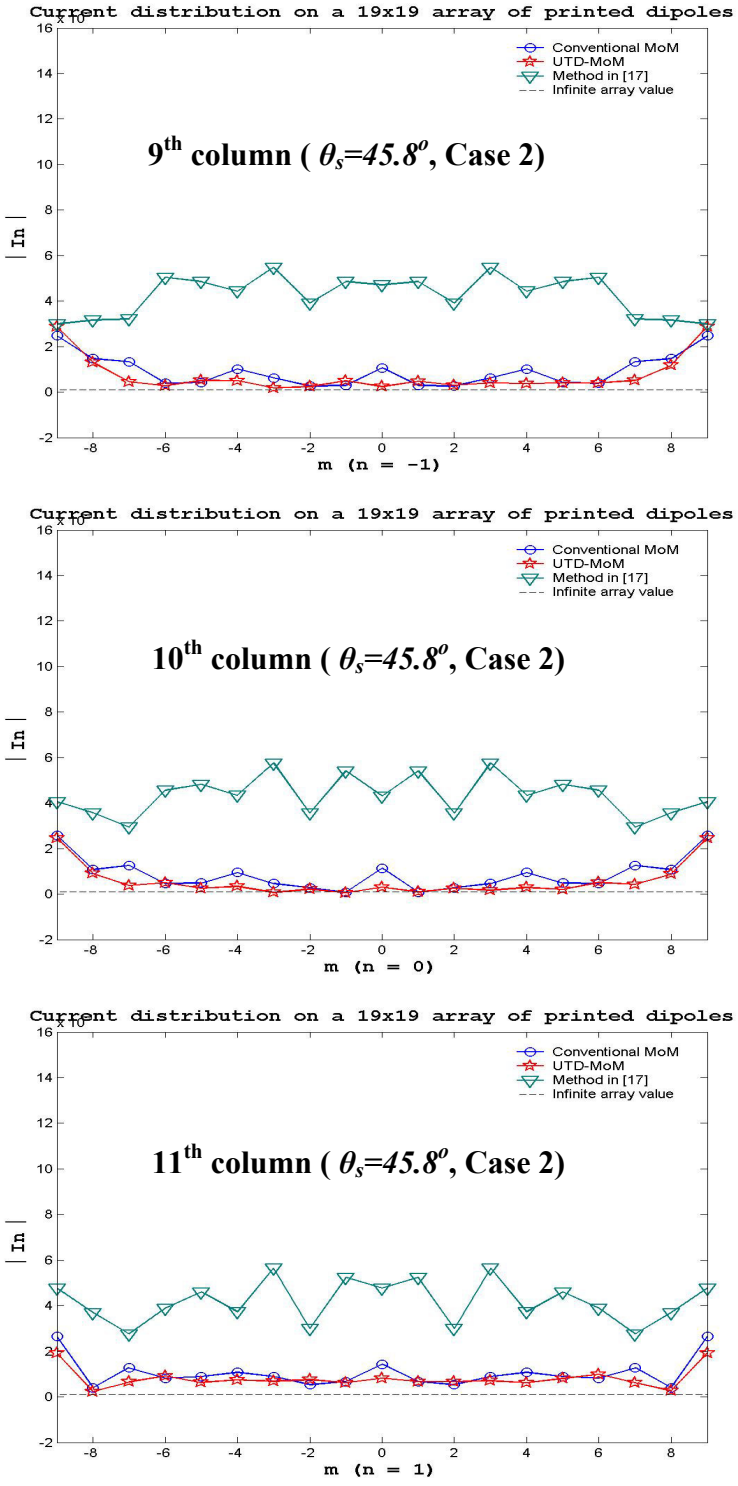

Figure 3.22 Element currents on the middle three columns for Case 2 at $\theta_s = 45.8^o$; graph on the top is for the 9th column, graph in the middle is for the 10th column, graph at the bottom is for the 11th column.

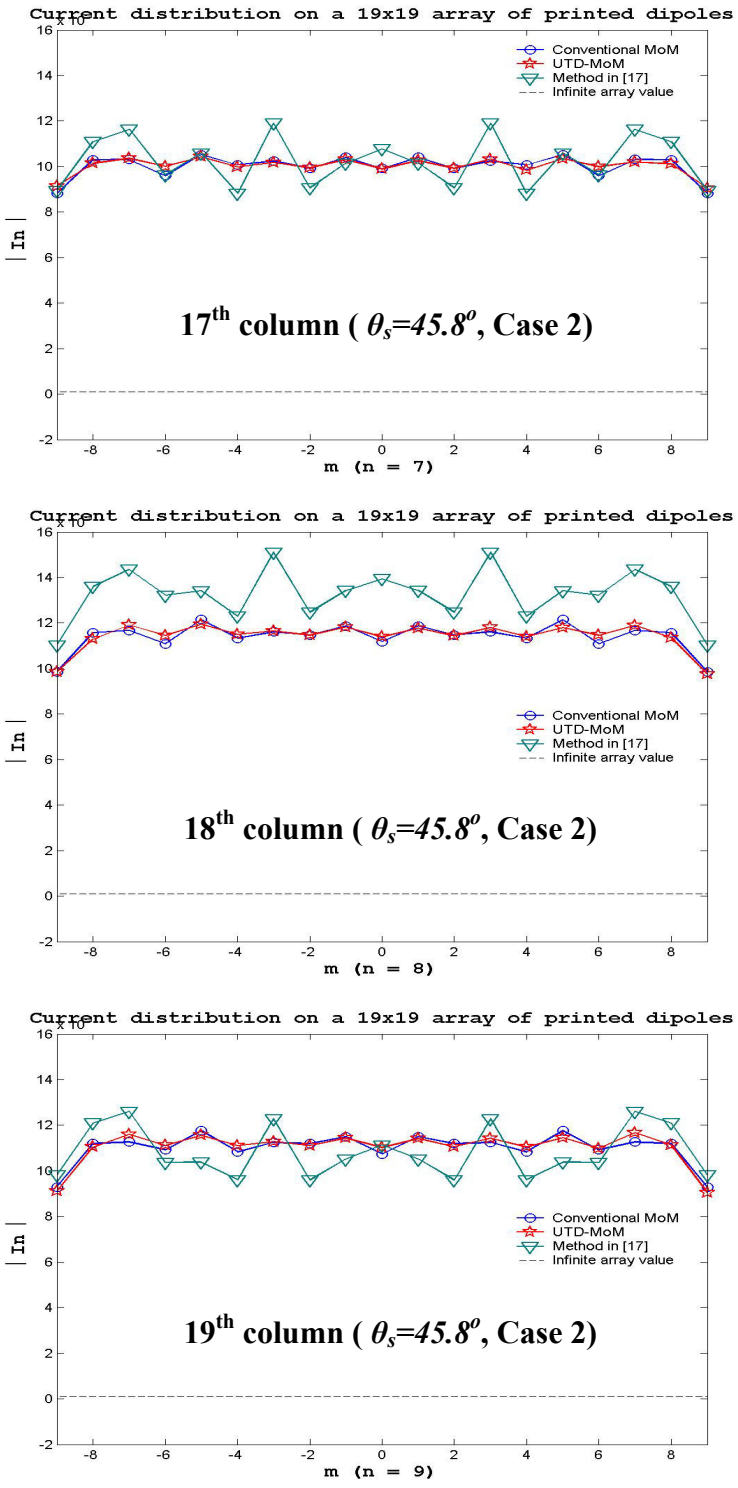

Figure 3.23 Element currents on the last three columns for Case 2 at $\theta_s = 45.8^o$; graph on the top is for the 17th column, graph in the middle is for the 18th column, graph at the bottom is for the 19th column

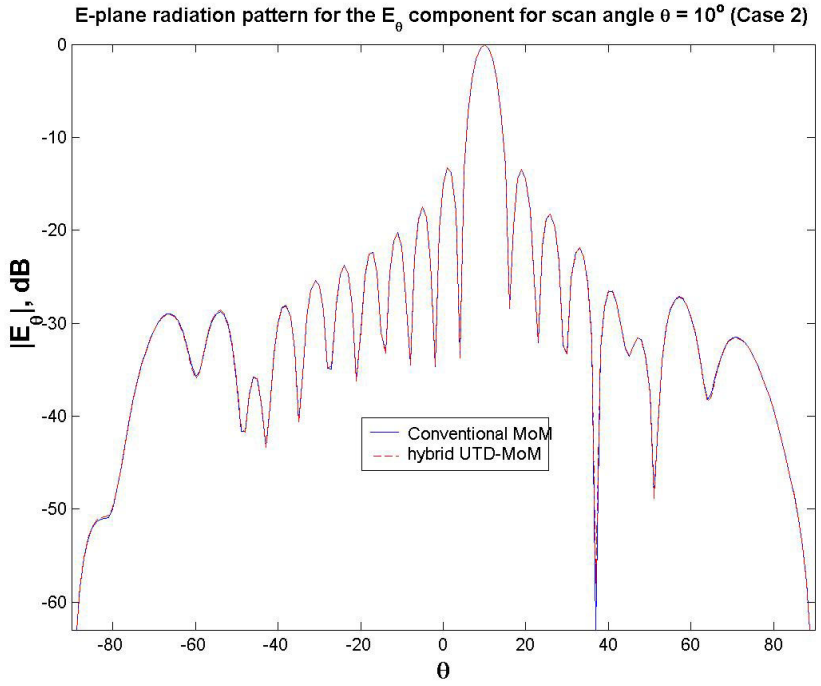

(a)

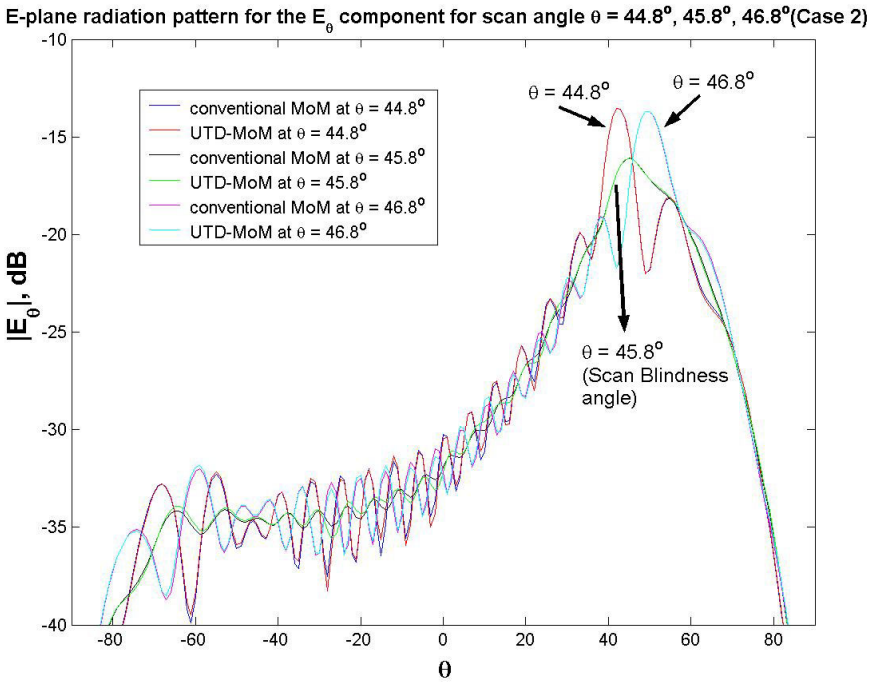

(b)

Figure 3.24 E-plane radiation patterns for the E_θ component in the case of scan angles a) $\theta_s = 10^o$ b) $\theta_s = 44.8^o$, $\theta_s = 45.8^o$ (scan blindness), $\theta_s = 46.8^o$ (Case 2)

Case 3 In this case the dielectric substrate is electrically thin ($d = 0.06\lambda_0$) but of high relative permittivity so that the surface wave is better excited.

Results are obtained for near-broadside ($\theta_s = 10^o$) and off-broadside ($\theta_s = 55^o$) radiations and compared with three different results; i.e. conventional MoM, the method used in [17] and the infinite array solution. Although the mutual coupling effect of the surface wave is more significant now as compared to the Case 1 (due to the higher relative permittivity of the dielectric slab), results of the present hybrid method compare very well with the results of conventional MoM method for both the near-broadside ($\theta_s = 10^o$) and off-broadside ($\theta_s = 55^o$) radiations.

The currents on the first 3 rows (1st, 2nd, and 3rd rows), on the 9th and 10th rows, and on the first 3 columns (1st, 2nd, and 3rd columns), on the 3 middle columns (9th, 10th, and 11th columns), on the last 3 columns (17th, 18th, and 19th columns) are plotted in the Figures 3.25~3.34. E-plane radiation patterns for the E_θ component in the case of scan angles $\theta_s = 10^o$ and $\theta_s = 55^o$ are shown in the Figure 3.35.

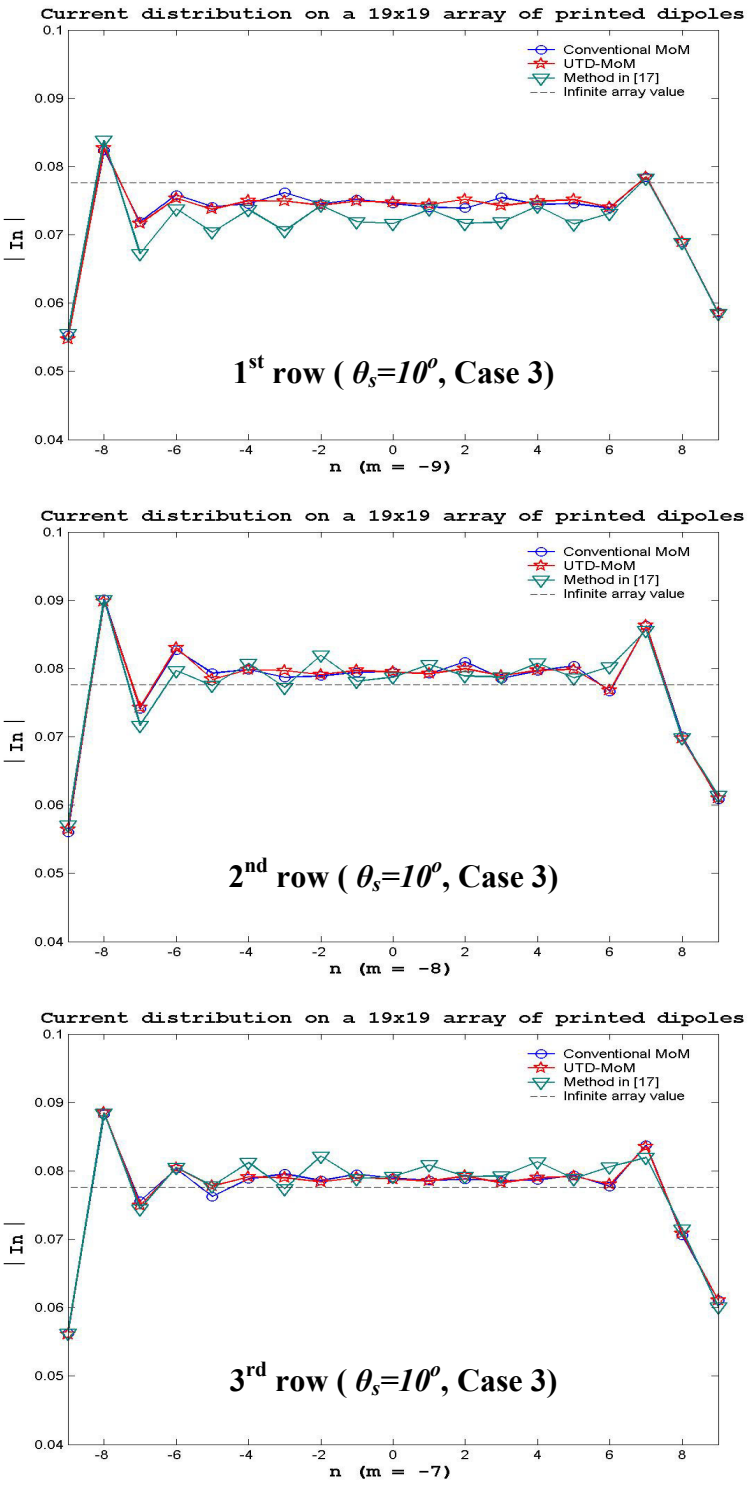

Figure 3.25 Element currents on the first three rows for Case 3 at $\theta_s = 10^o$; graph on the top is for the first row, graph in the middle is for the second row, graph at the bottom is for the third row

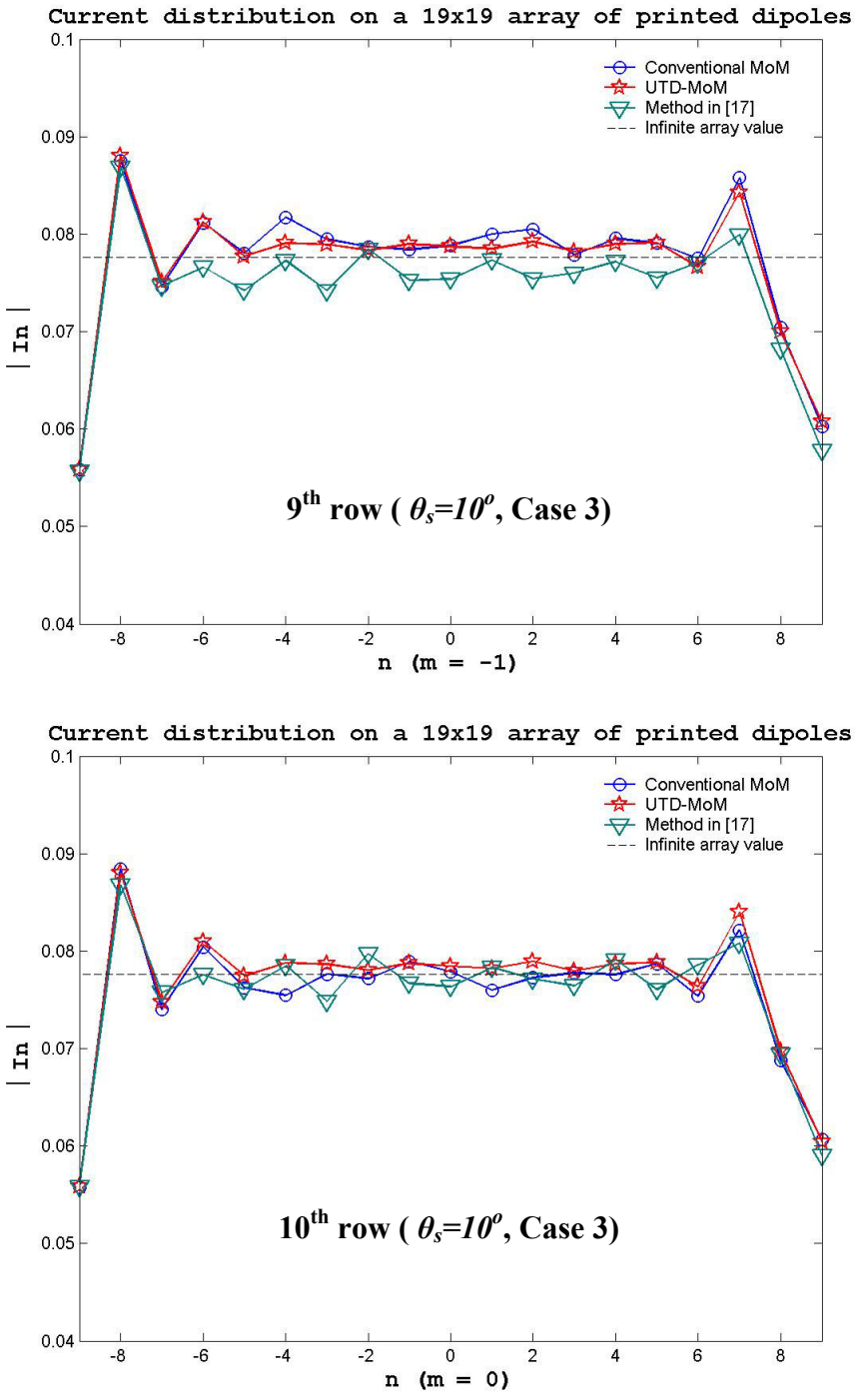

Figure 3.26 Element currents on the 9th and 10th rows in the middle for Case 3 at $\theta_s = 10^o$; graph on the top is for the 9th row, graph at the bottom is for the 10th row.

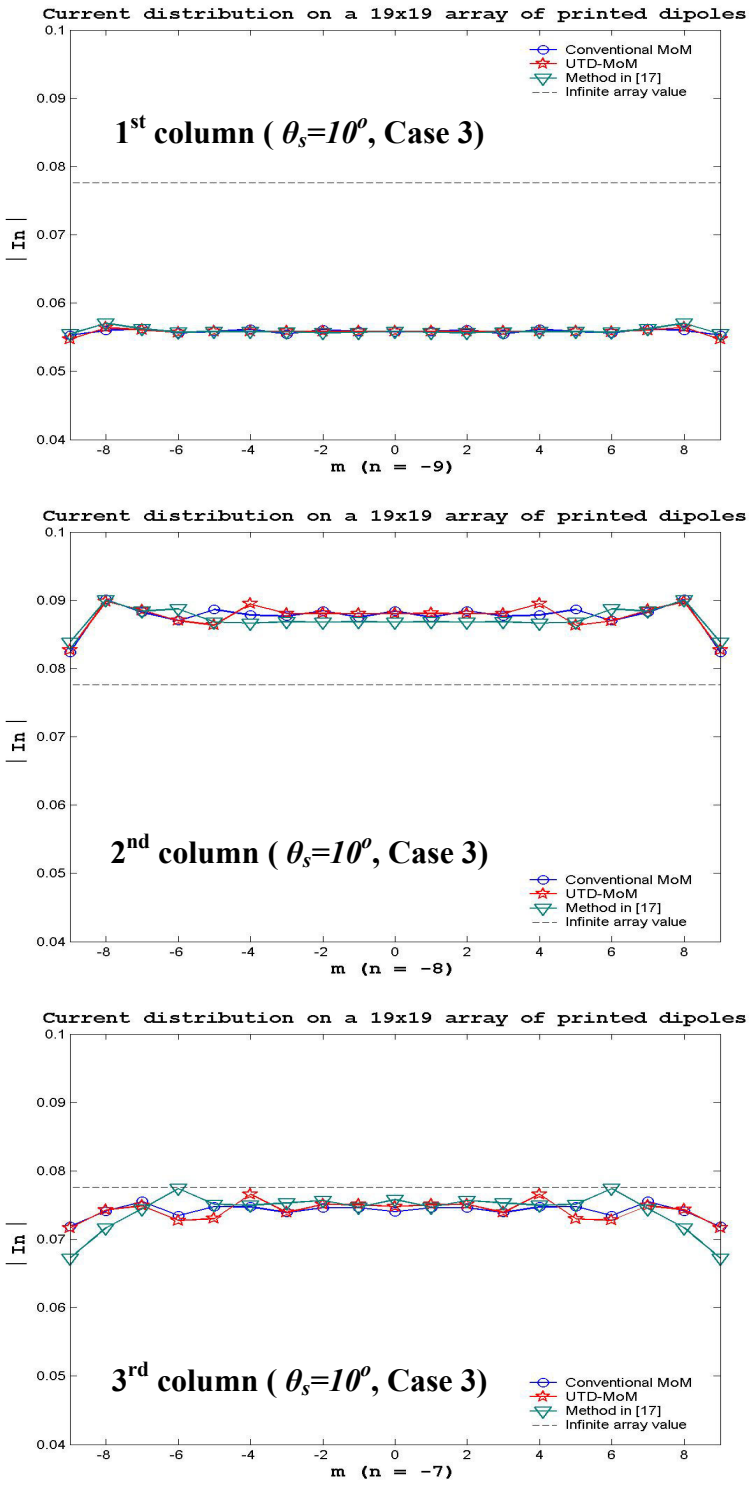

Figure 3.27 Element currents on the first three columns for Case 3 at $\theta_s = 10^o$; graph on the top is for the first column, graph in the middle is for the second column, graph at the bottom is for the third column.

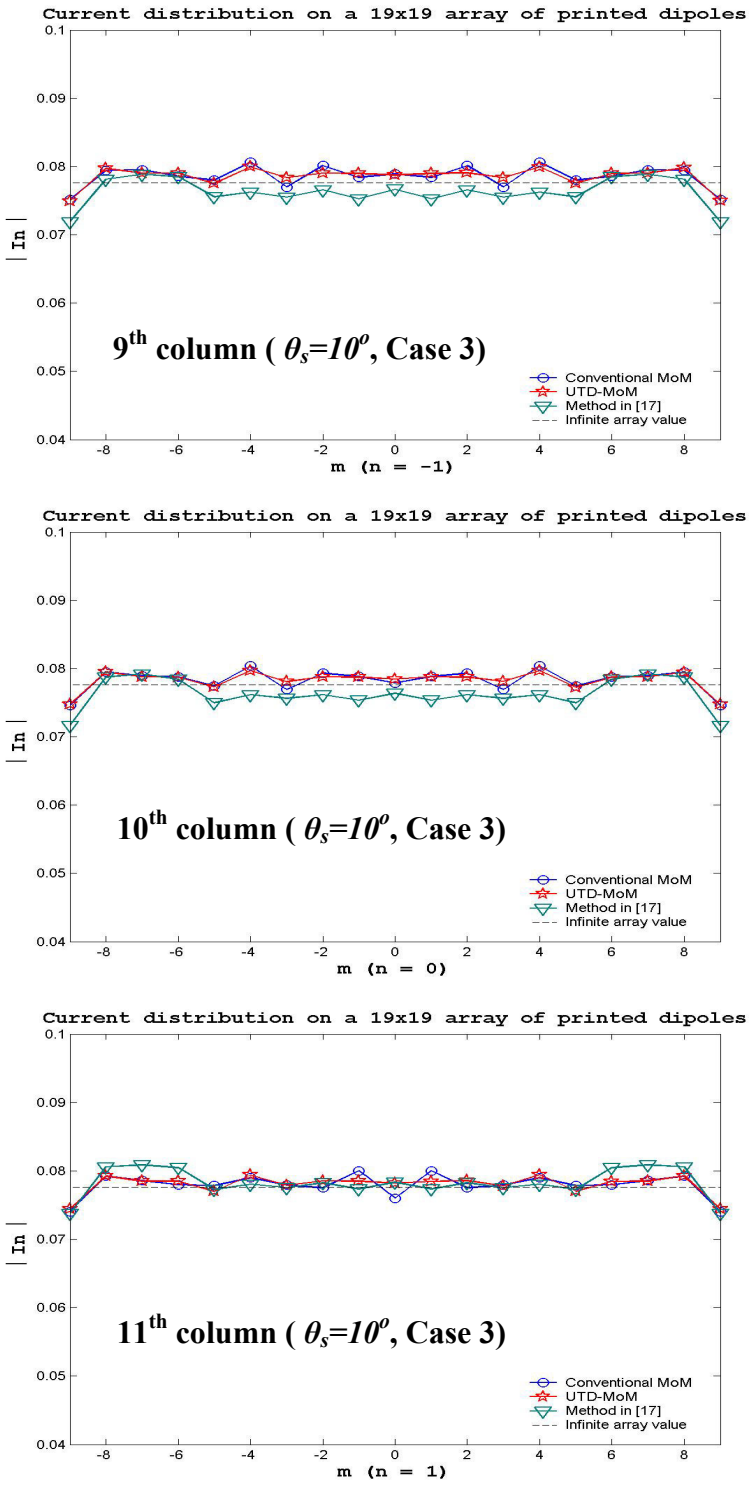

Figure 3.28 Element currents on the middle three columns for Case 3 at $\theta_s = 10^o$; graph on the top is for the 9th column, graph in the middle is for the 10th column, graph at the bottom is for the 11th column.

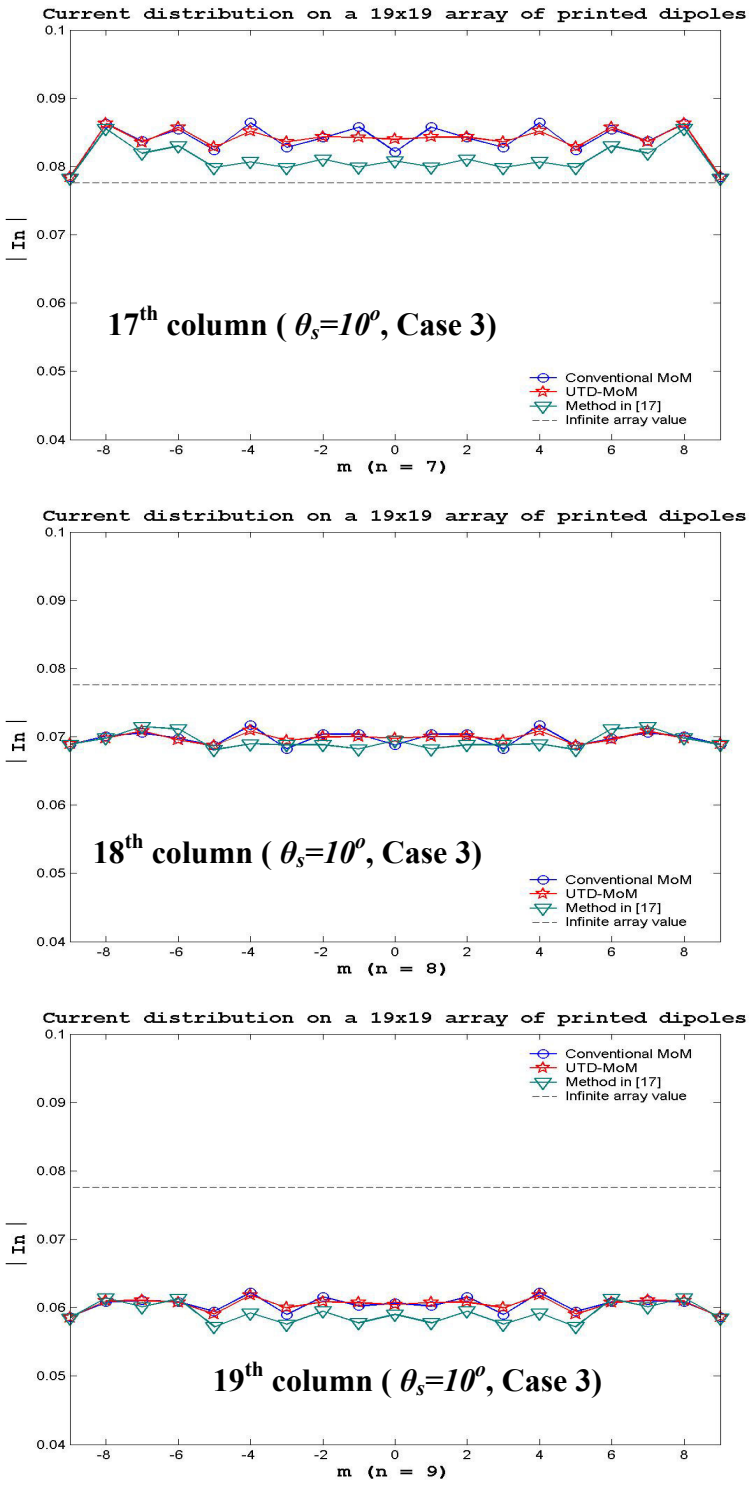

Figure 3.29 Element currents on the last three columns for Case 3 at $\theta_s = 10^o$; graph on the top is for the 17th column, graph in the middle is for the 18th column, graph at the bottom is for the 19th column.

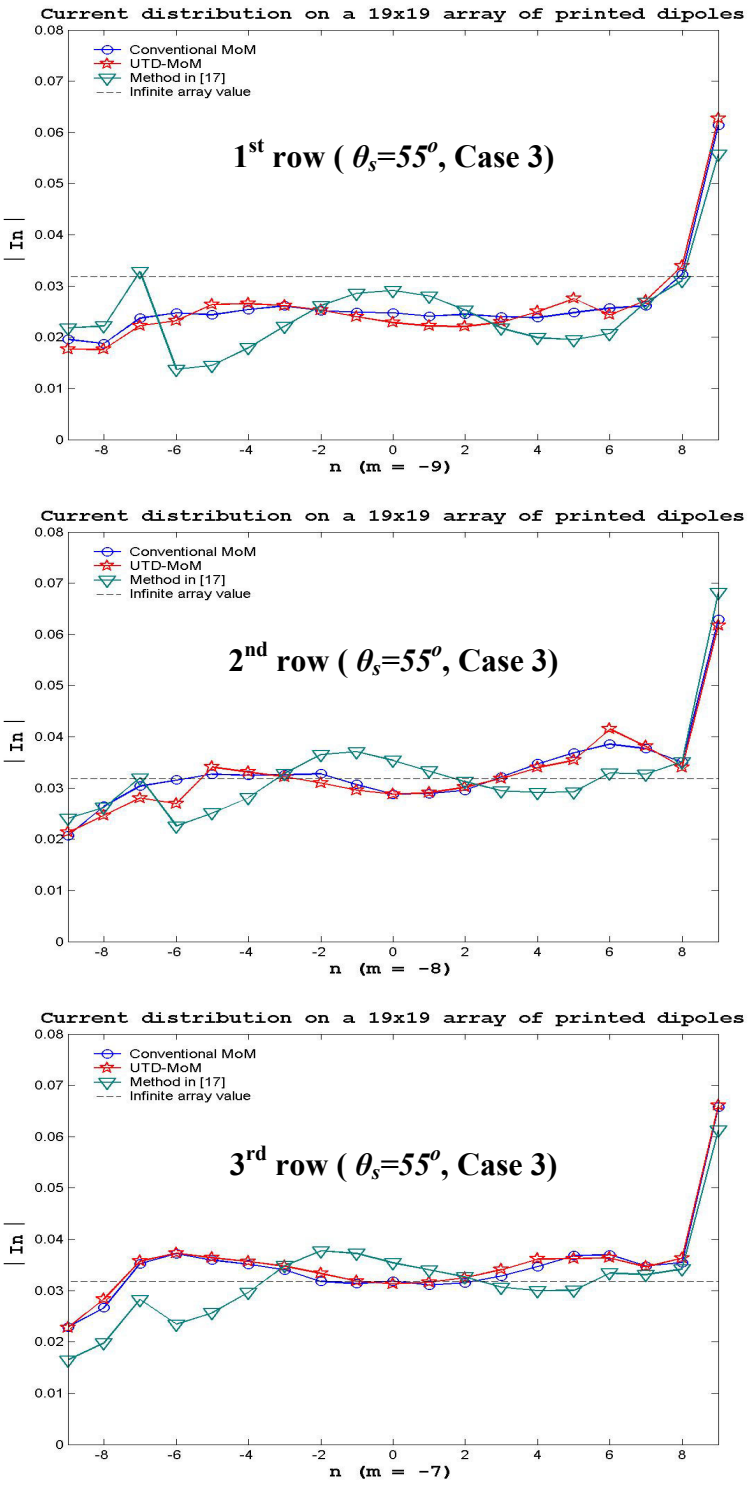

Figure 3.30 Element currents on the first three rows for Case 3 at $\theta_s = 55^o$; graph on the top is for the first row, graph in the middle is for the second row, graph at the bottom is for the third row.

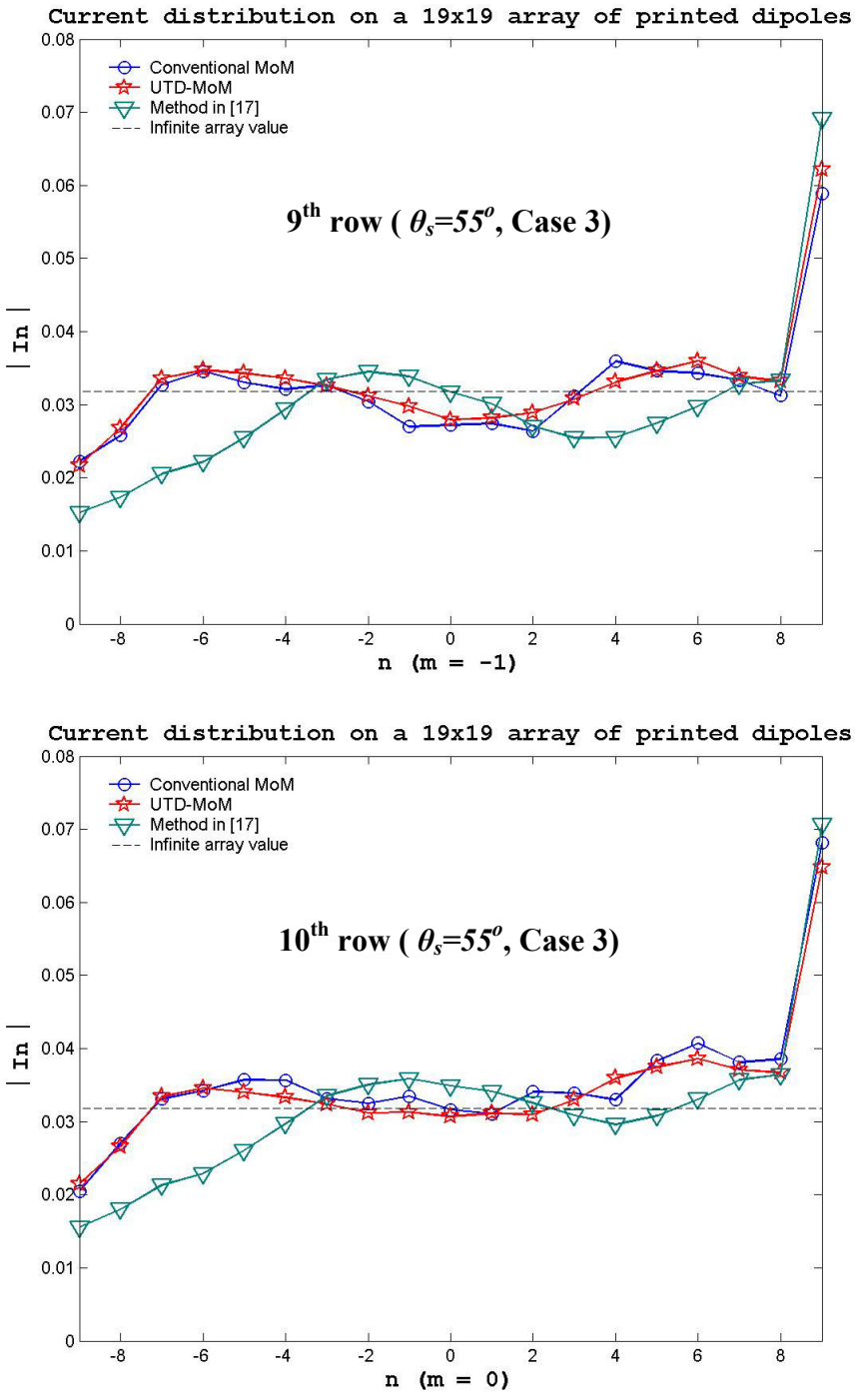

Figure 3.31 Element currents on the 9th and 10th rows in the middle for Case 3 at $\theta_s = 55^o$; graph on the top is for the 9th row, graph at the bottom is for the 10th row.

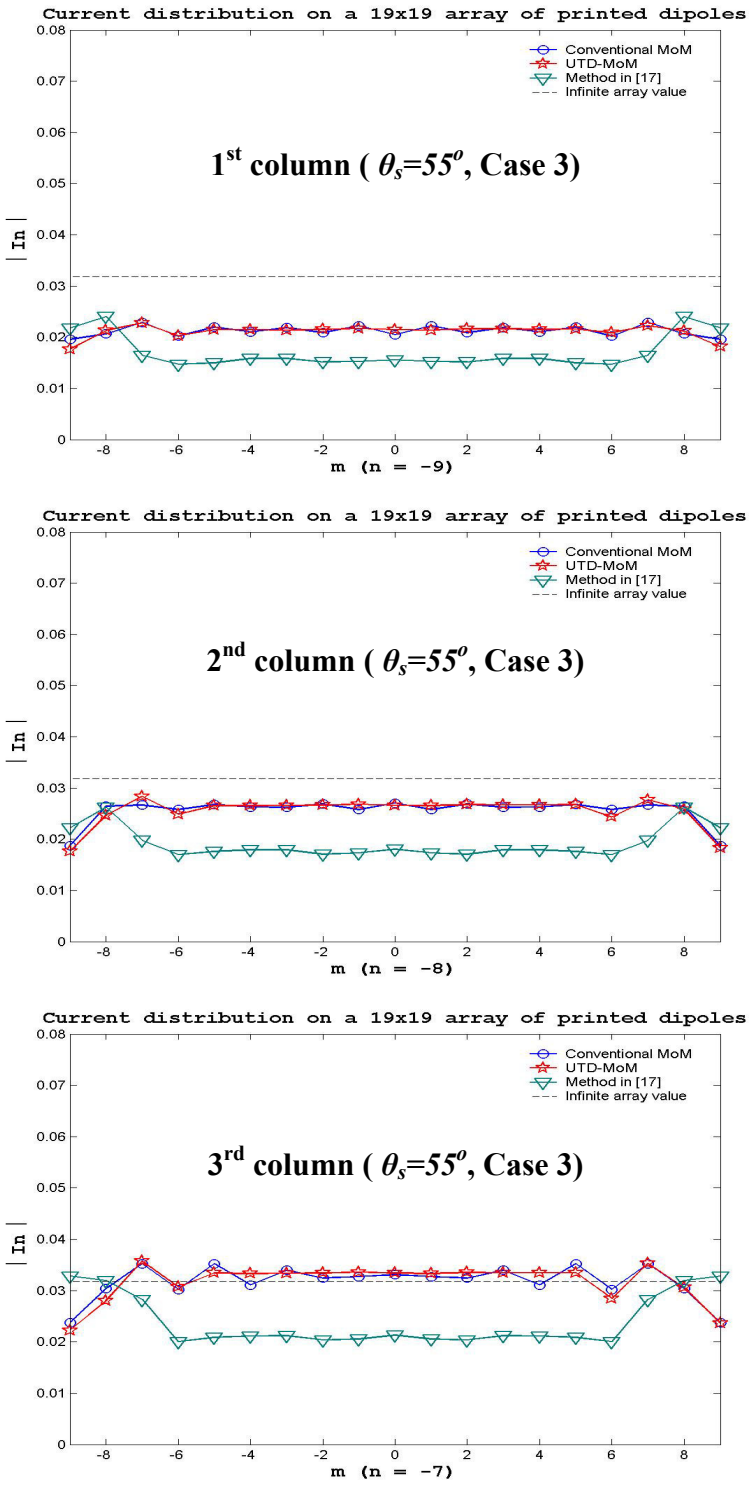

Figure 3.32 Element currents on the first three columns for Case 3 at $\theta_s = 55^o$; graph on the top is for the first column, graph in the middle is for the second column, graph at the bottom is for the third column

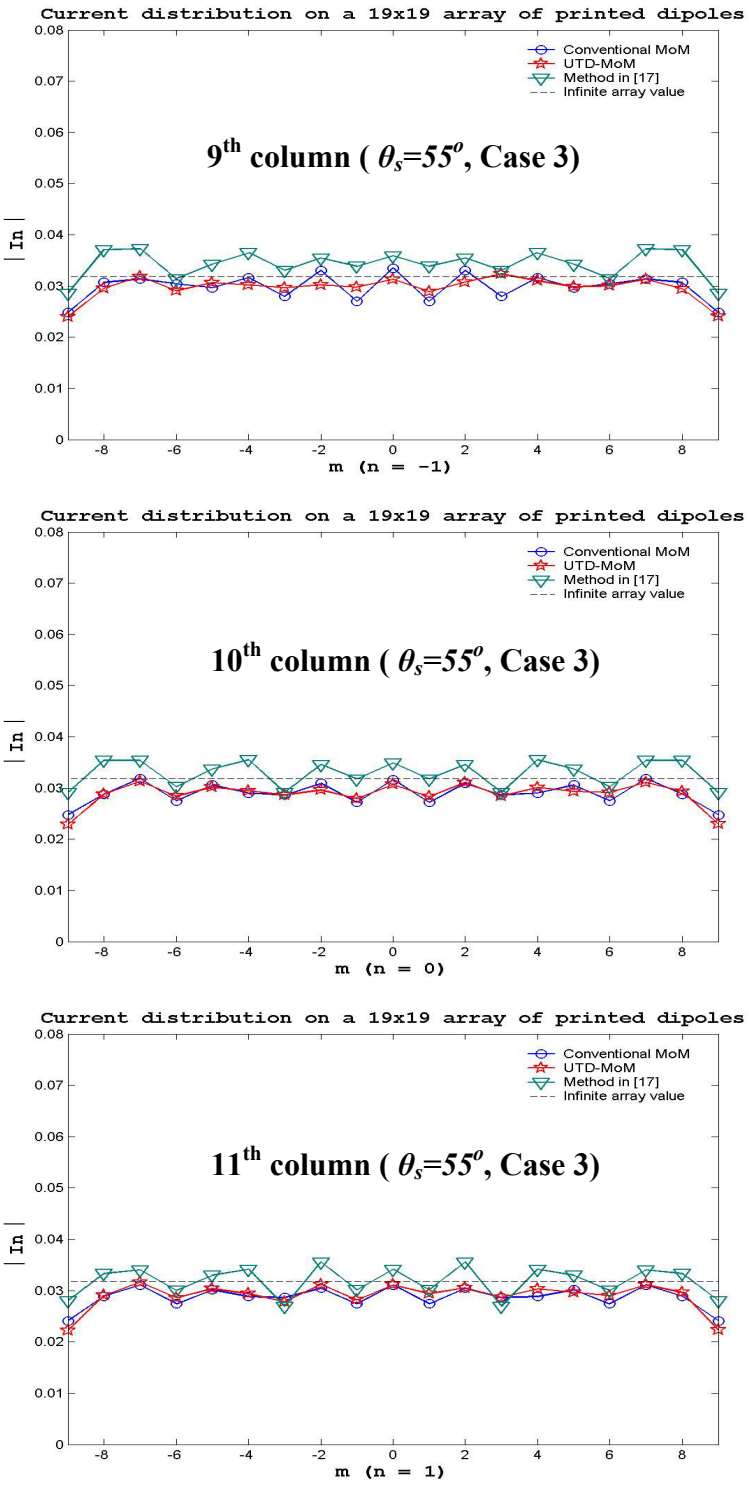

Figure 3.33 Element currents on the middle three columns for Case 3 at $\theta_s = 55^o$; graph on the top is for the 9th column, graph in the middle is for the 10th column, graph at the bottom is for the 11th column.

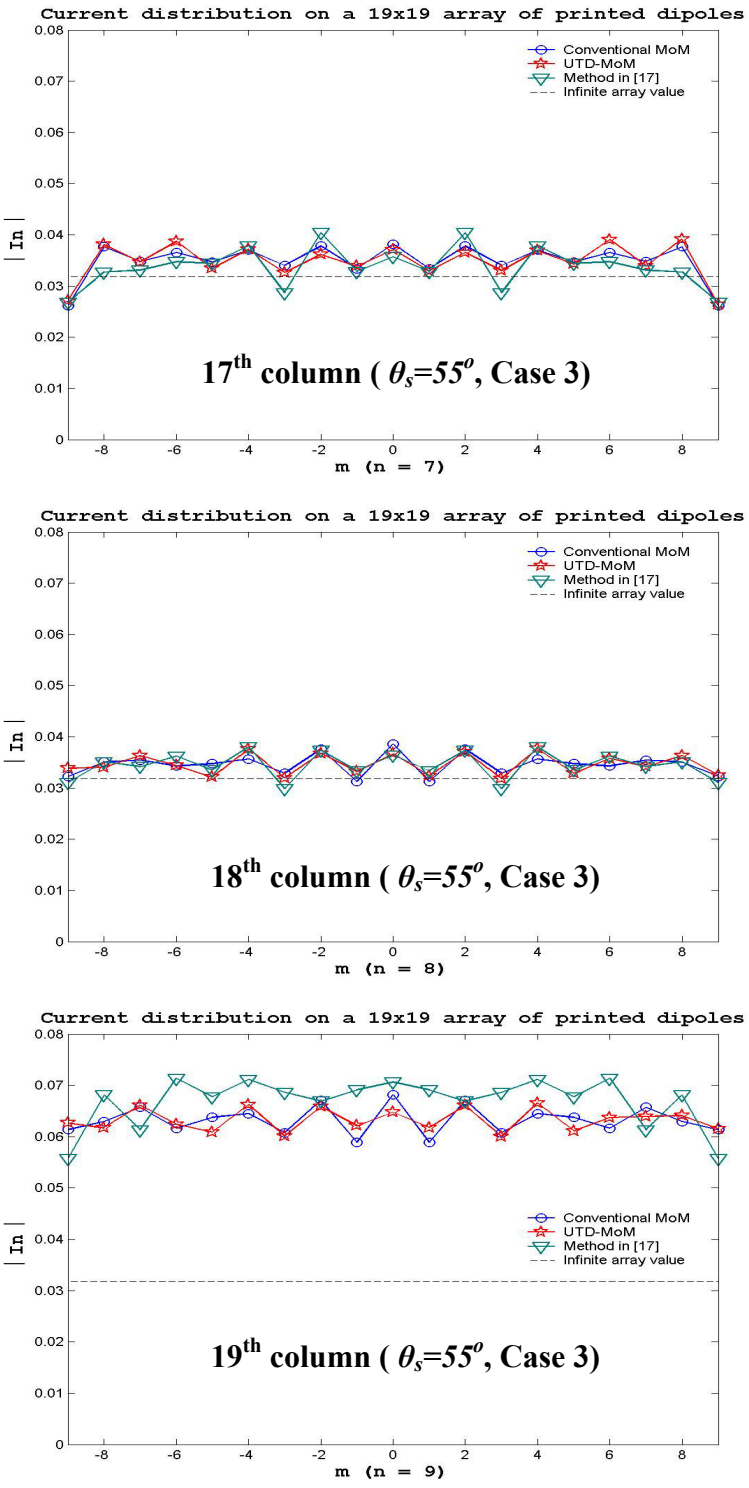

Figure 3.34 Element currents on the last three columns for Case 3 at $\theta_s = 55^o$; graph on the top is for the 17th column, graph in the middle is for the 18th column, graph at the bottom is for the 19th column.

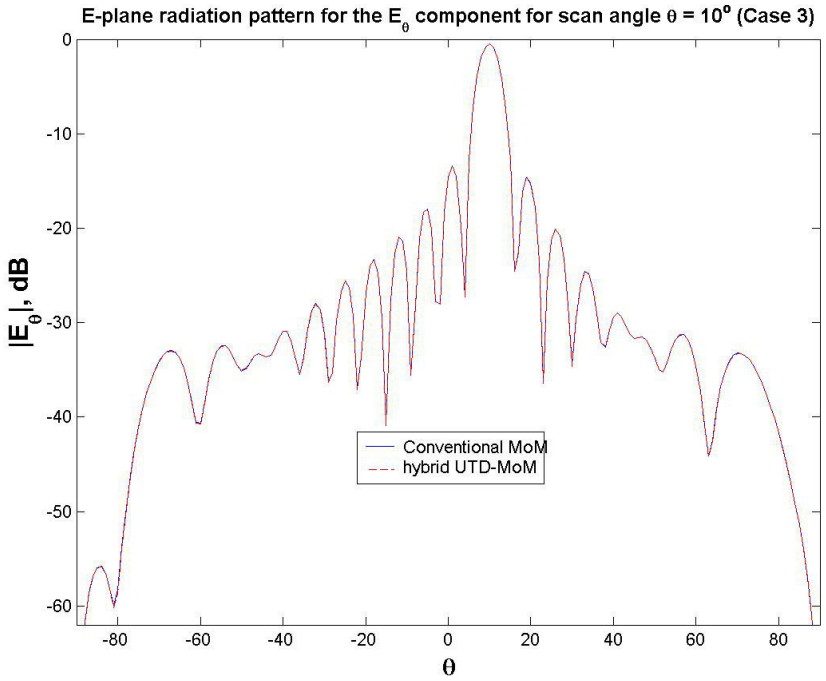

(a)

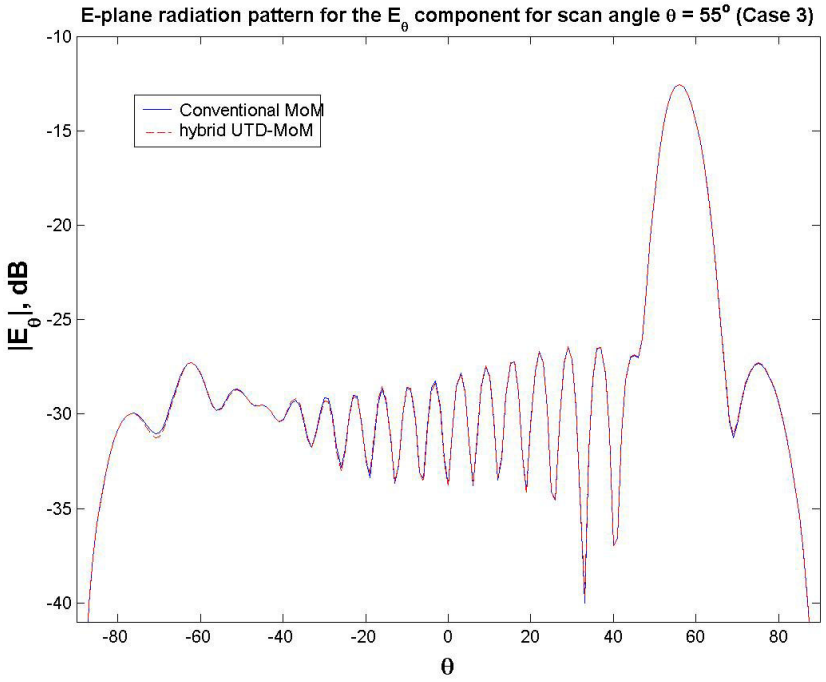

(b)

Figure 3.35 E-plane radiation patterns for the E_θ component in the case of scan angles a) $\theta_s = 10^o$ b) $\theta_s = 55^o$ (Case 3)

CHAPTER 4

CONCLUSION

In this study, a hybrid method is presented for the efficient yet accurate prediction of current distribution on a finite phased array of printed dipoles. Hybrid analysis begins with the usual MoM approach to obtain an integral equation formulation for the unknown currents on the dipoles. As the size of the array increases, this rigorous MoM analysis eventually becomes computationally prohibitive due to large number of unknowns. This drawback of conventional MoM approach for the analysis of large arrays is treated by utilizing the UTD-ray concept for the unknown array element currents. Asymptotic ray analysis for radiation/scattering from large finite arrays enables to expand the unknown array element currents using a few appropriate UTD-type global basis functions. Consequently, the number of unknown currents is drastically reduced, the matrices that make up the integral equation obtained via conventional MoM approach shrink greatly in size and the solution becomes computationally far more efficient as compared to the conventional MoM solution.

Of course the computational efficiency is not the only issue; the analysis should give reasonably accurate results as well. The analysis of large printed periodic arrays using the theory of infinite periodic structures allows the expansion of the fields in terms of Floquet waves and the analysis reduces to a single cell of periodicity. This provides a great efficiency on the computational cost but lacks in the accuracy. This infinite array approximation leads to reasonable results for describing the characteristics of elements far from the array boundaries, whereas it is significantly inaccurate for the elements in the vicinity of array boundaries.

However behavior of each element in the array can be predicted accurately by using the present UTD-MoM approach.

The numerical results and comparisons presented in Chapter 3 show that the hybrid UTD-MoM method developed in this study can be used for the efficient analysis of large planar printed dipole arrays. It is shown that this UTD-MoM approach provides very accurate results at scan angles from broadside to off-broadside (up to ~75^{o}) including scan blindness angles. It provides good results for the arrays on thin and thick dielectric substrates as well as dielectrics with high permittivity values. Finite array of printed dipoles is chosen in this study to provide simplicity in the understanding of the present hybrid method and ease of finding results of different approaches to compare them with the results of the present hybrid method. However the approach developed here can be extended for treating the complicated printed elements such as patches or more complex elements on multi-layered media and for the analysis of frequency selective surfaces (FSS).

In this study, the unknown currents are handled utilizing the UTD-ray concept providing computational efficiency. However this UTD-ray concept can also be used to calculate the mutual impedances to reduce the fill time of the impedance matrix. When separations between elements are greater than λ_0, the contribution of large group of elements to the field of an element can be calculated by using UTD rays of rectangular finite array. For small separations, mutual coupling calculations can be handled in conventional fashion.

In the future studies, the UTD-MoM approach developed in this study can also be extended for the analysis of arrays of slots, patches or more complex antenna array elements in multilayered structures. Furthermore, this approach can be modified to analyze radiation/scattering from conformal arrays, like arrays on cylindrical surfaces.

CHAPTER 5

REFERENCES

[1] Harrington, R.F., "Field Computation by Moment Methods," *IEEE Press, Piscataway, N.J.*, 1993.

[2] Keller, J.B., "Geometrical theory of diffraction," *J. Opt. Soc. Am.,* 52*,* 116-130, 1962.

[3] Kouyoumjian, R.G., and P.H. Pathak, "A uniform geometrical theory of diffraction for an edge in a perfectly conducting surface," *Proc. IEEE,* 62, 1448-1461, 1974.

[4] Pathak, P.H., "High frequency techniques for antenna analysis," *Proc. IEEE,* 80, 44-65, 1992.

[5] Burnside,W.D., C.L. Yu, and R.J. Marhefka, "A technique to combine the geometrical theory of diffraction and the moment method," *IEEE Trans. Antennas Propag.*, 23, 551-558, 1975.

[6] Thiele, G.A., and T.H. Newhouse, "A hybrid technique for combining moment methods with geometrical theory of diffraction," *IEEE Trans. Antennas Propag.*, 23*,* 62-69, 1975.

[7] Srikanth, S., P.H. Pathak, and C.W. Chuang, "Hybrid UTD-MM analysis of the scattering by a perfectly-conducting semi-circular cylinder," *IEEE Trans. Antennas Propag.*, 34, 1250-1257, 1986.

[8] R.C. Hansen, "Phased Array Antennas," *John Wiley and Sons*, New York, 1998

[9] Shubert, K.A., and B.A. Munk, "Matching properties of arbitrarily large dielectric covered phased arrays," *IEEE Trans. Antennas Propag.*, 31, 54-59, 1983.

[10] Ishimaru, A., R.J. Coe, G.E. Miller and W.P. Geren, "Finite periodic approach to large scanning array problems," *IEEE Trans. Antennas Propag.*, 33, 1213-1220, 1985.

[11] Skrivervik, A.K., and J.R Mosig, "Analysis of finite phased arrays of microstrip patches," *IEEE Trans. Antennas Propag.*, 41, 1105-1113, 1993.

[12] Carin, L., and L.B. Felsen, "Time harmonic and transient scattering by finite periodic flat strip arrays: Hybrid (Ray)-(Floquet mode)-MoM algorithm and its interpretation," *IEEE Trans. Antennas Propag.*, 41, 412-421, 1993.

[13] Carin, L., and L.B. Felsen, and T. Hsu, "High frequency fields excited by truncated arrays of non-uniformly distributed filamentary scatterers on an infinite dielectric grounded slab: Parameterizing leaky mode Floquet mode interaction," *IEEE Trans. Antennas Propag.*, 44, 1-11, 1996.

[14] Capolino, F., M. Albani, S. Maci, and L.B. Felsen, "Floquet wave diffraction theory for truncated dipole arrays: Propagating and evanescent spectra," *paper presented at URSI Commission B 1998 Electromagnetic Theory Symposium*, Thessaloniki, Greece, May 1998.

[15] Çivi, Ö.A., P.H. Pathak, and H.-T. Chou, "A hybrid UTD-MoM for efficient analysis of EM radiation/scattering from large finite planar arrays," *paper presented at URSI Commission B 1998 Electromagnetic Theory Symposium,* Thessaloniki, Greece, May 1998a.

[16] Çivi, Ö.A., P. H. Pathak, H.-T. Chou, P. Nepa, "A hybrid uniform geometrical diffraction-moment method for efficient analysis of electromagnetic radiation/scattering from large finite planar arrays," *Radio Science,* vol. 35, no. 2, pp. 607-620, Mar.-Apr. 2000.

[17] Çivi, Ö.A., V. B. Ertürk, P.H. Pathak, P. Janpugdee, and H.-T. Chou, "A Hybrid UTD-MoM Approach for the Efficient Analysis of Radiation/Scattering from Large, Printed Finite Phased Arrays," *2001 IEEE AP-S Intl. Symp.*, vol. 2, pp. 806-809, July 2001.

[18] Panuwat Janpugdee, "An Efficient Discrete Fourier Transform Based Ray Analysis of Large Finite Planar Phased Arrays," Thesis Report, The Ohio State University, 2002.

[19] A. Polemi, A. Toccafondi, S. Maci "High-frequency Green's function for a semi-infinite array of electric dipoles on a grounded slab. Part I: Formulation," *IEEE Trans. Antennas Propagat.*, Vol. 49, pp.1667-1677, Dec. 2001.

[20] Pozar, D.M., "Analysis of Finite Phased Arrays of Printed Dipoles," *IEEE Trans. Antennas Propag.*,33, 1045-1053, 1985.

[21] Pozar, D.M., "Input Impedance and Mutual Coupling of Rectangular Microstrip Antennas," *IEEE Trans. Antennas Propag.*, 30, 1191-1196, 1982.

[22] Pozar, D.M., "Improved computational efficiency for the moment method solution of printed dipoles and patches," *Electromagn.*, 3, 299-309, 1984.

[23] F. Capolino, M. Albani, S. Maci, L. B. Felsen, "Frequency domain Green's function for a planar periodic semi-infinite phased array. Part I: truncated Floquet wave formulation. Part II: diffracted wave phenomenology," *IEEE Trans. Antennas Propagat.*, Vol. 47, no. 1, pp. 67-74, Jan. 2000.

[24] F. Capolino, S. Maci and L. B. Felsen, "Green's function for a planar phased sectoral array of dipoles," *Radio Science*, Vol. 35, no.2, pp. 579-593, Mar.-Apr. 2000.

[25] Ö. Aydın Çivi, P.H. Pathak, H-T. Chou, P. Nepa, "Extension to a hybrid UTD-MoM approach for the efficient analysis of Radiation/Scattering from tapered array distributions," *2000 IEEE International Antennas and Propagation Symposium and URSI Radio Science Meeting*, Salt Lake City-USA, p.70-73, July 16-21 2000.

[26] Pozar, David M., "Considerations for Millimeter Wave Printed Antennas," *IEEE Trans. Antennas Propagat.*, Vol. AP-31, no. 5, pp.740-747, Sept. 1983.

[27] Pozar, David M., "Scan Blindness in Infinite Phased Array of Printed Dipoles," *IEEE Trans. Antennas Propagat.*, Vol. AP-32, no. 6, pp.602-610, June 1984.

[28] A. Ishimaru, "Electromagnetic Wave Propagation, Radiation and Scattering," pp. 178-180, Prentice Hall, New Jersey, 1991

APPENDIX A

PERIODIC STRUCTURES AND FLOQUET' S THEOREM

In this part, characteristics and mathematical representation of waves propagating in periodic structures are presented. Let us consider a wave propagating in periodic structures, which may be characterized by periodic boundary conditions or a periodically varied dielectric constant (Figure A.1) [28]. It is noted that the fields at a point z in an infinite periodic structure differ from the fields one period L away by a complex constant. This is apparently valid because in an infinite periodic structure, there should be no difference between the fields at z and $z+L$ except for the attenuation and phase shift. Let a function $u(z)$ represent a wave. Then a wave $u(z)$ at z and a wave $u(z+L)$ at $z+L$ are related in the same manner as a wave $u(z+L)$ at $z+L$ and a wave u($z+2L$) at $z+2L$. This can be expressed mathematically as:

$$\frac{u(z+L)}{u(z)} = \frac{u(z+2L)}{u(z+L)} = \frac{u(z+mL)}{u[z+(m-1)L]} = C = constant \tag{A.1}$$

From (A.1) the equation below is obtained:

$$u(z+mL) = C^m u(z) \tag{A.2}$$

The constant C is in general complex, which can be written as:

$$C = e^{-j\beta L}, \qquad \beta = complex \tag{A.3}$$

and β represents the propagation constant.

Now let us consider a function as:

$$R(z) = e^{j\beta z} u(z) \tag{A.4}$$

Then $R(z + L) = e^{j\beta(z+L)} u(z + L) = R(z)$. Therefore, $R(z)$ is a periodic function of z with the period L, and thus can be represented in a Fourier series:

$$R(z) = \sum_{n=-\infty}^{\infty} A_n e^{-j(2n\pi / L)z} \tag{A.5}$$

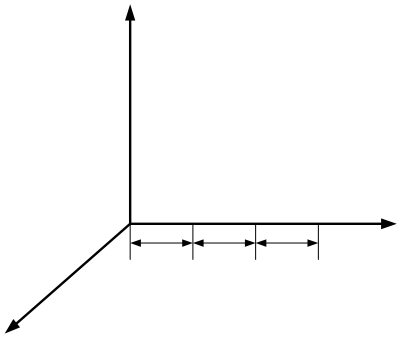

Figure A.1 Periodic structures

Using (A.4), a general expression for a wave in a periodic structure with the period L can be obtained:

$$\begin{aligned} u(z) &= \sum_{n=-\infty}^{\infty} A_n e^{-j(\beta+2n\pi / L)z} \\ &= \sum_{n=-\infty}^{\infty} A_n e^{-j\beta_n z} \end{aligned} \tag{A.6}$$

where $\beta_n = \beta + \dfrac{2n\pi}{L}$

Noting that, in general, the wave consists of both positive and negative-going waves:

$$u(z) = \sum_{n=-\infty}^{\infty} A_n e^{-j\beta_n z} + \sum_{n=-\infty}^{\infty} A_n e^{+j\beta_n z} \tag{A.7}$$

This is a representation of a wave in periodic structures in a form of an infinite series, resembling harmonic representation ($e^{-j\omega_n t}$) in time. The *n*th term in (A.6) is called the *n*th *space harmonic* or *Hartree harmonic*. Equation (A.7) is the mathematical representation of Floquet's theorem, which states that the wave in periodic structures consists of an infinite number of *space harmonics*.